SANDIA REPORT

SAND2009-4185
Unlimited Release
Printed August 2009

Aerodynamic and Aeroacoustic Tests of a Flatback Version of the DU97-W-300 Airfoil

Matthew F. Barone, Sandia National Laboratories
Dale E. Berg, Sandia National Laboratories
William J. Devenport, Virgina Polytechnic Institute and State University
Ricardo Burdisso, Virgina Polytechnic Institute and State University

Prepared by
Sandia National Laboratories
Albuquerque, New Mexico 87185 and Livermore, California 94550

Sandia is a multiprogram laboratory operated by Sandia Corporation,
a Lockheed Martin Company, for the United States Department of Energy's
National Nuclear Security Administration under Contract DE-AC04-94-AL85000.

Issued by Sandia National Laboratories, operated for the United States Department of Energy by Sandia Corporation.

Available to DOE and DOE contractors from
U.S. Department of Energy
Office of Scientific and Technical Information
P.O. Box 62
Oak Ridge, TN 37831

Telephone: (865) 576-8401
Facsimile: (865) 576-5728
E-Mail: reports@adonis.osti.gov
Online ordering: http://www.osti.gov/bridge

Available to the public from
U.S. Department of Commerce
National Technical Information Service
5285 Port Royal Rd
Springfield, VA 22161

Telephone: (800) 553-6847
Facsimile: (703) 605-6900
E-Mail: orders@ntis.fedworld.gov
Online ordering: http://www.ntis.gov/help/ordermethods.asp?loc=7-4-0#online

SAND2009-4185
Unlimited Release
Printed August 2009

Aerodynamic and Aeroacoustic Tests of a Flatback Version of the DU97-W-300 Airfoil

Matthew F. Barone and Dale E. Berg
Wind Energy Technology Department
Sandia National Laboratories
P.O. Box 5800
Albuquerque, NM 87185-1124
mbarone@sandia.gov

William J. Devenport
Department of Aerospace and Ocean Engineering
Virginia Polytechnic Institute and State University
215 Randolph Hall
Blacksburg, VA 24061

Ricardo Burdisso
Department of Mechanical Engineering
100 Randolph Hall
Blacksburg, VA 24061

Abstract

Results from an experimental study of the aerodynamic and aeroacoustic properties of a flatback version of the TU Delft DU97-W-300 airfoil are presented. Measurements were made for both the original DU97-W-300 and the flatback version. The chord Reynolds number varied from 1.6×10^6 to 3.2×10^6. The data were gathered in the Virginia Tech Stability Wind Tunnel, which includes a special aeroacoustic test section to enable measurements of airfoil self-noise. Corrected wind tunnel aerodynamic measurements for the DU97-W-300 are compared to previous solid wall wind tunnel data and are shown to give good agreement. Force coefficient and surface pressure distributions are compared for the flatback and the original

airfoil for both free-transition and tripped boundary layer configurations. Aeroacoustic data are presented for the flatback airfoil, with a focus on the amplitude and frequency of noise associated with the vortex-shedding tone from the blunt trailing edge wake. The effect of a splitter plate trailing edge attachment on both drag and noise of the flatback airfoil is also investigated.

Acknowledgment

The authors gratefully acknowledge the contributions of the following graduate students, who set up and carried out the measurements described in this report: Aurelien Borgoltz, Hugo Camargo, Erin Crede, Leonardo Errasquin, Marcel Remillieux, Matthew Rasnick, and Philip van Seeters.

Contents

1 Introduction **11**

2 Apparatus and Instrumentation **13**
2.1 Stability Wind Tunnel 13
2.2 Anechoic System 13
2.3 Airfoil Models 25
2.4 Aerodynamic Instrumentation 27
2.5 Acoustic Instrumentation 31

3 Correction of Aerodynamic Data **38**

4 Aerodynamic Results **39**
4.1 Surface Pressure Measurements, $28 \leq U_\infty \leq 30$m/s 40
4.2 Surface Pressure Measurements, $42 \leq U_\infty \leq 60$m/s 44
4.3 Wake Measurements 46
4.4 Trailing Edge Boundary Layer Properties 54

5 Acoustic Results **56**
5.1 Empty Tunnel Results 58
5.2 Airfoil Results 58

6 Conclusions **84**

Appendices **84**

Appendix

A Development of Porous Wall Wind Tunnel Corrections **85**

B Definition of $1/12^{\text{th}}$ Octave Bands **117**

References **117**

Figures

1 Photograph and plan view schematic of the Virginia Tech Stability Tunnel in anechoic configuration. Photo shows connection to Randolph Hall through metal building at center of picture. This pressure sealed steel room contains both the test section and operating console. 14
2 Plan view cross-section of the anechoic system as installed, showing the test section flanked by the two anechoic chambers. Dimensions in meters. Blue shaded areas of the test section side walls are acoustically treated. 16

3 Cross section through the anechoic chambers and test section looking downstream. Dimensions in meters. 17
4 Interior of the anechoic test section as seen from downstream. An airfoil model installed with end plates and the partially installed trailing edge hot-wire traverse are visible. 18
5 Exterior view of the anechoic test section with the acoustic windows and the port side anechoic chamber removed. The starboard side anechoic chamber is visible in the background. 19
6 Photo of the central portion of acoustic test section with the starboard-side anechoic chamber and Kevlar acoustic window removed. An airfoil model installed with end plates and the trailing edge hot-wire traverse are visible. 20
7 Photo taken from beneath the test section, showing the collar and bearing arrangement that form the airfoil mount. 21
8 Out-of-flow noise levels in the starboard-side anechoic chamber 1.9m from the center of the acoustic window (2.7m from the test section center), as a function of flow speed in the empty test section. (a) 1 Hz bandwidth SPL. (b) 1 Hz bandwidth A-weighted SPL. 23
9 Attenuation of sound passing through the (a) acoustic Kevlar windows and (b) shear layer as a function of frequency in 1/3 octave bands. 24
10 Estimated correction required to account for reflection of an acoustic wave emanating from a point source within the test section, reflecting off the anechoic chamber back wall, then traveling to the microphone array location. 25
11 DU97-W-300 and DU97-flatback airfoil shapes. 26
12 Splitter plate attachment used with the DU97-flatback. Dimensions in mm. 27
13 Photograph showing the traverse gear mounted in the anechoic test section (looking upstream). 29
14 Dwyer 160 pitot static probe in straight configuration. Dimensions in mm. 30
15 Pitot static probe rake detail (dimensions in mm). 30
16 Photographs of the hot-wire traverse. 32
17 View from inside the port-side anechoic chamber showing microphone phased array. 33
18 Microphone phased-array pattern. 34
19 Array point spread function for 1/12th octave bands with center frequencies at (a) 542.4, (b) 1024.0, (c) 2048.0, (d) 4096.0 Hz at a distance of 3.0 meters. Flow in the tunnel section is not accounted for in these results. 35
20 Array (a) resolution or beamwidth and (b) signal-to-noise ratio in 1/12th octave bands for the 500-5000Hz frequency range at a distance of 3.0 meters. Flow in the tunnel section not accounted for in these results. 36
21 Position of the array on the starboard side used in all runs. 37
22 Coordinate systems and measurement locations for the tests. Z coordinate is measured from center-span out of the paper. 39
23 Comparison of corrected surface pressure distributions between TU-Delft wind tunnel data and measurements taken in the Virginia Tech acoustic test section. 41
24 Comparison of corrected surface pressure distributions between TU-Delft wind tunnel data and measurements taken in the Virginia Tech acoustic test section. 42

25 Corrected surface pressure coefficient distributions. (a) DU97-W-300 and DU97-flatback, $Re_c = 1.6 - 1.8 \times 10^6$, no trip. (b) DU97-flatback, $\alpha_{eff} = 11.9$ deg., $Re_c = 1.6 \times 10^6$. 43
26 Corrected surface pressure coefficient distributions, for DU97-flatback without and with splitter plate, $Re_c = 1.6 \times 10^6$, serrated tape trip . (a) $\alpha_{eff} = 4.4$ deg. (b) $\alpha_{eff} = 11.6$. 43
27 Corrected lift coefficient for DU97-W-300 and DU97-flatback airfoils with $28 \leq U_\infty \leq 30$m/s, compared with data for the DU97-W-300 taken in the TU-Delft wind tunnel. 44
28 Corrected pitching moment coefficient for DU97-W-300 and DU97-flatback airfoils with $28 \leq U_\infty \leq 30$m/s, compared with data for the DU97-W-300 taken in the TU-Delft wind tunnel. 45
29 Uncorrected surface pressure coefficient distributions, comparing the DU97-W-300 with the DU97-flatback at the same or similar geometric angle of attack, $Re_c = 3.1 - 3.2 \times 10^6$, no trip. 46
30 Uncorrected lift coefficients for the DU97-W-300 and DU97-flatback for $55 \leq U_\infty \leq 60$m/s. 48
31 DU97-flatback stagnation and static pressure profiles measured at $X/c = 3.74$. $Re_c = 3.2 \times 10^6$, $\alpha_{geom} = 5.1$ deg, no trip. 49
32 DU97-flatback stagnation and static pressure profiles measured at $X/c = 3.74$. $Re_c = 3.2 \times 10^6$, $\alpha_{geom} = 12.8$ deg, no trip. 50
33 Control volume used for drag analysis based on wake profiles. 51
34 Drag coefficients for the DU97-W-300 and DU97-flatback, compared with data taken in the TU-Delft wind tunnel. 52
35 Uncorrected drag coefficients for the DU97-flatback with and without splitter plate, $Re_c = 3.2 \times 10^6$, no trip. 53
36 (a) Beamforming measurement plane for the computation of the acoustic maps. (b) Typical acoustic map and color scale for an airfoil measurement. (Example shown: DU97-flatback, 5.1 degrees α_{geom}, 28m/s flow speed, and 1933 Hz 1/12th band). . 59
37 Beamforming measurement volume for the computation of the integrated spectrum. 60
38 Average noise spectrum for the empty tunnel operating at several flow speeds. (Frequency resolution: 3.125 Hz) 61
39 Average noise spectrum the empty tunnel operating at several flow speeds scaled to the (a) 6th and (b) 5th power of the flow velocity. (Frequency resolution: 3.125 Hz) 62
40 Average noise spectrum for the empty tunnel and the DU97-flatback airfoil ($\alpha_{geom} =$ 15.4 degrees) at 56.5m/s. 63
41 Average narrowband noise spectrum for the DU97-W-300 airfoil at ~ 57 m/s (runs 10, 7, 11, 4, and 114). 63
42 Average narrowband noise spectrum for the DU97-W-300 airfoil at ~ 44 m/s (runs 9, 6, 3, and 113). 64
43 Average narrowband noise spectrum for the DU97-W-300 airfoil at ~ 28 m/s (runs 8, 5, 12, 2, and 112). 64

44 Average narrowband noise spectrum for the DU97-flatback airfoil at $\sim$ 57 m/s (runs 20, 23, 38, 36, and 114). 65
45 Average narrowband noise spectrum for the DU97-flatback airfoil at $\sim$ 44 m/s (runs 19, 22, 35, and 113). 65
46 Average narrowband noise spectrum for the DU97-flatback airfoil at $\sim$ 28 m/s (runs 18, 34, 37, and 112). 66
47 Average narrowband noise spectrum for the DU97-flatback and DU97-flatback with splitter plate at $\sim$ 58 m/s (runs 29 vs 20, 26 vs 23, and 33 vs 36). 67
48 Average narrowband noise spectrum for the DU97-flatback and DU97-flatback with splitter plate at $\sim$ 44 m/s (runs 28 vs 19, 25 vs 22, and 32 vs 35). 68
49 Average narrowband noise spectrum for the DU97-flatback and DU97-flatback with splitter plate at $\sim$ 28 m/s (runs 27 vs 18 and 31 vs 34). 68
50 Acoustic maps (1/12th octave bands) for the DU97-flatback airfoil at 5.1 degrees geometric AoA at 57.5 m/s flow speed (run 20). 69
51 Acoustic maps (1/12th octave bands) for the DU97-flatback airfoil at 5.1 degrees geometric AoA at 57.5 m/s flow speed (run 20) 70
52 Acoustic maps (1/12th octave bands) for the DU97-flatback airfoil at 5.1 degrees geometric AoA at 57.5 m/s flow speed (run 20) 71
53 Acoustic maps (1/12th octave bands) for the DU97-flatback airfoil at 5.1 degrees geometric AoA at 57.5 m/s flow speed (run 20) 72
54 Description of typical noise spectrum of an airfoil model in 1/12th octave bands: (a) Average and integrated spectrum separately and (b) Average and adjusted integrated spectrum as a single trailing edge noise spectrum. Example: DU97-flatback without splitter plate at 5.1 degrees AoA at 56 m/s. 74
55 1/12th octave band noise spectrum for the DU97-W-300 airfoil at $\sim$ 56 m/s flow speed. 75
56 1/12th octave band noise spectrum for the DU97-W-300 airfoil at $\sim$ 42 m/s flow speed. 76
57 1/12th octave band noise spectrum for the DU97-W-300 airfoil at $\sim$ 28 m/s flow speed. 76
58 1/12th octave band noise spectrum for the DU97-flatback airfoil without splitter plate at $\sim$ 56 m/s flow speed. 77
59 1/12th octave band noise spectrum for the DU97-flatback airfoil with splitter plate at $\sim$ 56 m/s flow speed. 77
60 1/12th octave band noise spectrum for the DU97-flatback airfoil without splitter plate at $\sim$ 43 m/s flow speed. 78
61 1/12th octave band noise spectrum for the DU97-flatback airfoil with splitter plate at $\sim$ 43 m/s flow speed. 78
62 1/12th octave band noise spectrum for the DU97-flatback airfoil without splitter plate at $\sim$ 28 m/s flow speed. 79
63 1/12th octave band noise spectrum for the DU97-flatback airfoil with splitter plate at $\sim$ 28 m/s flow speed. 79
64 (a) Trailing edge noise spectrum for the DU97-flatback at 5.1 degrees geometric AoA for 57, 44, and 28 m/s and (b) scaled to the 6th power of the flow velocity. No trip. 81

65 Trailing edge noise spectrum for the DU97-flatback with and without splitter plate at 5.1 degrees geometric AoA and $\tilde{5}6$ m/s flow speed. No trip. 82
66 Trailing edge noise spectrum for the DU97-flatback at 5.1, 12.8, and 15.4 degrees geometric AoA and $\tilde{5}6$ m/s flow speed. No trip. 82
67 Trailing edge noise spectrum for the DU97-flatback at 12.8 degrees geometric AoA and $\tilde{5}6$ m/s flow speed, tripped and no trip. 83

1 Introduction

Design of the inboard region of wind turbine blades involves a compromise between aerodynamic performance, structural requirements and, at large scale, size constraints due primarily to over-land transportation of blades. The flatback airfoil concept was motivated by these multi-disciplinary considerations. The shape of a flatback airfoil is generated by taking an existing airfoil shape and adding thickness about the camber line over some aft portion of the airfoil, resulting in an airfoil with the same camber line as the original, but with a blunt base at the trailing edge. This approach is in contrast to "truncated" airfoils where the trailing edge is simply cut off, changing the camber and degrading airfoil lift performance. A primary structural advantage of the flatback shape is that its sectional strength is larger than that of a sharp trailing edge airfoil for a given chord length. This property can be leveraged to decrease blade weight and cost, both critical issues for the next generation of wind turbine blades [1]. Aerodynamic benefits include increased lift curve slope, increased maximum lift, and reduced sensitivity to stall caused by leading edge soiling [2].

Technical risks associated with the use of flatback airfoils for the inboard region of wind turbine blades include increased aerodynamic noise and increased aerodynamic drag. Both of these penalties are the result of the blunt trailing edge shape and the wake that is produced by this shape. The relatively low pressure at the blunt base results in a much larger drag force than for a conventional airfoil shape. The effect of this drag penalty on rotor thrust and torque coefficient for typical inboard twist angles is not severe, and in fact can be offset by the additional lift that a flatback airfoil generates [3]. Consideration of drag reducing devices such as splitter plates or trailing edge serrations may be desirable to further boost performance, however.

The increased noise from the flatback is due primarily to the vortex shedding phenomenon associated with bluff-body wakes. The vortex shedding often leads to tonal noise, similar to the Aeolian tones of flow past circular cylinders. The intensity of bluff-body vortex shedding tones at low Mach number scales with the sixth power of the relative flow velocity. Broadband aeroacoustic noise sources associated with turbulent boundary layer-trailing edge interaction scale with the fifth power of the relative flow velocity. Since outboard flow velocities are much higher than those encountered inboard, the overall aerodynamic noise levels of a rotor incorporating inboard flatback shapes will likely continue to be dominated by outboard turbulent boundary layer trailing edge noise. However, two aspects of the flatback noise source may be cause for concern. First, the vortex-shedding noise from flatbacks is likely to be contained in a relatively low-frequency band (50-200 Hz). Some community noise regulations consider both A-weighted sound, which emphasizes higher frequencies to which the human ear is more sensitive, as well as separate low-frequency noise standards. Second, the source of the flatback noise is likely to be tonal in nature. Pure tones are perceived as more annoying than broadband noise, often resulting in special treatment of tones in noise standards.

Previous work on analysis and testing of flatback airfoils includes wind tunnel testing at moderate Reynolds numbers [2], as well as computational modeling of flatback airfoils and their effect on rotor performance [3, 4]. The goals of the present study are to: 1) measure aerodynamic performance of flatback airfoils at Reynolds numbers representative of those encountered by utility scale wind turbines, including quantification of the drag penalty, 2) quantify the aeroacoustic noise

from a flatback airfoil, 3) assess the effect of a simple splitter plate attachment on flatback airfoil drag and noise, and 4) generate data that can be used to validate computational models of flatback aerodynamics and aeroacoustics. To this end, a wind tunnel experiment was performed to measure the aerodynamic and aeroacoustic characteristics of the TU-Delft DU97-W-300 airfoil [5] and a flatback version of that airfoil, the DU97-flatback. The DU97-W-300 was designed to serve as a base airfoil for the development of thick airfoils for use on wind turbines. The DU97-flatback was created by adding thickness to the aft half of the DU97-W-300 airfoil, giving a blunt trailing edge with a base width of 10% chord.

Models of the DU97-W-300 and DU97-flatback were tested in the Virginia Tech Stability Wind Tunnel. Measurements were made of airfoil surface pressure distributions, trailing edge boundary layer characteristics, wake pressure profiles (from which drag was calculated), and trailing edge noise. The wind tunnel facility, experimental setup, and instrumentation are described in Section 2. Wind tunnel wall interference corrections are discussed in Section 3. The results from the aerodynamic measurements are presented and discussed in Section 4, and the aeroacoustic data are presented in Section 5. Conclusions are made in Section 6.

2 Apparatus and Instrumentation

2.1 Stability Wind Tunnel

All tests were performed in the Virginia Tech Stability Wind Tunnel. This facility is a continuous, single return, subsonic wind tunnel with 7.3-m long removable rectangular test sections of square cross section 1.83m on edge. The general layout is illustrated in Figure 1. The tunnel is powered by a 0.45-MW variable speed DC motor driving a 4.3-m propeller at up to 600 r.p.m. This provides a maximum speed in the test section (with no blockage) of about 75m/s and a Reynolds number per meter up to about 5,000,000. The tunnel forms a closed loop, but has an air exchange tower open to the atmosphere to allow for temperature stabilization. The air exchange tower is located downstream of the fan and motor assemblies. Downstream of the tower the flow is directed into a 5.5×5.5m settling chamber containing seven turbulence-reducing screens, each with an open area ratio of 0.6 and separated by 0.15m. Flow exits this chamber through the 9:1 contraction nozzle which further reduces turbulence levels and accelerates the flow to test speed.

At the downstream end of the test section, flow passes into a 3-degree diffuser. Sixteen 0.16m high vortex generators arranged at intervals of 0.39m around the floor, walls and ceiling of the flow path at the entrance to the diffuser serve to mix momentum into the diffuser boundary layer, minimizing the possibility of separation and the consequent instability and inefficiency. The four corners in the flow path (two between the air exchange tower and settling chamber, and two between diffuser and fan) are equipped with diagonal arrays of shaped turning vanes. Spacing between the vanes is 0.3m, except in the corner immediately ahead of the settling chamber where the spacing is 0.076m.

The test section itself is located in a hermetically sealed steel building (Figure 1). The pressure inside this control room is equalized with the static pressure in the test section flow, this being below atmospheric by an amount roughly equal to the dynamic pressure. Pressure is equalized through a small aperture in the tunnel side wall at the upstream entrance to the diffuser. Flow through the empty test section (measured with a hard-wall test section in place) is both closely uniform and of very low turbulence intensity. Table 1 shows recent (2006) measurements of free stream turbulence levels as a function of flow speed. Turbulence levels are as low 0.016% at 12m/s and increase gradually with flow speed. Choi and Simpson [6] measured the lateral integral scales of the streamwise velocity in both the horizontal (L_z) and vertical (L_y) directions. They found L_z=56mm for 15m/s and 28mm for 37.5m/s, and L_y=122mm for 15m/s and 25mm for 37.5m/s.

2.2 Anechoic System

Physical Layout

The Stability Wind Tunnel is unique in that it has an anechoic system that can be installed or removed at will. The anechoic system permits acoustic as well as aerodynamic flow measurements

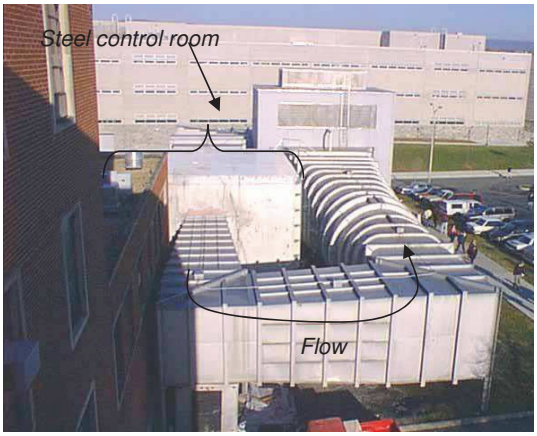

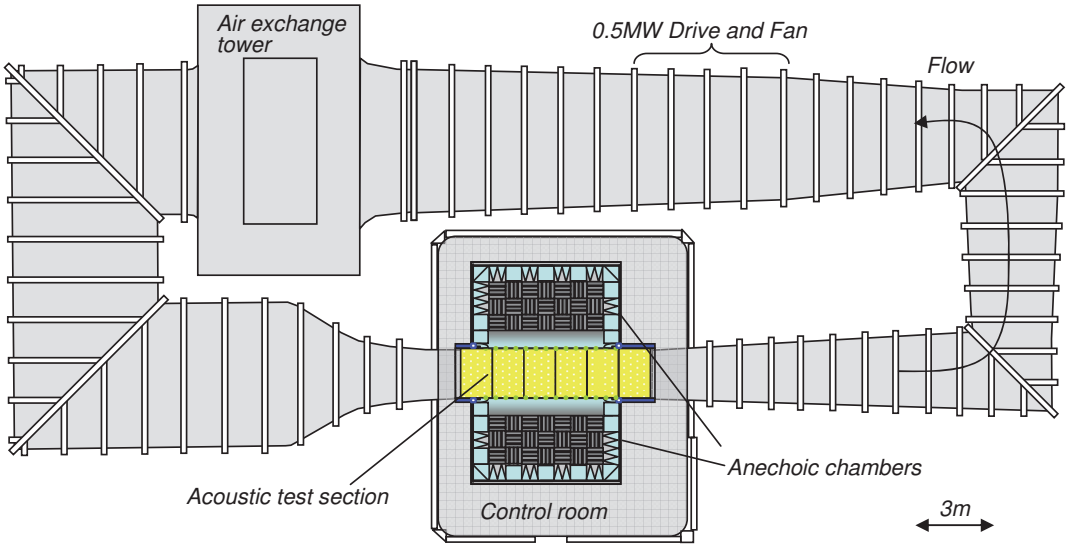

Figure 1. Photograph and plan view schematic of the Virginia Tech Stability Tunnel in anechoic configuration. Photo shows connection to Randolph Hall through metal building at center of picture. This pressure sealed steel room contains both the test section and operating console.

Freestream Velocity, m/s	RMS Streamwise Fluctuations, %
12	0.016
21	0.021
30	0.024
48	0.029
57	0.031

Table 1. Free stream turbulence levels in the empty hard wall test section of the Stability Tunnel as a function of flow speed, as measured May 2006. Turbulence levels are based on spectral integrations that exclude electrical noise at frequencies exceeding 100 Hz.

and was used for all tests reported here. The anechoic system consists of an acoustic test section flanked by two anechoic chambers (Figures 1, 2 and 3).

The acoustic test section is depicted in Figures 2 to 5. The test section consists of acoustically treated upper and lower walls that run the full 7.3m length of the test section and partial side walls, also treated, at the test section entrance and exit. Large rectangular openings in the side walls which extend 4.2m in the streamwise direction and cover the full 1.83-m height of the test section serve as acoustic windows (Figure 5). Sound generated in the test flow exits the test section through these windows into the anechoic chambers to either side. Large tensioned panels of Kevlar cloth cover these openings, permitting the sound to pass while containing the bulk of the flow. The test section arrangement thus simulates a half-open jet, acoustically speaking. The Kevlar windows eliminate the need for a jet catcher and, by containing the flow, substantially reduce the lift interference when airfoil models are placed in the test flow. This arrangement is unique to the Virginia Tech Stability Wind Tunnel and, like the anechoic system itself, is a relatively recent innovation.

The upper wall of the test section is formed from a series of perforated steel sheet panels bonded to a layer of Kevlar cloth that forms a smooth, quiet, but acoustically transparent flow surface. The volume behind this flow surface is filled with 0.457m-high foam wedges that eliminate any acoustic reflections at frequencies above 190Hz. The lower wall of the test section has the same construction except in the area immediately around the model mount where a 1.83x0.84m section of the acoustically treated flow surface is replaced by medium density fiberboard (MDF) panels (Figure 6). The MDF panels can be removed and replaced, providing an access pathway through which models can be installed. The partial side walls (Figure 2) include 150mm deep acoustic absorbers filled with a combination of melamine foam and fiberglass insulation and covered with a tensioned Kevlar flow surface.

The upper and lower walls contain hardware for the (vertical) mounting of two-dimensional airfoil models. This includes a simple collar, located just above the level of the upper wall, and a bearing arrangement (Figure 7) located just below the level of the lower wall. Both are designed to accept and hold an 88.9mm diameter vertical tube of circular cross section centered midway between the acoustic windows and 3.56m from the upstream end of the test section. To date, all

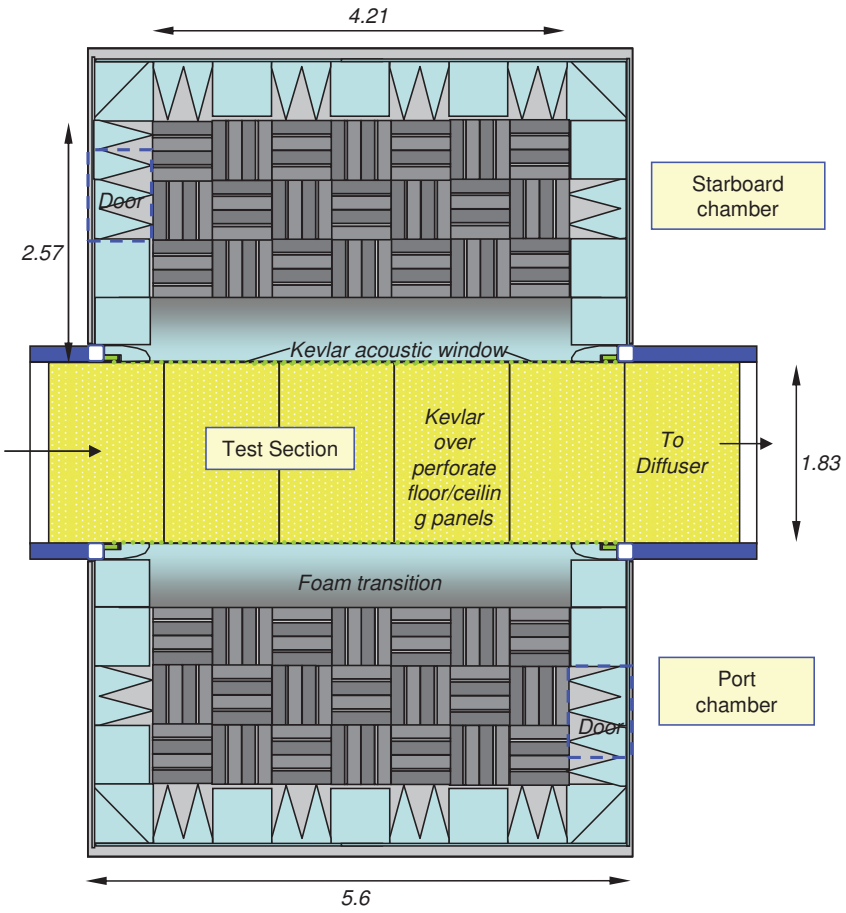

Figure 2. Plan view cross-section of the anechoic system as installed, showing the test section flanked by the two anechoic chambers. Dimensions in meters. Blue shaded areas of the test section side walls are acoustically treated.

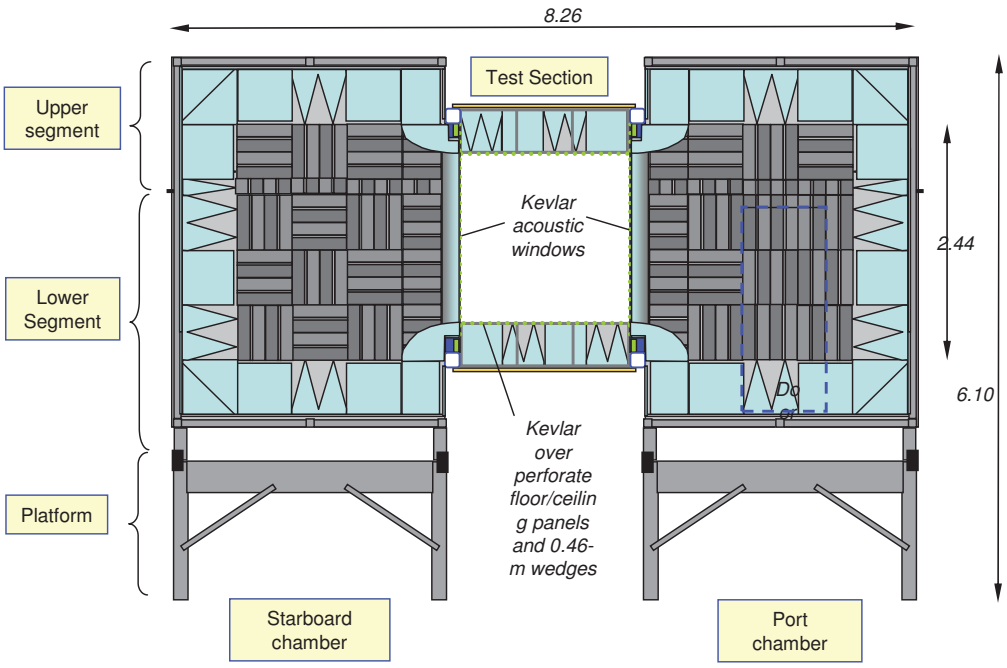

Figure 3. Cross section through the anechoic chambers and test section looking downstream. Dimensions in meters.

Figure 4. Interior of the anechoic test section as seen from downstream. An airfoil model installed with end plates and the partially installed trailing edge hot-wire traverse are visible.

Figure 5. Exterior view of the anechoic test section with the acoustic windows and the port side anechoic chamber removed. The starboard side anechoic chamber is visible in the background.

airfoil models tested in the anechoic test section have been built to completely span the vertical height of the test section with a tube of this size protruding from both spanwise ends. The axis of the tube, and thus the axis of rotation, of the model is located one quarter of the distance from leading to trailing edge.

Plain weave Kevlar 120 cloth (7.9 grams/m^2) is used to form the acoustic windows. This use of the material was pioneered by Jaeger et al. [7], who investigated different means of shielding a phased array microphone system embedded in the wall of a test section. They found this cloth to transmit sound with very little attenuation up to at least 25kHz. The Stability Tunnel is the first anechoic wind tunnel to employ this technology on a facility scale. The Kevlar cloth forming the acoustic windows is stretched on a 5.37 x 2.51 m tensioning frame to a tension of the order of 1500 N per linear meter. The Kevlar windows are sewn from 3 lengths of Kevlar cloth. When the windows are mounted, the two 40mm-wide seams run streamwise along the test section 0.19 to 0.28m below the upper wall and a similar distance above the lower wall.

Anechoic chambers are positioned on either side of the test section (Figures 2 and 3). Each chamber has a streamwise length of 6m, extends 2.8m out from the test section acoustic window, and has a depth of 4.2m. The chamber walls are constructed from medium density fiberboard, supported by a network of external steel beams, and lined internally with 0.610-m high acoustic foam wedges that eliminate acoustic reflections at frequencies above 200Hz. Quarter-elliptical foam sections surround the acoustic windows so as to form a smooth transition between the lower and upper walls of the test section, on the inside of the windows, and the acoustically treated

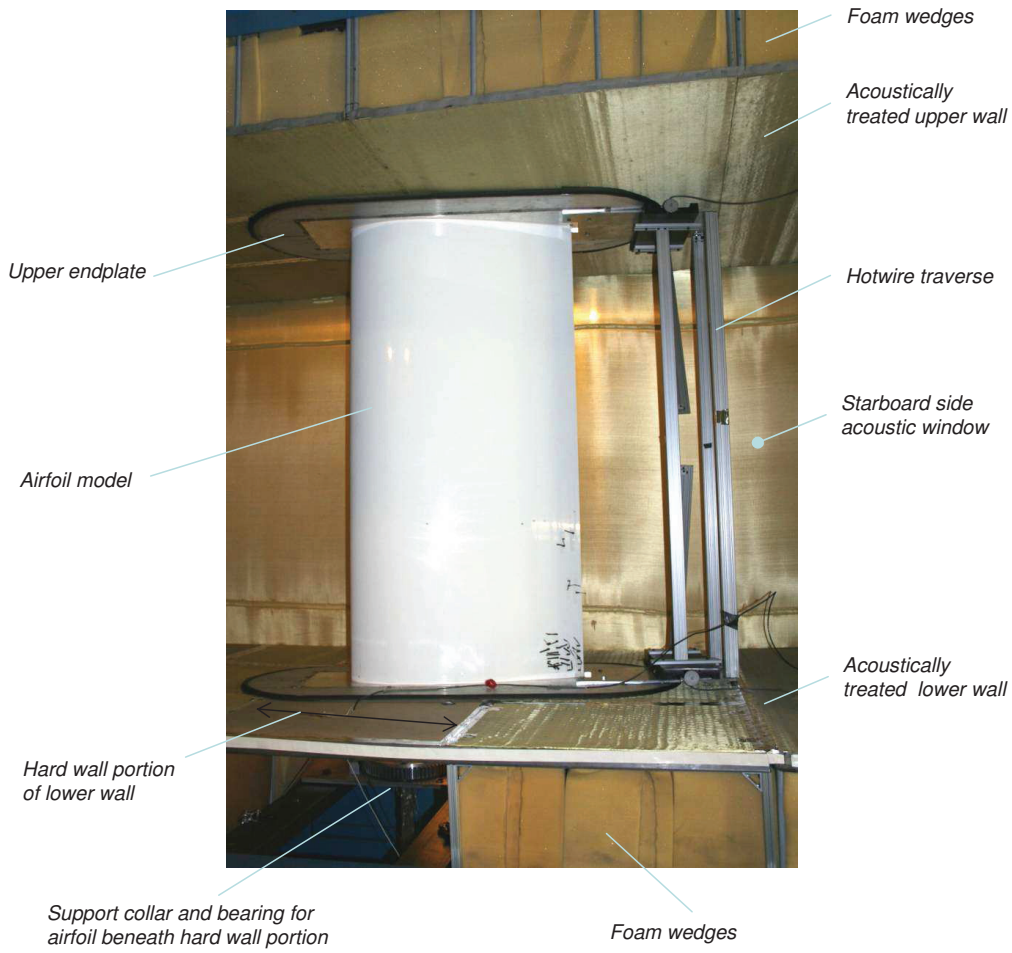

Figure 6. Photo of the central portion of acoustic test section with the starboard-side anechoic chamber and Kevlar acoustic window removed. An airfoil model installed with end plates and the trailing edge hot-wire traverse are visible.

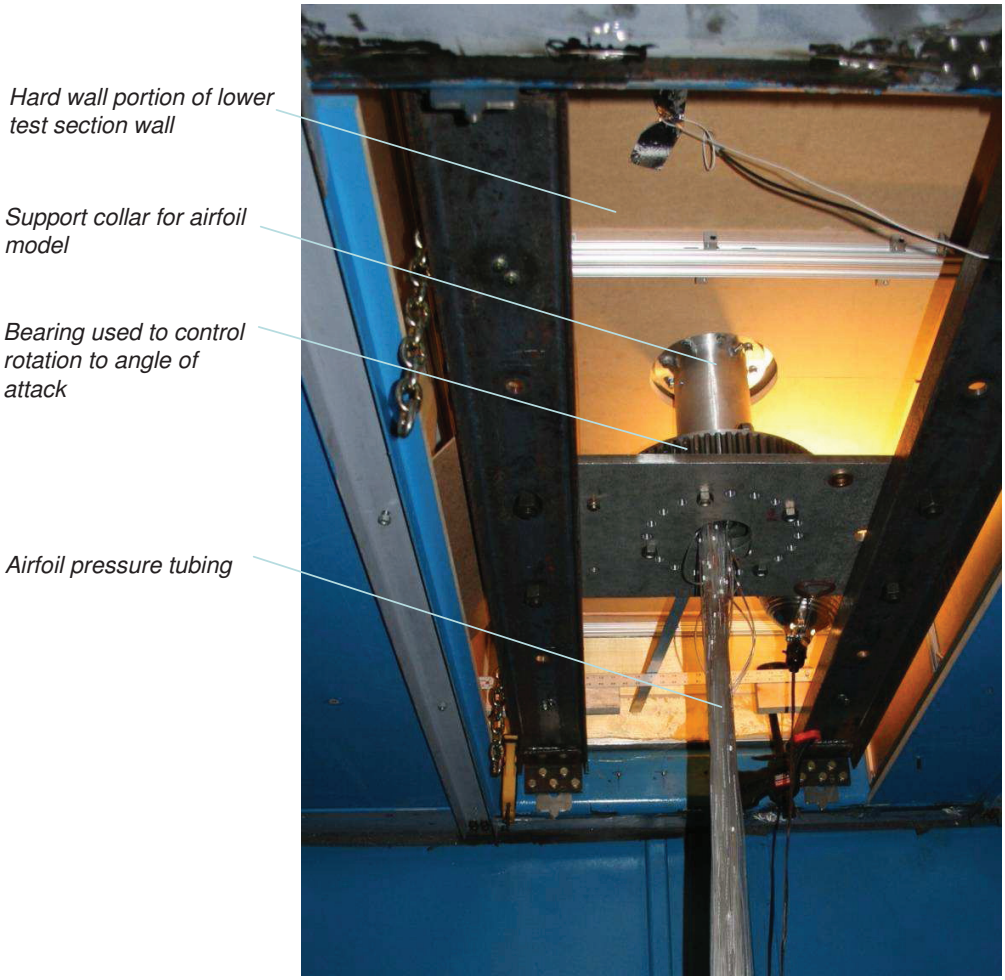

Figure 7. Photo taken from beneath the test section, showing the collar and bearing arrangement that form the airfoil mount.

walls of the anechoic chambers on the outside of the acoustic windows. The chamber sections are designed to seal to the sides of the test section, so as to minimize any net flow through either acoustic window. In practice, breaks in the seal are present.

Calibration information

The anechoic system was constructed and first installed in the Stability Wind Tunnel in 2006, since which further work on the system, on the acoustic treatment of the rest of the tunnel circuit, and on the calibration of the facility has been underway. Details of the calibration are given in Crede [8], Staubs [9], and Remillieux *et al.* [10], and summarized here. Figures 8(a) and 8(b) show empty test-section background noise levels in the starboard-side anechoic chamber as a function of flow speed. Note that noise levels in the port side chamber are almost identical. These measurements were made 1.9m from the center of the starboard-side acoustic window using a single 12.7mm diameter B&K microphone. Note that at the lowest speed (11.2m/s) the tunnel is quiet enough that the spectrum is dominated by the electrical noise of the microphone system and thus, in this specific case, the overall shape of this spectrum should not be taken as an indicator of actual acoustic levels. Below 200Hz background levels are mostly associated with fan tones. Above 200Hz the background noise is primarily broadband and is believed to be due to a combination of noise sources including the fan, turning vanes, and scrubbing noise from flow surfaces in and around the test section.

In an effort to accurately determine the absolute self-noise levels of the model tested, a procedure for amplitude calibration of the microphone phased array was developed for this new facility. In addition to determining the array sensitivity, corrections were measured to account for the noise attenuation effects of the Kevlar and the shear layer by Remillieux et al. [10]. The correction factors to account for the loss through the shear layer and the Kevlar window must be added to the array output. That is,

$$SPL_{True}(dB) = SPL_{Measured} + \Delta_K + \Delta_F, \tag{1}$$

where SPL_{True} is the actual level at the array position, $SPL_{Measured}$ is the array output, and Δ_K and Δ_F denote the corrections for the loss through the Kevlar window and the flow effects, respectively.

Figures 9(a) and 9(b) show the corrections as a function of frequency in 1/3rd octave bands. In these figures, a positive value of the curve indicates the loss, in decibels. Due to the small noise source used in this calibration, results below 2500 Hz are not very reliable. In Figure 9(a), the losses through the Kevlar window should converge to zero at low frequencies and thus the results were curve fitted (dashed line). Figure 9(b) depicts the losses due to the shear layer at Mach 0.12 (solid curve), at 0.15 (dashed curve), and 0.17 (smaller-dashed curve), as a function of frequency. The results indicate a weak dependence of the losses with frequency while increasing with flow speed.

The foam treatment on the anechoic chamber walls was designed to absorb sound above approximately 190 Hz. Measurements of sound below this frequency are contaminated to some degree by reflection from the chamber walls. An experiment was performed where sound was generated from a spherical speaker placed within the wind tunnel test section. Microphone mea-

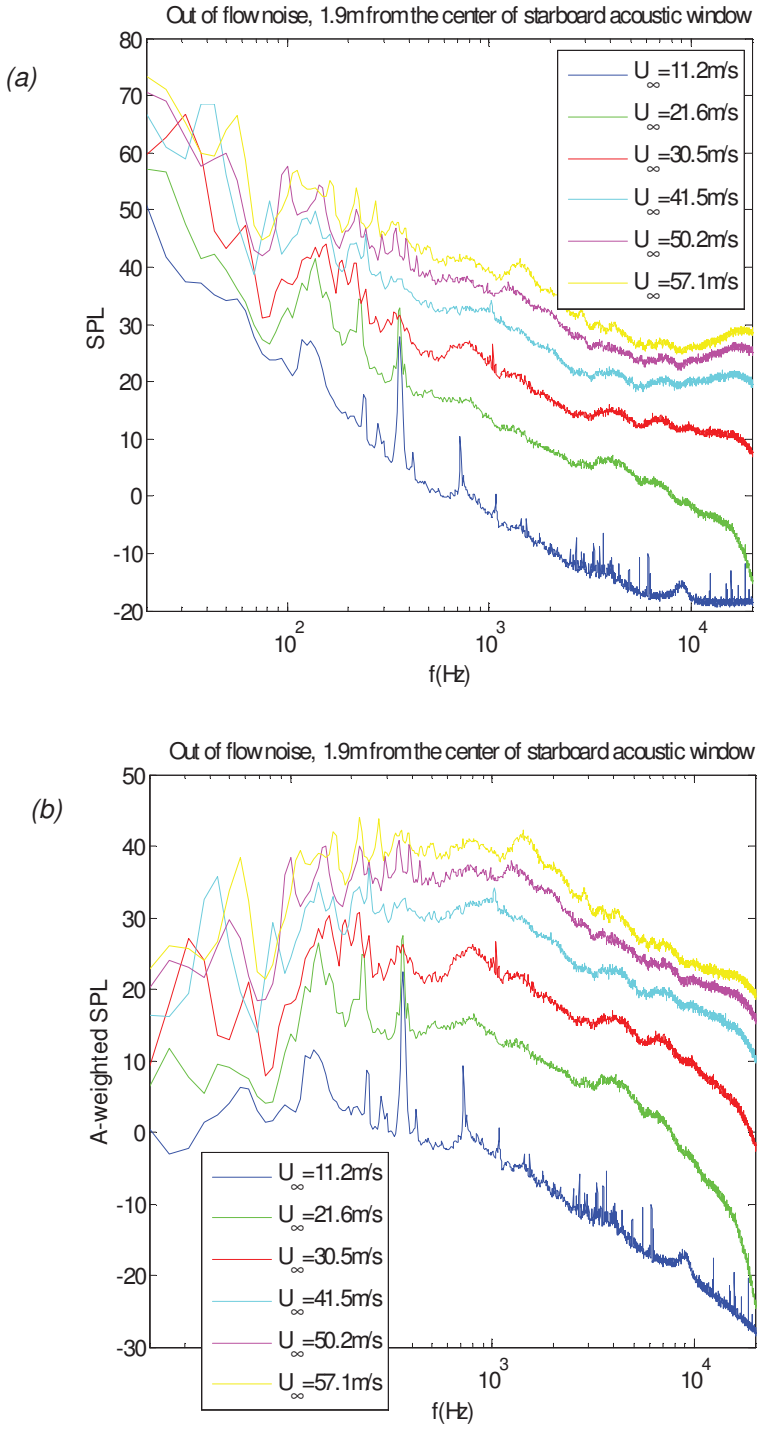

Figure 8. Out-of-flow noise levels in the starboard-side anechoic chamber 1.9m from the center of the acoustic window (2.7m from the test section center), as a function of flow speed in the empty test section. (a) 1 Hz bandwidth SPL. (b) 1 Hz bandwidth A-weighted SPL.

surements were made of the noise signal at the same array location used in the present airfoil experiments. From these measurements, the chamber wall impedance was derived as a function of frequency, and used to estimate the amount of correction to the measured noise intensity that would be required to account for reflection from the back chamber wall. This estimate is shown in Figure 10. The estimated corrections are less than 2 dB for frequencies greater than 100 Hz, with peaks associated with destructive and constructive interference appearing at lower frequencies. These corrections give confidence in the quality of the measured noise above 100 Hz, and provide guidance for interpretation of lower frequency measurements. Since this analysis does not consider reflections from the chamber floor or ceiling, the reflection corrections are considered approximate, and were not actually applied to any of the data presented herein.

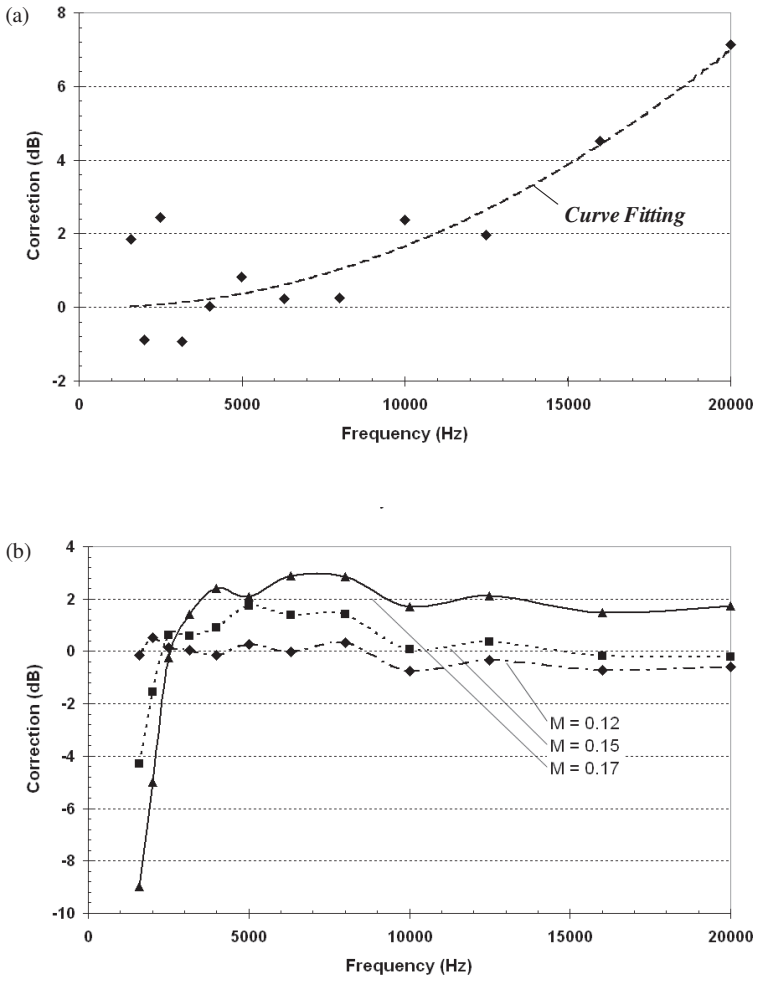

Figure 9. Attenuation of sound passing through the (a) acoustic Kevlar windows and (b) shear layer as a function of frequency in 1/3 octave bands.

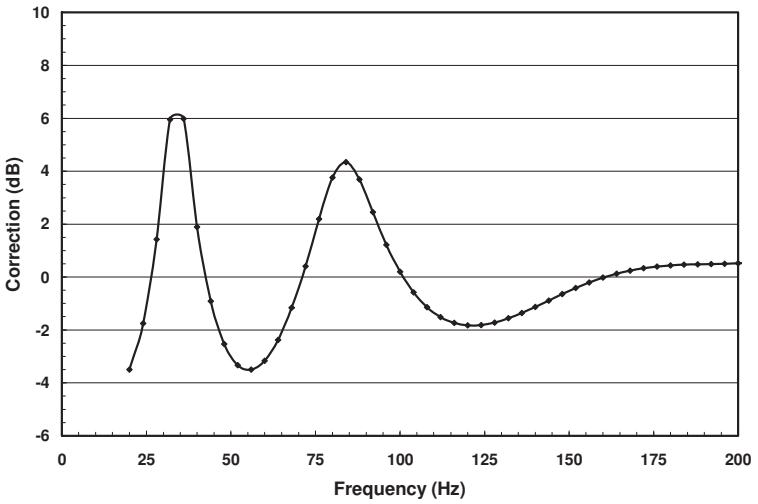

Figure 10. Estimated correction required to account for reflection of an acoustic wave emanating from a point source within the test section, reflecting off the anechoic chamber back wall, then traveling to the microphone array location.

2.3 Airfoil Models

The aerodynamic and acoustic measurements were performed on two airfoil models, a DU97-W-300 and a DU97-flatback, shown in Figure 11. The DU97-W-300 surface coordinates were obtained from Delft University of Technology (TU-Delft) upon request. The DU97-flatback shape was constructed by smoothly adding thickness about the aft 50% of the camber line, resulting in a blunt base with a width of 10% chord. The models, constructed by Novakinetics LLC, were designed to span the complete vertical height of the test section. They have a 1.8m span and 914mm chord and are built around a 88.9-mm diameter steel tube that forms a spar centered on the quarter chord location. The models have a fiberglass composite skin and a fill of fiberboard and polyurethane foam. The steel tube projects 166mm from the ends of each airfoil and was used for mounting. Novakinetics proof tested a similarly built model to a load of 27kN evenly distributed across the span, this being much larger than the maximum expected aerodynamic load. Deflection at this load at center span was approximately 5mm. The models were measured using a Faro Fusion CMM machine with a 3 mm probe. The surface deviations from the design coordinates for both models were less than 0.5 mm over most of the surface, with maximum deviations of 2.5 mm (about 0.25% chord) near the trailing edges of both models.

Both models were instrumented with 80 pressure taps of 0.5mm internal diameter located near the midspan. The taps appeared free from burrs and other defects. The taps were connected internally to 1.6mm Tygon tubing that exited the model through the center of the steel tube. In order to provide access to the interior of the model in the area of the pressure taps, a hatch was provided on one side of the model, fixed in place using a series of flathead bolts countersunk into

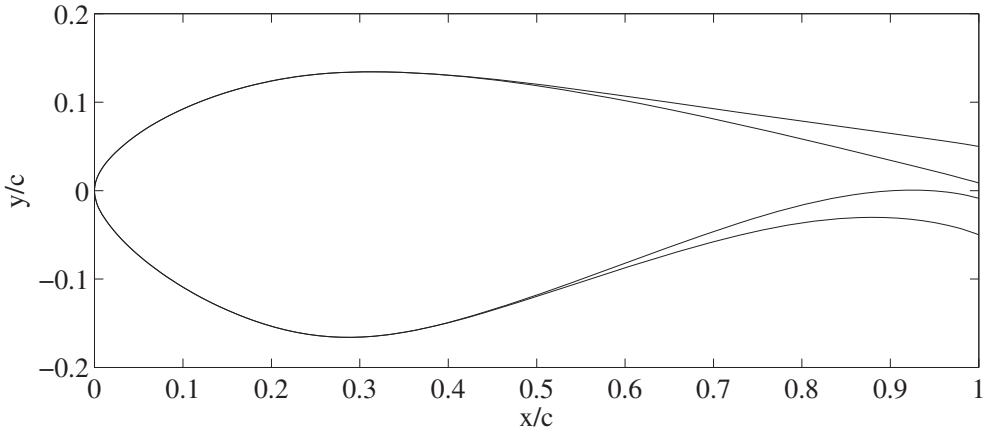

Figure 11. DU97-W-300 and DU97-flatback airfoil shapes.

the airfoil surface. Both bolt heads and the slight step at the edge of hatch were covered with 0.05mm Scotch tape during testing.

During testing, the airfoil models were mounted vertically in the test section, as shown in Figure 4, with the leading edge 3.33m downstream of the test section entrance and perpendicular to the oncoming flow. As also shown in this figure, end plates were attached to both ends of the model. These plates were 1.68m long in the chordwise direction, 0.66m wide, and had semicircular ends of radius 0.33m. The plates were attached to the ends of the model and rotated with it to angle of attack. At the edges of the endplates the roughly 20mm step to the surrounding wind tunnel wall was faired using closed cell foam strips with a quarter circle cross section mounted around the periphery of the end plates.

The origin of the geometric angle of attack of the models was determined using the measured pressure distribution, as discussed in Section 4.1. Angles relative to zero were set by using a lever arm and scale arrangement, attached to the bearing below the test section. The uncertainty of changes in angle of attack was estimated to be ± 0.2 degrees.

For certain measurements, the model boundary layers were tripped to ensure a stable and spanwise uniform transition location and a fully turbulent boundary layer at the trailing edge. Serrated trip tape (Glasfaser-Flugzeug-Service GmbH 3D Turbulator Tape) was applied with its leading edge at the 5% chord location on the airfoil suction side, and at the 10% chord location on the pressure side. The tape has a thickness of 0.5mm and is 12mm in overall width. The leading and trailing edges are cut to form aligned serrated edges with a 6mm distance between points.

For certain measurements with the flatback airfoil, a splitter plate was added to the trailing edge. The splitter plate attachment, illustrated in Figure 12, consists of an L-shaped aluminum angle that spans the entire trailing edge length of the airfoil. When attached, the 7.2mm thick base of the L is flush with the suction side of the blunt trailing edge, effectively extending the suction surface of the airfoil by 7.2mm. The other surface of the L projects from near the center of the blunt trailing edge, perpendicular to its surface. This 4.8mm thick splitter plate extends 89.6mm

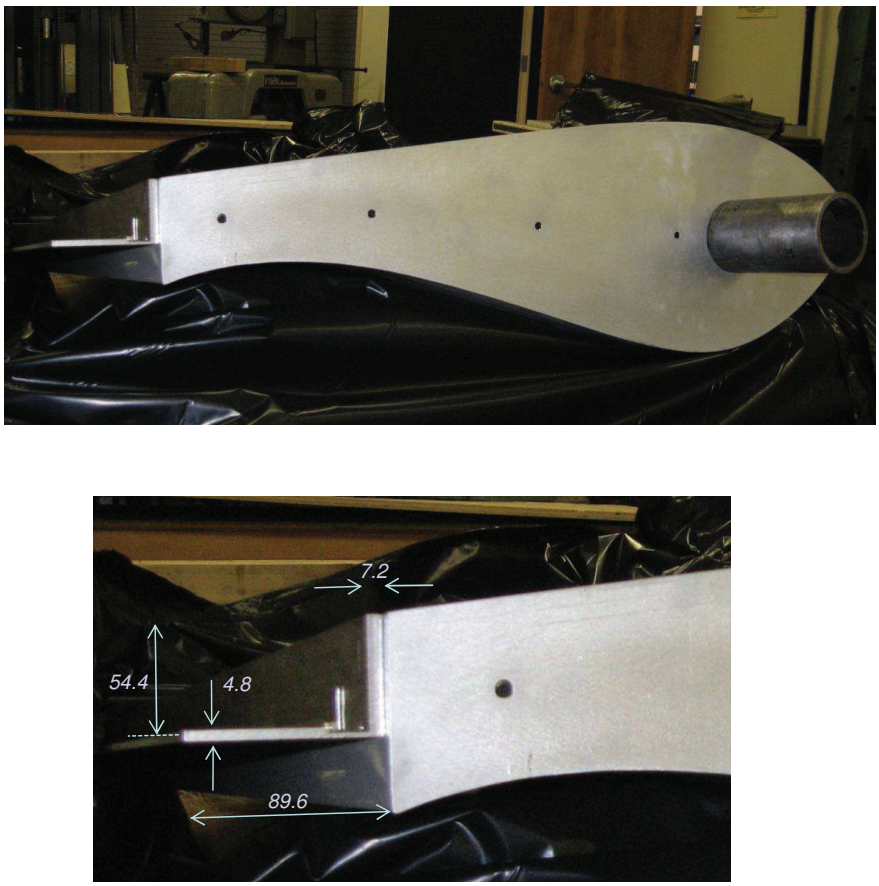

Figure 12. Splitter plate attachment used with the DU97-flatback. Dimensions in mm.

downstream from the trailing edge.

2.4 Aerodynamic Instrumentation

Reference conditions

During all measurements, various tunnel flow conditions were monitored. Flow speed was monitored using an 8-mm diameter reference Pitot static probe located near the exit of the contraction. The probe was positioned 0.035m upstream of the test section entrance, 1.22m from the floor and 0.23m from the port-side wall. The free-stream dynamic pressure was sensed using a Setra Model 239 pressure transducer. Temperature in the test section was monitored using an Omega Thermistor type 44004 (accuracy $\pm$0.2C) and the ambient absolute pressure was determined using a Validyne DB-99 Digital Barometer (resolution 0.01 in Hg).

Airfoil pressure distributions

A series of Setra model 239 pressure transducers (with ranges of $\pm$7.5 in H_2O, $\pm$15 in H_2O and $\pm$ 2.5 p.s.i.) were used to measure static pressures on the airfoil surfaces. These transducers were zeroed and calibrated against each other to minimize errors associated with differences in offset and sensitivity. Pressures from the taps on the airfoil model surfaces were directed through a Scanivalve system for measurement. The pressure from each tap, converted to voltage by the transducer, was measured simultaneously with the reference dynamic pressure using a 16-bit Agilent E1432 Digitizer. After switching the Scanivalve and allowing half a second for the pressure to settle, five records of 1024 samples were measured at a sampling rate of 3200Hz, over a total sampling time of some 3 seconds, in order to determine the mean pressure.

Airfoil wake measurements

The two-axis wind tunnel traverse shown in Figure 13 was used to position wake probes in the test section. Wake profiles were measured downstream of the midspan of the airfoil models using a rake of five Dwyer model 160 Pitot-static probes, with the intent of determining airfoil drag. The traverse mounts inside the test section and produces an overall solid blockage of about 10%. Probes are mounted well upstream of the traverse to avoid the region of flow acceleration associated with this blockage. These 3.18mm diameter probes, which normally include a 90 degree bend, were special-ordered in the straight configuration shown in Figure 14. The 5 probes were held at 25.4mm intervals across the flow using the bracket shown in Figure 15. The bracket, in turn, was held using a 32mm diameter sting attached to the traverse gear. The total distance from the upstream end of the traverse to the tips of the probes was close to 1.4m, the probe tips being some 340mm upstream of the bracket. To prevent relative movement of the probe tips, a thin spacer, manufactured from aluminum tape, was used to tie the probes together between 100 and 150mm from the probe tips.

Ten Omega Model PX277-30D5V pressure transducers set to a range of $\pm$7.5 inches of water were used to sense the pressures from the 5 probes relative to the wind tunnel free stream static pressure. The 5 stagnation and 5 static pressure coefficients sensed by the probe rake were calculated by averaging 30000 samples of the pressure transducer outputs recorded at a rate of 3200Hz. Voltage outputs from the 10 transducers, along with that from the wind tunnel reference transducer, were recorded using the same 16-bit Agilent E1432 Digitizer described above. A single Agilent VEE program was used to control the data acquisition, the traverse position and the data processing and saving. Prior to obtaining each rake profile, measurements were made with no flow in order to set the transducer offsets. Measurements were made with the probe rake oriented so that the 5 probes simultaneously recorded pressures from 5 different positions across the wake, minimizing the number of profile points needed.

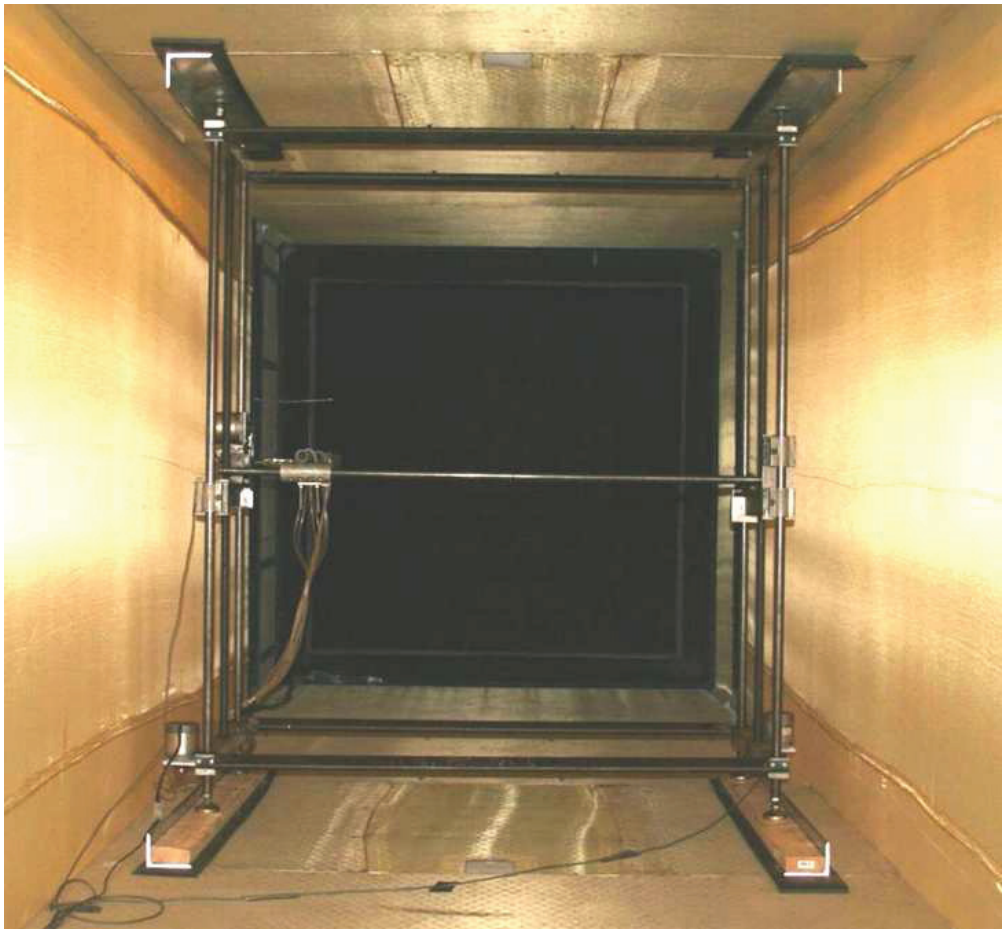

Figure 13. Photograph showing the traverse gear mounted in the anechoic test section (looking upstream).

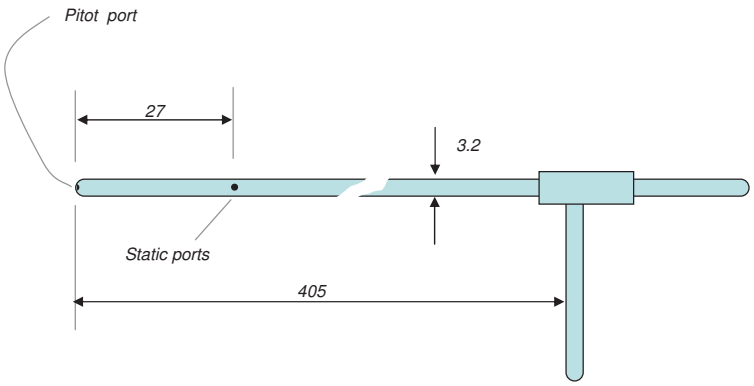

Figure 14. Dwyer 160 pitot static probe in straight configuration. Dimensions in mm.

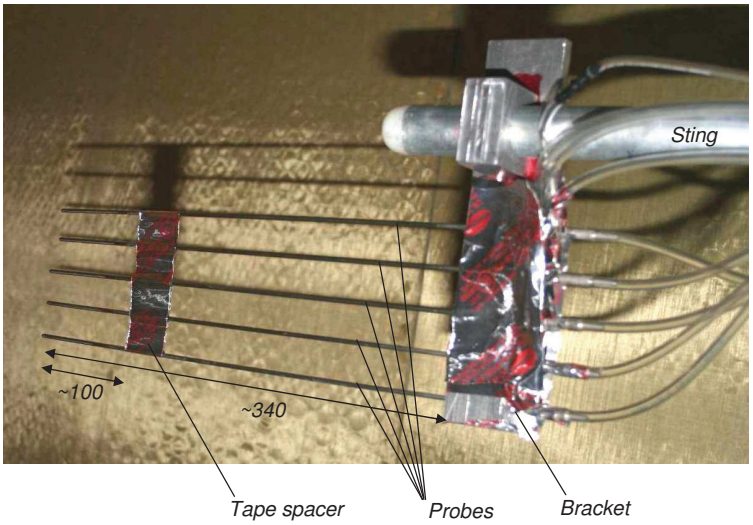

Figure 15. Pitot static probe rake detail (dimensions in mm).

Hot wire anemometry

Hot-wire profiles were measured in the vicinity of the trailing edge of the DU97-W-300 airfoil using single hot-wire probes. The probes were positioned using the specially-built traverse pictured in Figure 16. The traverse is powered by two synchronized, stepper-motor driven, linear stages mounted to the airfoil endplates downstream of the trailing edge. Probes are held using a 12.7mm thick strut mounted across the airfoil span some 330mm downstream of its trailing edge. The strut connects the two stages and traverses with them. A single angle bracket rigidly holds the 4.6mm diameter hot-wire probe stem, positioning the hot-wire at mid-span immediately downstream of the trailing edge. Additional diagonal beams (also 12.7mm thick), attached to the strut above and below the probe (Figure 16) and connected to the stages, add rigidity to the probe support to minimize vibration. A further non-traversing 25.4mm-thick strut with rounded leading and trailing

edges is attached 180mm downstream of the probe support, fixing the distance between the stages. The entire assembly rotates to angle of attack with the airfoil and endplates.

One shortcoming of this traverse arrangement is that the traverse structure experiences an unsteady loading should the airfoil wake impinge on one or both of the spanwise struts. This loading can then lead to probe vibration. While this does not appear to be a limiting factor for sharp trailing-edge models (that generate relatively weak wakes) the more intense wake produced by the blunt trailing edge of the DU97-W-300 may have resulted in some low amplitude vibration. While this vibration could not be observed directly (probes were monitored using a zoomed video camera located on the test section wall) there is some evidence in spectral measurements made at certain conditions. This effect was overwhelming for the DU97-flatback airfoil. The very intense wake shed from the blunt trailing edge of this airfoil produced vibrations of the traverse or jarring of its structure (enough to break probes) that simply could not be suppressed by adjusting its structure or the probe support. Hot wire measurements were therefore not made for the flatback airfoil.

A straight type single hot wire probe, either an Auspex AHWU-100 or a TSI type 1210-T1.5, was used for all measurements. Probes were balanced and operated using a Dantec 90C10 Streamline bridge system and used to obtain mean velocity, turbulence quantities, and spectra. The Agilent E1432 16-bit digitizer was again used for data acquisition. Hot wire calibration, traversing and the data acquisition were all controlled using Agilent VEE programs written in-house. Flow temperature was monitored continuously during hot wire measurements and corrections were made using the method of Bearman [11].

Hot-wire measurements were used to reveal the flow and turbulence structure in the trailing edge boundary layer relative to the local edge velocity, rather than in absolute terms. For this reason hot wire probes could be calibrated by positioning them in the potential flow region outside the airfoil boundary layer (saving much test time). Here the hot wire was calibrated by determining its output voltage as a function of the tunnel free stream speed, and fitting this to King's law with an exponent of 0.45. While the flow speed at the calibration points was not equal to the tunnel free stream, they were expected to be closely proportional. In effect, this means that subsequent hot wire velocity and turbulence measurements (after dividing by the tunnel freestream velocity) were obtained normalized by the velocity at the calibration point U_{cal}. Except for stalled conditions (where no boundary layer edge could be observed), data were then subsequently re-normalized on the observed edge velocity U_e.

Each boundary layer hot wire profile consisted of measurements at some 40 points, typically covering about 60mm in the direction normal to the airfoil upper or lower surface. Mean velocity and turbulence intensity were obtained by averaging some 20 records, each comprising 1024 points, measured at a rate of 3200Hz.

2.5 Acoustic Instrumentation

Acoustic data was collected using the 63-microphone phased array shown in Figure 17. This array has a star configuration consisting of 7 arms with 9 microphones per arm. The inner and outer

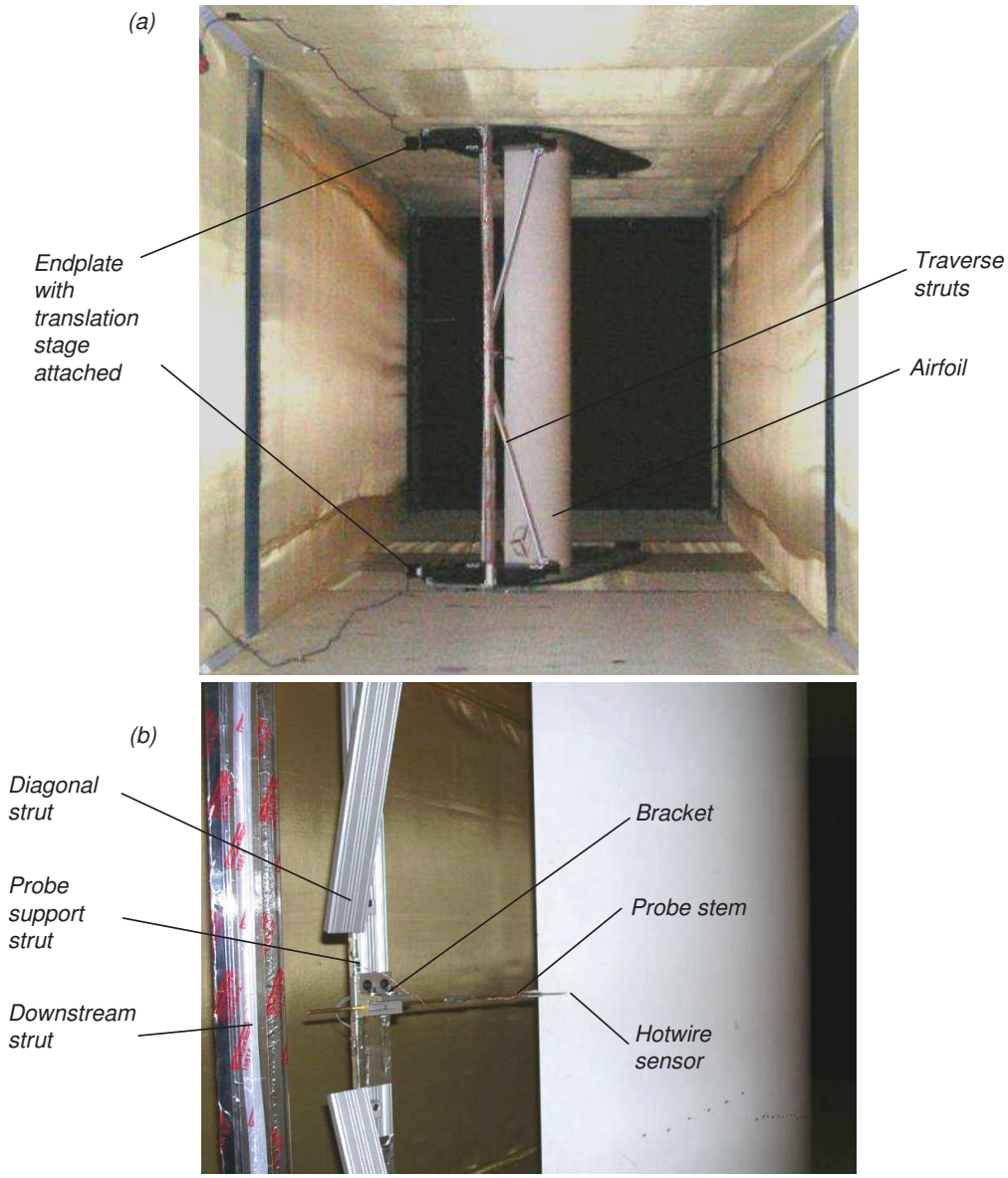

Figure 16. Photographs of the hot-wire traverse.

Figure 17. View from inside the port-side anechoic chamber showing microphone phased array.

diameters are 0.25m and 1.5m, respectively. The array pattern is shown in Figure 18. The array center body is provided with a laser pointer that projects a laser dot along a line perpendicular to the array plane passing through the array origin. This laser pointer was used for alignment purposes. The microphones of the phased array (Panasonic WM-60AY Electret microphones) have a flat frequency response from 200 to 18000 Hz. The microphone signal rolls off steeply at 18 kHz.

The array resolution and signal-to-noise ratio was determined by computing the point spread function for all the 1/12th octave bands in the 500 to 5000 Hz frequency range. The array point spread function at a distance of 3.0 meters from the array is plotted in Figure 19 for four 1/12th octave bands in the frequency range. The array resolution and signal-to-noise ratio as a function of the frequency for a plane 3 meters from the array is shown in Figure 20.

Phased array data was acquired using a 64-Channel Agilent Data Acquisition System. The raw data consists of the time series of the 63 array microphones for each run. A total of 50 records of 16384 points each were acquired for each microphone at a sampling frequency of 51200 Hz.

A conventional beamforming frequency domain algorithm with diagonal removal was used to generate the acoustic maps. The algorithm incorporates the convective effect of the flow in the test section and the flow velocity discontinuity between the test section and the anechoic chamber. This algorithm has been used in previous experiments at Virginia Tech (Remillieux et.al.[12]).

The microphone phased array was installed in the starboard-side chamber for all cases measured. Figure 21 shows the position of the array relative to the model.

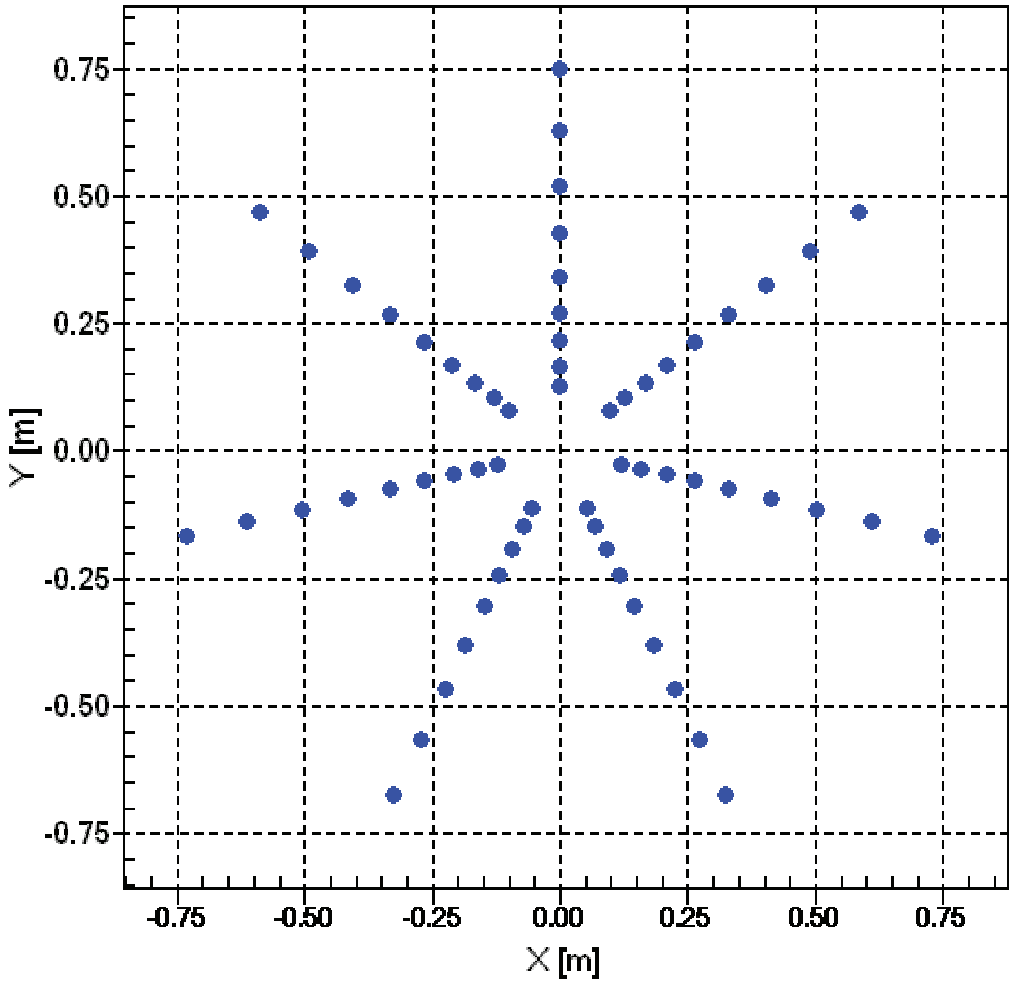

Figure 18. Microphone phased-array pattern.

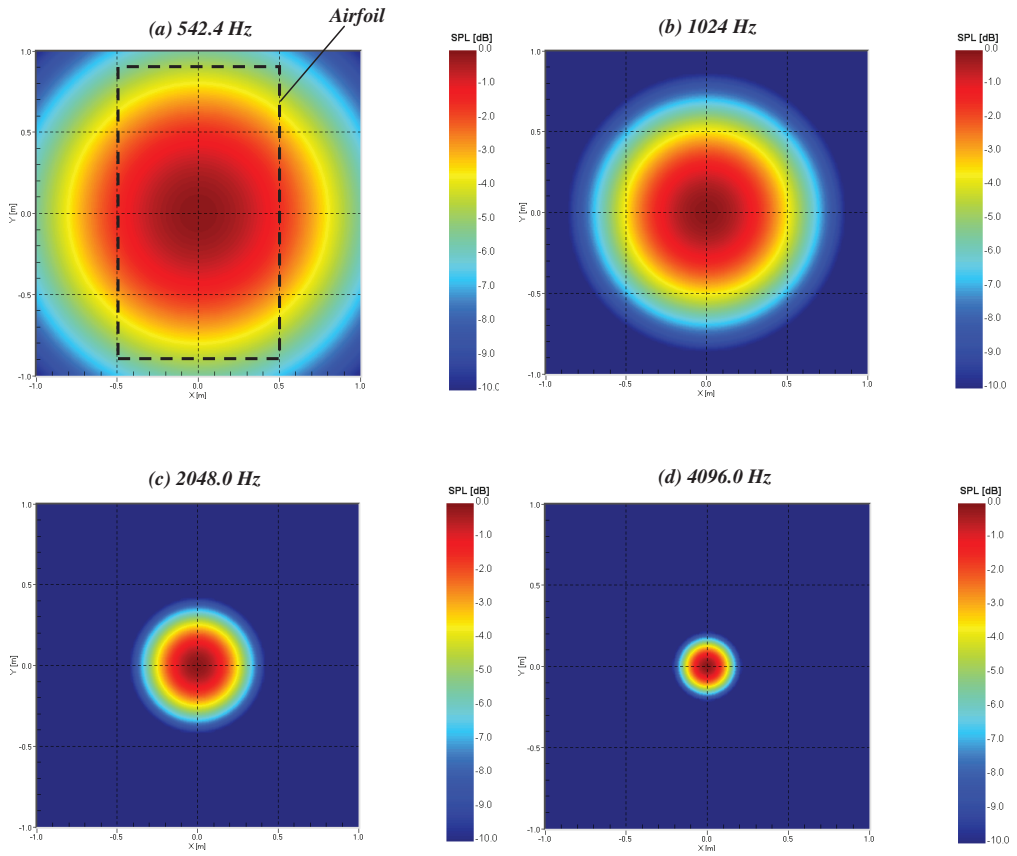

Figure 19. Array point spread function for 1/12th octave bands with center frequencies at (a) 542.4, (b) 1024.0, (c) 2048.0, (d) 4096.0 Hz at a distance of 3.0 meters. Flow in the tunnel section is not accounted for in these results.

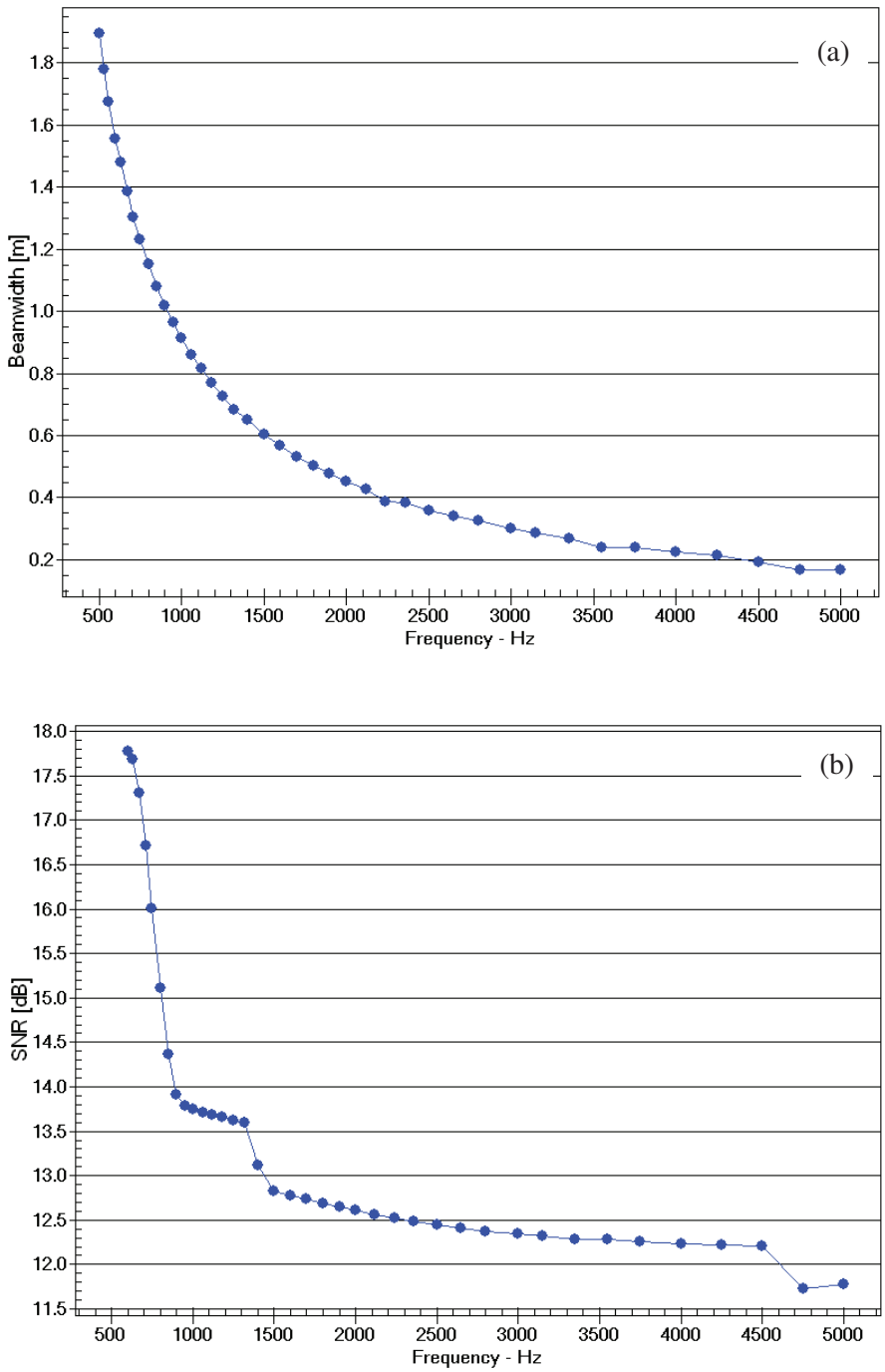

Figure 20. Array (a) resolution or beamwidth and (b) signal-to-noise ratio in 1/12th octave bands for the 500-5000Hz frequency range at a distance of 3.0 meters. Flow in the tunnel section not accounted for in these results.

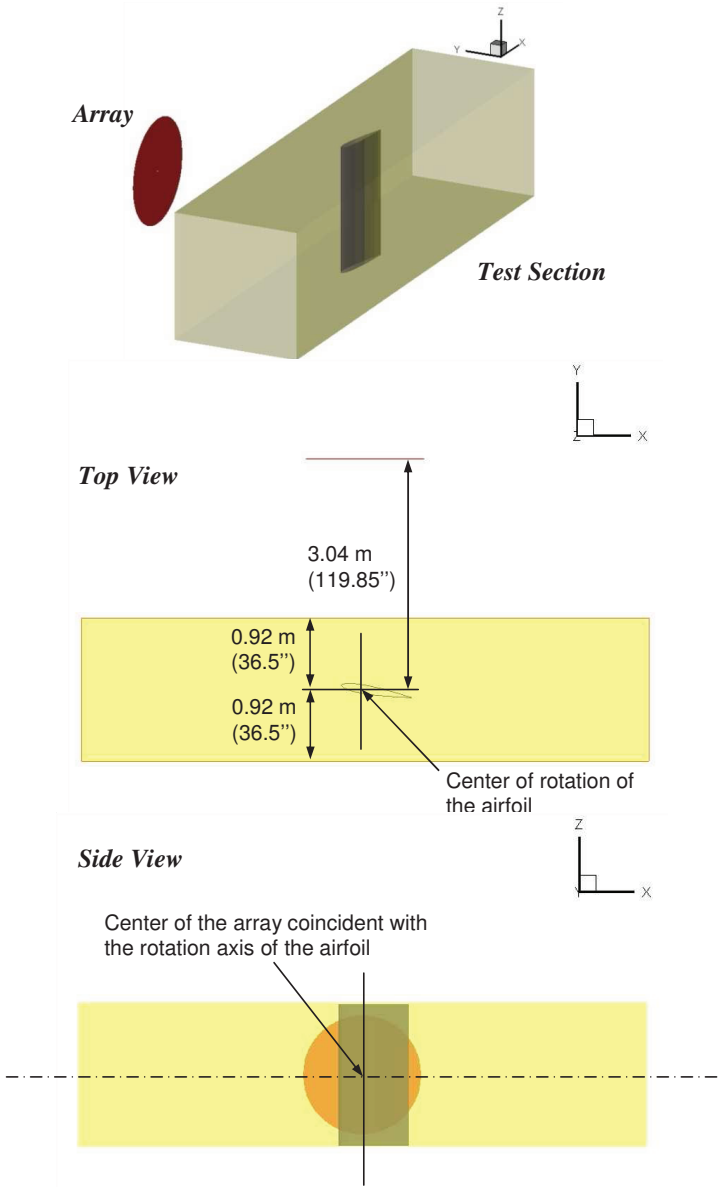

Figure 21. Position of the array on the starboard side used in all runs.

3 Correction of Aerodynamic Data

Previous airfoil aerodynamic measurements in the acoustic test section had involved models with a smaller chord and/or smaller maximum thickness than the present models. In these previous tests aerodynamic data were corrected using a simple downwash correction applied to the angle of attack, similar to corrections applicable to the case of a small model in an open jet wind tunnel. In the present tests, with larger and relatively thick airfoils, the simple downwash correction proved inadequate. This prompted a companion effort to derive porous wall interference corrections for the acoustic test section; this effort and the resulting corrections are described in detail in Appendix A.

The porous wall interference corrections were derived using a combination of measurement, theory, and Computational Fluid Dynamics (CFD) modeling. Due to resource and cost constraints, the effort was focused on the case of the DU97-W-300 at a nominal free stream velocity of 30m/s. A key assumption in the analysis is that the transpiration flow as a function of pressure difference across the porous Kevlar wall is not a function of the free stream velocity. As detailed in Appendix A, the resulting corrections work very well in correcting the data taken at 30m/s. However, the data taken at higher tunnel velocities do not appear to follow the same correction, based on comparison to the TU-Delft data set [5], limited data taken in the Virginia Tech Stability Wind Tunnel solid wall test section, and comparisons with CFD results. For this reason, the aerodynamic data are divided into two sets.

The first set corresponds to free stream velocities of between 28 and 30m/s, where the corrections are deemed to be valid and the data may be interpreted as accurate (within measurement uncertainties) in an absolute sense. This data corresponds to a chord Reynolds number range of $1.58 \times 10^6 \leq Re_c \leq 1.86 \times 10^6$. The second set of data is for free stream velocities between 42 and 60m/s, or $2.38 \times 10^6 \leq Re_c \leq 3.21 \times 10^6$. Modification to the existing corrections is deemed necessary for this set of data. However, the corrections are estimated to be relatively small and are not expected to influence major trends or sensitivities, except those tied directly to the free-stream velocity. For example, performance of the DU97-W-300 may be compared to that of the DU97-flatback, but Reynolds number effects for a single given airfoil will not be meaningful.

In the following section, the data for 28 m/s $\leq U_\infty \leq$ 30 m/s are presented and labelled as *corrected* data, while the data for 42 m/s $\leq U_\infty \leq$ 60 m/s are presented and labelled as *uncorrected* data.

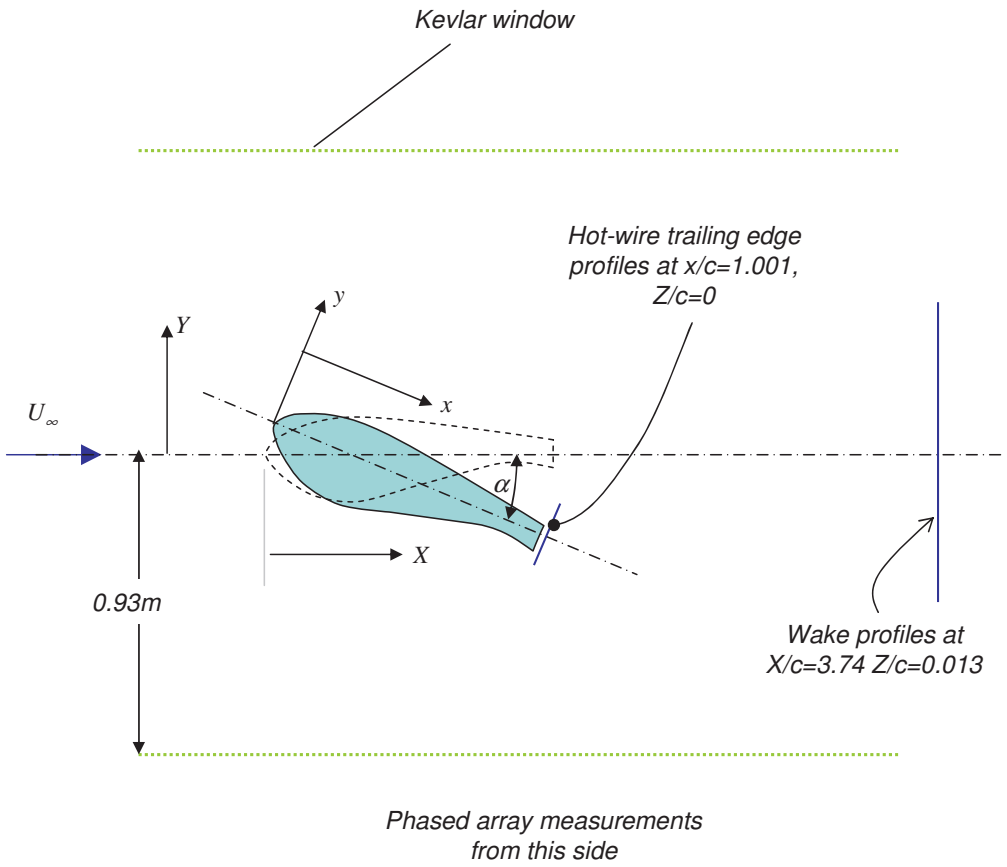

Figure 22. Coordinate systems and measurement locations for the tests. Z coordinate is measured from center-span out of the paper.

4 Aerodynamic Results

Figure 22 shows the coordinate systems used in presenting the results of the airfoil tests. The chord-aligned airfoil system (x,y) has its origin at the leading edge of the airfoil, that origin moving with the leading edge as the angle of attack is varied. This system is used to present mean pressure distributions measured on the airfoil and to define the locations of the trailing edge boundary layer measurements. The tunnel fixed system (X,Y,Z) has its origin at the midspan of the leading edge when the airfoil is at zero angle of attack. This system is used for the wake and phased array measurements. Note that in terms of physical orientation in the wind tunnel, the view shown in Figure 22 is that seen looking upward along the airfoil span, with the starboard-side chamber appearing at the bottom of the diagram.

Airfoil	Trip	α_{geom}, deg.	α_{eff}, deg.	U_∞, m/s	Re_c	Corr. C_l	Corr. C_m	Corr. C_d
DU97-W-300	No Trip	0.0	-0.4	30.0	1.76×10^6	0.26	-0.107	–
DU97-W-300	No Trip	6.7	5.7	30.0	1.86×10^6	1.00	-0.126	–
DU97-W-300	No Trip	10.3	9.2	28.4	1.64×10^6	1.43	-0.143	0.0163
DU97-W-300	No Trip	13.2	11.9	30.0	1.73×10^6	1.57	-0.118	–
DU97-flatback	Serrated Tape	5.2	4.4	28.7	1.60×10^6	0.83	-0.152	–
DU97-flatback	No Trip	12.8	11.6	28.9	1.60×10^6	1.94	-0.207	0.0509
DU97-flatback	Serrated Tape	12.8	11.6	28.5	1.58×10^6	1.74	-0.190	–
DU97-flatback/splitter	Serrated Tape	5.2	4.4	28.5	1.60×10^6	0.87	-0.146	–
DU97-flatback/splitter	Serrated Tape	12.8	11.6	28.8	1.59×10^6	1.86	-0.187	–

Table 2. Test matrix for aerodynamic measurements obtained for $28m/s \leq U_\infty \leq 30m/s$, with *corrected* force and moment coefficients.

4.1 Surface Pressure Measurements, $28 \leq U_\infty \leq 30$m/s

Table 2 lists the cases where $28 \leq U_\infty \leq 30$m/s and for which the mean pressure distributions were measured. The reported free-stream velocity, U_∞, is the measured quantity and is not corrected for blockage. Table 2 also gives the corrected force coefficients. Note that in all cases the calculations of lift and pitching moment coefficients for the DU97-flatback with splitter plate *do not* include the loads on the splitter plate, as the splitter plate itself was not instrumented.

For most of the measurements (including those at higher U_∞), the geometric angle of attack origin was determined using the following procedure. After installing the DU97-W-300 airfoil, it was placed approximately (by eye) at zero angle of attack. A trial pressure distribution was then measured at a Reynolds number of approximately 3.2 million. The measured mean pressure distribution was then compared to an inviscid panel method solution for the airfoil to establish the actual geometric angle of attack. The exact same procedure was used with the flatback airfoil without splitter plate. Geometric angles of attack with the splitter plate were taken to be the same as those without. The effective angle of attack was calculated using the porous wall downwash correction derived in Appendix A. Due to the approximate nature of the procedure for determining geometric angle of attack, uncertainty in both the geometric and corrected angle of attack for measurements using this technique is ±0.5 degrees. For measurements that were taken later in the test program and used to derive wall interference corrections, the angle of attack was measured directly and the resulting uncertainty is estimated to be ±0.2 degrees. These cases are the DU97-W-300 runs listed in Table 2 with $U_\infty = 30.0$m/s, and α_{geom} =0, 6.7, and 13.2 degrees.

Measured pressure distributions are presented in terms of the pressure coefficient

$$C_p = \frac{p - p_\infty}{p_{0_\infty} - p_\infty} = \frac{p - p_\infty}{\frac{1}{2}\rho U_\infty^2} \tag{2}$$

where p is the local pressure, p_{0_∞} and p_∞ are the reference freestream stagnation and static pres-

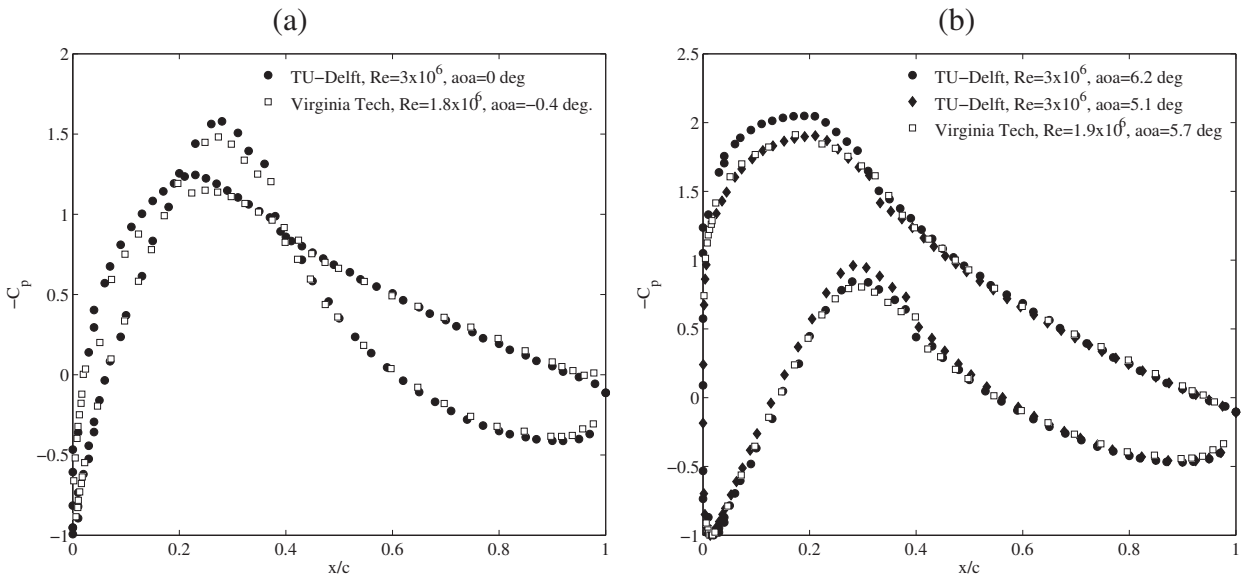

Figure 23. Comparison of corrected surface pressure distributions between TU-Delft wind tunnel data and measurements taken in the Virginia Tech acoustic test section.

sures, and U_∞ is the free stream velocity. Pressure distributions presented in this section are corrected for blockage and streamline curvature interference, as described in Appendix A. Figures 23 and 24 compare the present corrected pressure distributions with data taken in the TU-Delft low-speed, low-turbulence wind tunnel [5] at similar effective angles of attack. Generally good agreement is observed, with small differences that can be attributed to the difference in Reynolds number between the two data sets. This good comparison with what is considered a reliable data set gives confidence in the current measurements and wall interference corrections.

Figure 25(a) compares corrected surface pressure distributions between the DU97-W-300 and DU97-flatback at $Re_c = 1.6 - 1.8 \times 10^6$, with $\alpha_{eff} = 11.9$ deg. for the DU97-W-300 and 11.6 deg. for the DU97-flatback. The difference in angle of attack bewteen the two cases is less than the uncertainty in measured angle of attack, and differences are primarily due to the modified shape of the flatback. The primary difference between the two pressure distributions is the uniformly lower pressure over the suction surface of the DU97-flatback relative to the DU97-W-300. The flatback suction surface pressure near the trailing edge is lower than ambient pressure, indicating off-body pressure recovery that enables lower pressures (and higher lift) over the entire suction surface. Figure 25(b) indicates the effect of tripping the boundary layers near the leading edge for the flatback airfoil at this same angle of attack. The effect of the boundary layer trip is felt primarily near the leading edge, where the thicker turbulent boundary layer leads to a reduced suction peak, resulting in a modestly lower lift.

Figure 26 shows the corrected pressure distributions for the DU97-flatback with and without the splitter plate attachment at two different angles of attack. At $\alpha_{eff} = 4.4$ deg., the splitter

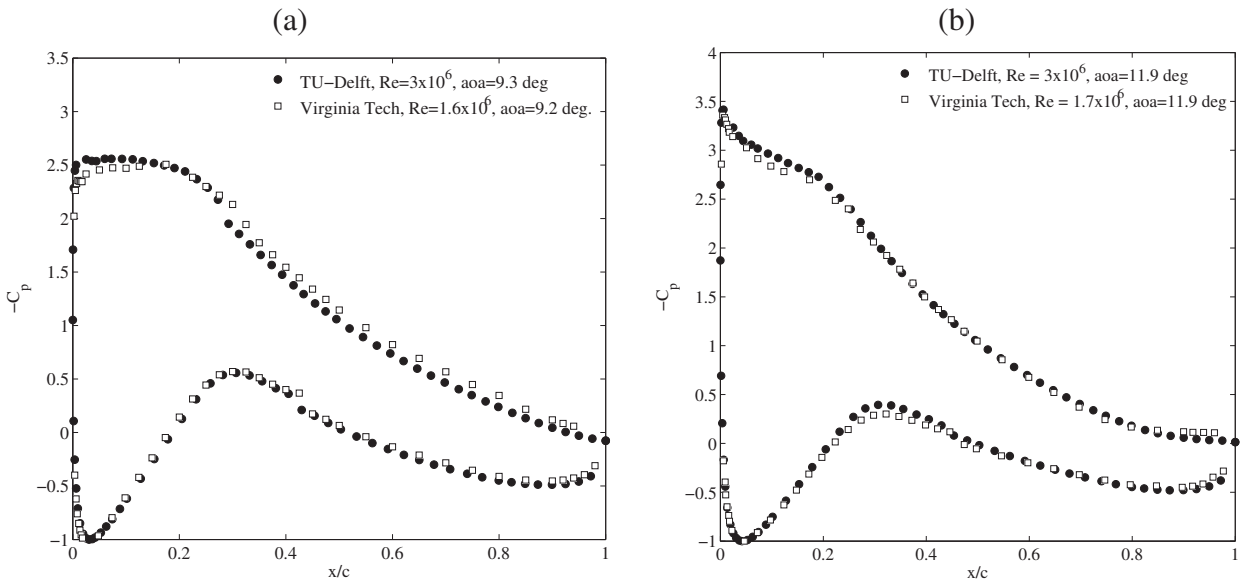

Figure 24. Comparison of corrected surface pressure distributions between TU-Delft wind tunnel data and measurements taken in the Virginia Tech acoustic test section.

plate increases the suction surface pressure at the trailing edge, appearing to maintain an attached suction surface boundary layer versus the possibly separated boundary layer seen on the flatback without splitter plate. This effect is not observed at the higher angle of attack. At both angles of attack, the splitter plate slightly increases the magnitude of the suction peak. Overall, these changes in pressure distribution appear to be minor. However, the lift coefficient will also depend on the details of the base pressure and the pressure distribution over the splitter plate itself, which were not measured.

The measured pressure distributions were integrated to estimate the lift and moment coefficients. To do this, the distributions were first interpolated to 200 points distributed around the airfoil contour. The base pressure on the blunt trailing edges was estimated from the average of the pressures measured closest to the trailing edge on either side. For the splitter plate cases, the integration was performed ignoring the contributions from the plate itself, so in this case the results only reflect the lift and moment experienced on the rest of the airfoil.

Figure 27 shows the corrected lift coefficient for the DU97-W-300 (no trip) and DU97-flatback (with and without trip) airfoils at $Re_c = 1.6 - 1.8 \times 10^6$, compared with the TU-Delft corrected wind tunnel data at $Re_c = 3 \times 10^6$. The DU97-W-300 lift coefficients fall very close to the TU-Delft data, despite the difference in Reynolds number. The DU97-flatback lift coefficients indicate that both the clean and tripped flatback have a higher maximum lift coefficient than the clean DU97-W-300. The trip reduces the DU97-flatback lift coefficient at 11.6 degrees angle of attack from 1.94 to 1.74. The DU97-flatback with serrated tape trip gives a lift coefficient close to that of the clean DU97-W-300 at 4.4 degrees angle of attack, and evidently has a steeper lift curve slope than the

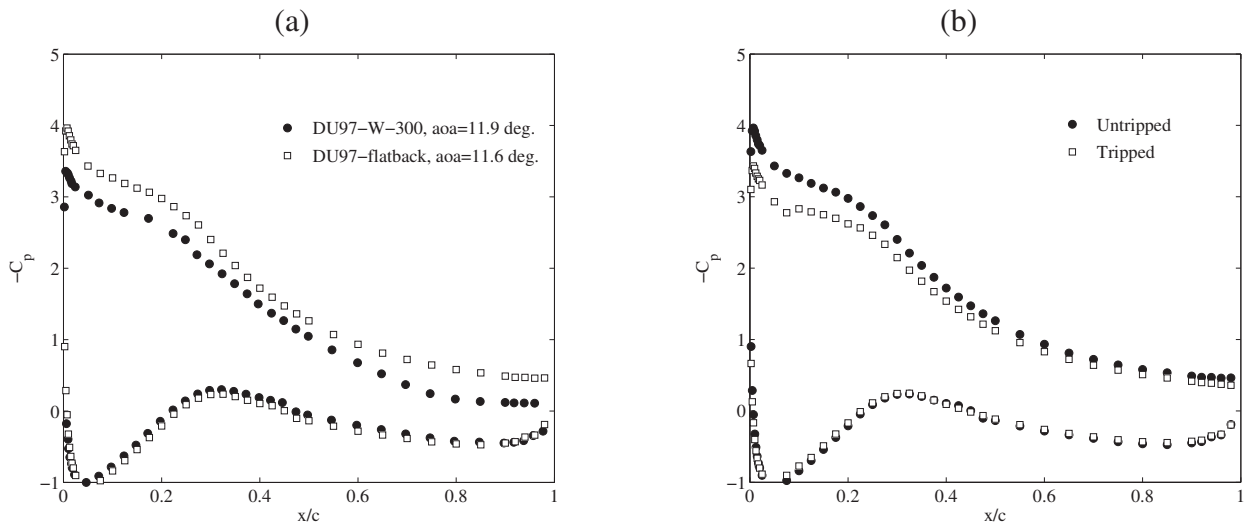

Figure 25. Corrected surface pressure coefficient distributions. (a) DU97-W-300 and DU97-flatback, $Re_c = 1.6 - 1.8 \times 10^6$, no trip. (b) DU97-flatback, $\alpha_{eff} = 11.9$ deg., $Re_c = 1.6 \times 10^6$.

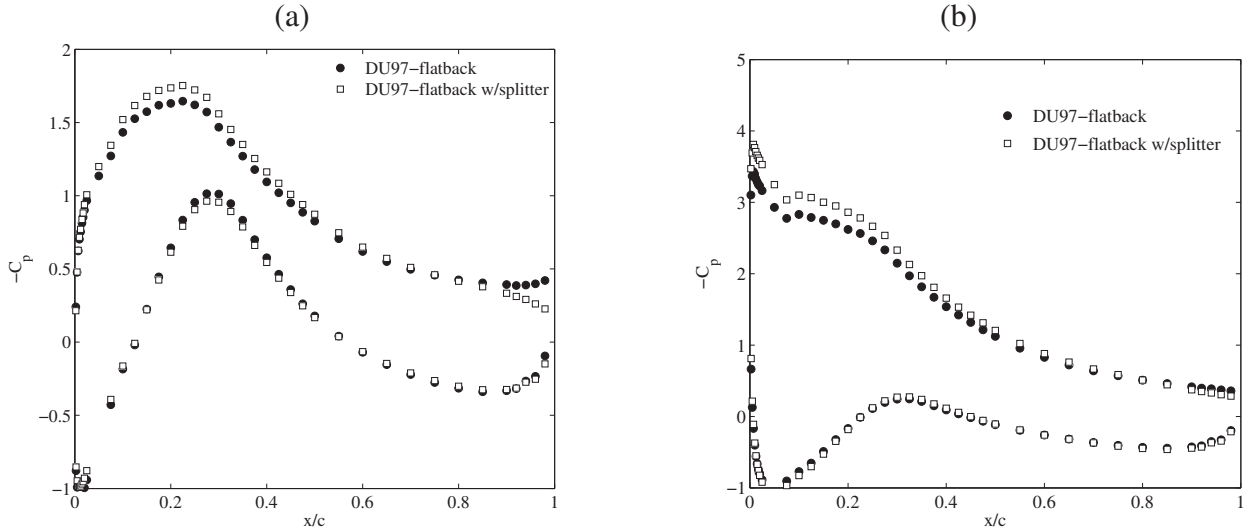

Figure 26. Corrected surface pressure coefficient distributions, for DU97-flatback without and with splitter plate, $Re_c = 1.6 \times 10^6$, serrated tape trip . (a) $\alpha_{eff} = 4.4$ deg. (b) $\alpha_{eff} = 11.6$.

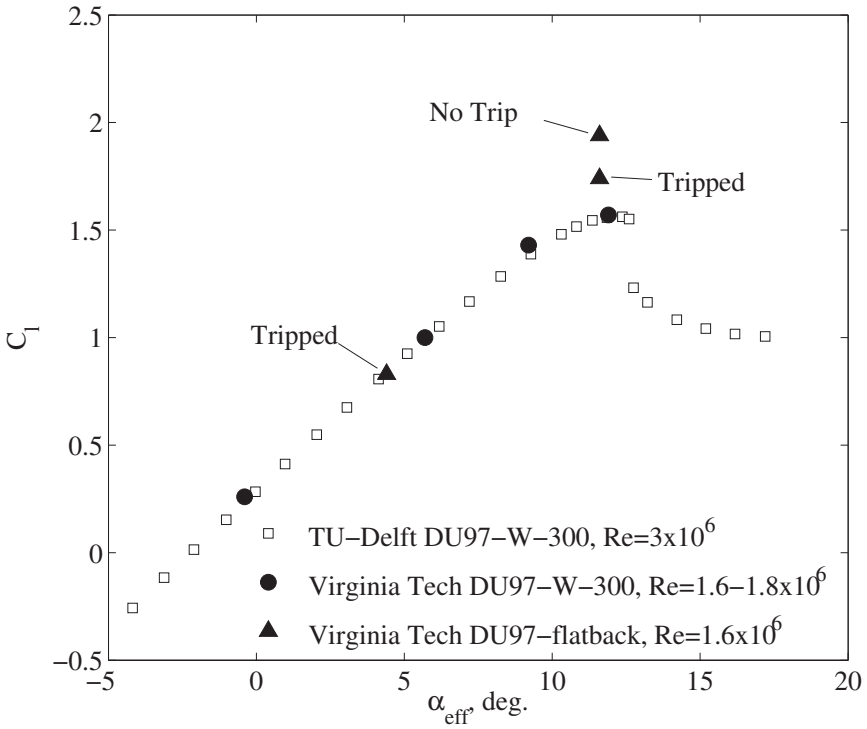

Figure 27. Corrected lift coefficient for DU97-W-300 and DU97-flatback airfoils with $28 \leq U_\infty \leq 30$m/s, compared with data for the DU97-W-300 taken in the TU-Delft wind tunnel.

clean DU97-W-300. Overall, the limited data shown in Figure 27 indicate that the flatback airfoil increases maximum lift coefficient and lift curve slope, and is not extremely sensitive to leading edge boundary layer transition at high angle of attack.

Figure 28 shows the corrected pitching moment coefficient for the DU97-W-300 (no trip) and DU97-flatback (with and without trip) airfoils at $Re_c = 1.6 - 1.8 \times 10^6$, again compared with the TU-Delft corrected wind tunnel data at $Re_c = 3 \times 10^6$. The present DU97-W-300 measurements are close to the TU-Delft data with some deviation evident at 9.2 degrees angle of attack. The DU97-flatback pitching moment is more negative (nose down) than the DU97-W-300 for both tripped and clean configurations. Tripping the boundary layer reduces the (negative) pitching moment at $\alpha_{eff} = 11.6$ degrees, due to the lower suction peak observed in Figure 25(b).

4.2 Surface Pressure Measurements, $42 \leq U_\infty \leq 60$m/s

Table 3 lists the measurement conditions for cases where $42 \leq U_\infty \leq 60$m/s. As mentioned previously, reliable wall interference corrections are not yet available for data at these higher free stream velocities. However, useful information can be gained by examining relative trends.

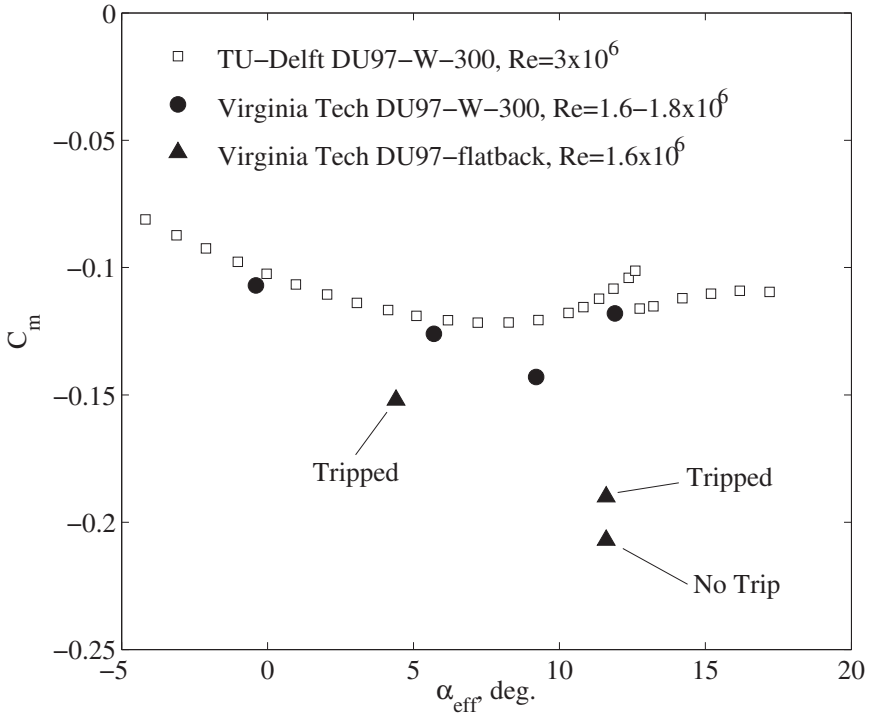

Figure 28. Corrected pitching moment coefficient for DU97-W-300 and DU97-flatback airfoils with $28 \leq U_\infty \leq 30$m/s, compared with data for the DU97-W-300 taken in the TU-Delft wind tunnel.

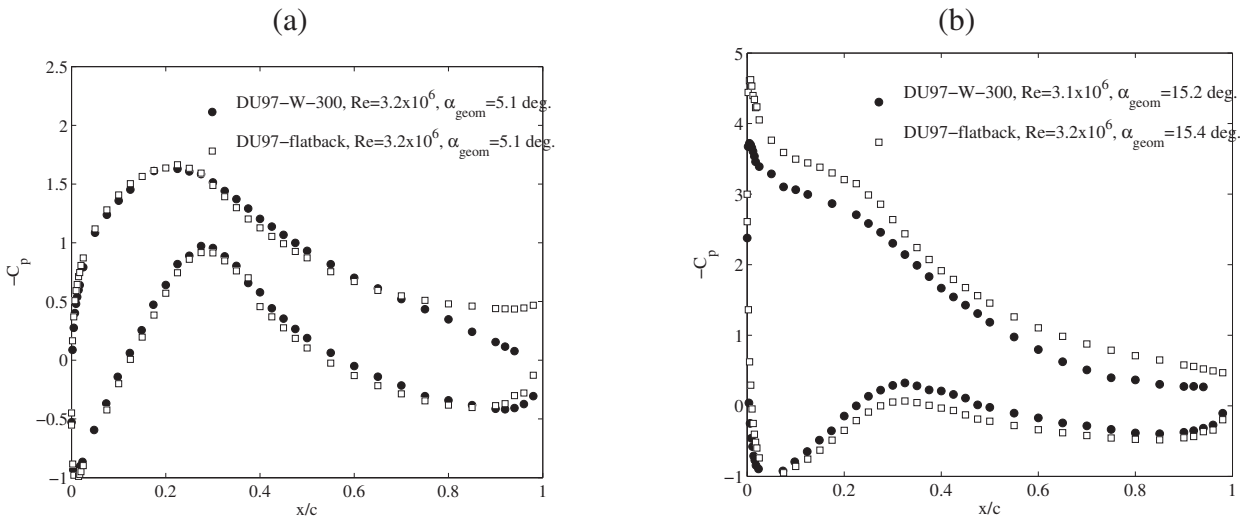

Figure 29. Uncorrected surface pressure coefficient distributions, comparing the DU97-W-300 with the DU97-flatback at the same or similar geometric angle of attack, $Re_c = 3.1 - 3.2 \times 10^6$, no trip.

Figure 29 compares uncorrected surface pressure coefficients at a chord Reynolds number of $3.1 - 3.2 \times 10^6$ for the DU97-W-300 and DU97-flatback. At the lower angle of attack (Figure 29(a)) , the pressure distributions deviate significantly only on the suction surface near the trailing edge. The suction surface pressure distribution on the flatback plateaus near the trailing edge and terminates at a pressure lower than free-stream pressure, while the DU97-W-300 pressure recovers to free-stream pressure near the trailing edge. In contrast, Figure 29(b) shows behavior similar to the lower Reynolds number case in Figure 25(a), where the flatback suction surface pressure is uniformly lower than that measured on the DU97-W-300.

The uncorrected lift coefficients for the DU97-W-300 and DU97-flatback at $Re_c = 3.1 - 3.2 \times 10^6$ are compared in Figure 30. These data show similar trends to the (corrected) lift coefficient data at lower Reynolds number. In particular, the flatback airfoil has a steeper lift curve slope and likely a higher maximum lift coefficient than the DU97-W-300. The sensitivity to leading edge boundary layer tripping is small and is less of an effect at this higher Reynolds number.

4.3 Wake Measurements

Stagnation pressure and static pressure profiles were measured through the airfoil wake at $X/c = 3.74$, approximately two chordlengths downstream of the airfoil trailing edges. Measurements were made for the configurations and conditions where drag coefficient is reported in Tables 2 and 3. Selected profiles of the pressure coefficients for the flatback with and without splitter plate are plotted against Y position measured relative to the wake centers Y_{cl} in Figures 31 and 32. Pressures

Airfoil	Trip	α_{geom}, deg.	U_∞, m/s	Re_c	Uncorr. C_l	Uncorr. C_m	Uncorr. C_d
DU97-W-300	No Trip	5.1	42.1	2.40×10^6	0.83	-0.140	–
DU97-W-300	No Trip	10.3	42.0	2.40×10^6	1.44	-0.160	–
DU97-W-300	Serrated Tape	10.3	42.4	2.38×10^6	1.40	-0.152	–
DU97-W-300	No Trip	5.1	56.0	3.16×10^6	0.81	-0.142	0.0112
DU97-W-300	No Trip	10.3	56.3	3.13×10^6	1.41	-0.165	0.0149
DU97-W-300	Serrated Tape	10.3	56.4	3.12×10^6	1.39	-0.158	–
DU97-W-300	No Trip	15.2	55.6	3.09×10^6	1.71	-0.132	–
DU97-flatback	No Trip	5.1	43.6	2.40×10^6	0.93	-0.179	–
DU97-flatback	Serrated Tape	5.2	43.7	2.41×10^6	0.93	-0.180	–
DU97-flatback	No Trip	12.8	44.0	2.40×10^6	2.09	-0.261	–
DU97-flatback	Serrated Tape	12.8	42.5	2.39×10^6	1.76	-0.196	–
DU97-flatback	No Trip	15.4	43.8	2.39×10^6	2.11	-0.209	–
DU97-flatback	Serrated Tape	15.4	42.6	2.40×10^6	2.27	-0.242	–
DU97-flatback	No Trip	5.1	58.6	3.20×10^6	0.91	-0.181	0.0635
DU97-flatback	Serrated Tape	5.2	58.6	3.21×10^6	0.90	-0.180	–
DU97-flatback	No Trip	12.8	59.3	3.20×10^6	1.89	-0.230	0.0578
DU97-flatback	Serrated Tape	12.8	59.3	3.20×10^6	1.83	-0.226	0.0502
DU97-flatback	No Trip	15.4	59.1	3.19×10^6	2.21	-0.243	0.0493
DU97-flatback	Serrated Tape	15.4	58.4	3.20×10^6	2.13	-0.233	–
DU97-flatback/splitter	No Trip	5.1	43.5	2.41×10^6	0.86	-0.155	–
DU97-flatback/splitter	Serrated Tape	5.2	43.3	2.40×10^6	0.71	-0.122	–
DU97-flatback/splitter	No Trip	12.8	43.9	2.39×10^6	1.84	-0.204	–
DU97-flatback/splitter	Serrated Tape	12.8	43.5	2.41×10^6	1.83	-0.202	–
DU97-flatback/splitter	No Trip	5.1	58.6	3.21×10^6	0.82	-0.155	0.0345
DU97-flatback/splitter	Serrated Tape	5.2	58.3	3.20×10^6	0.82	-0.154	–
DU97-flatback/splitter	No Trip	12.8	58.4	3.20×10^6	1.81	-0.207	0.0320
DU97-flatback/splitter	Serrated Tape	12.8	48.9	3.21×10^6	1.80	-0.205	–

Table 3. Test matrix for aerodynamic measurements obtained for $U_\infty > 30 m/s$, with *uncorrected* force and moment coefficients.

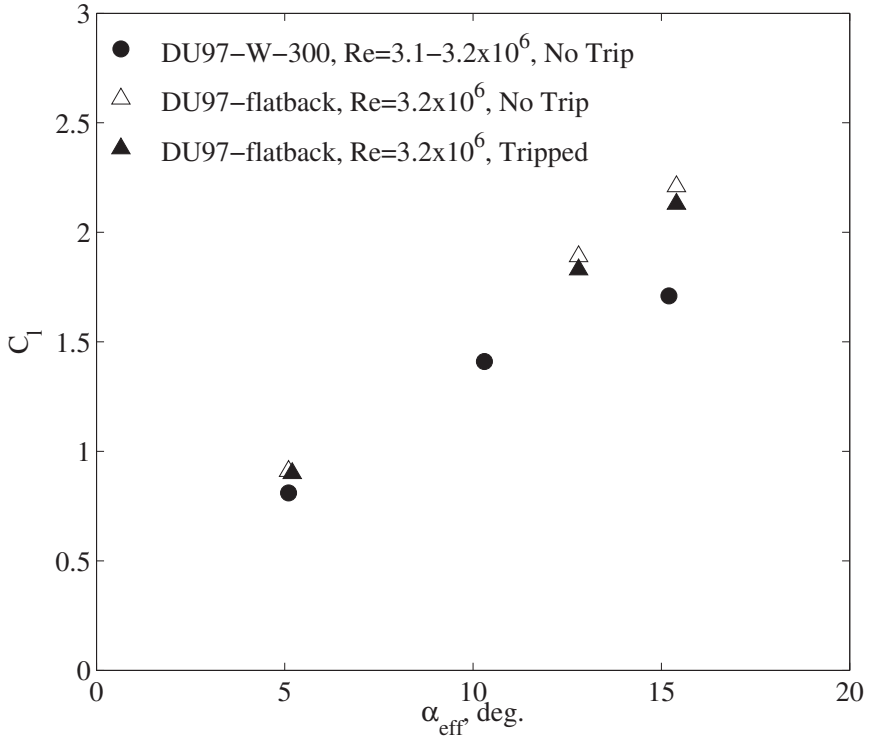

Figure 30. Uncorrected lift coefficients for the DU97-W-300 and DU97-flatback for $55 \leq U_\infty \leq 60$m/s.

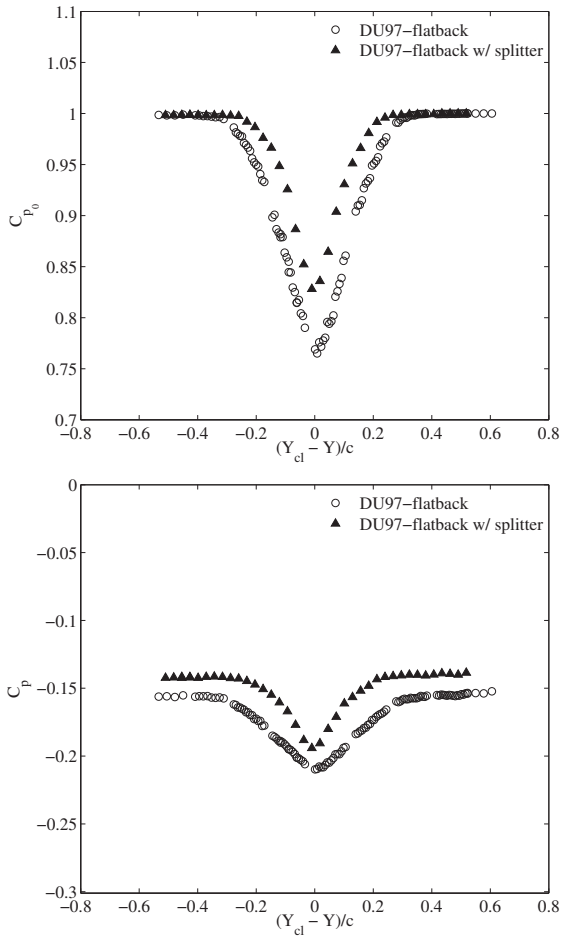

Figure 31. DU97-flatback stagnation and static pressure profiles measured at $X/c = 3.74$. $Re_c = 3.2 \times 10^6$, $\alpha_{geom} = 5.1$ deg, no trip.

are plotted in terms of the static pressure coefficient (2) and the stagnation pressure coefficient

$$C_{p0} = \frac{p_0 - p_\infty}{p_{0_\infty} - p_\infty}, \tag{3}$$

where p_0 and p are the measured Pitot and static pressures, respectively.

We have used these data to estimate the total airfoil drag through a straightforward momentum balance. Consider the control volume shown in Figure 33. The difference of the mass flowing into the volume on the left and flowing out on the right, per unit span, is $\int (\rho U_\infty - \rho U)\ \mathrm{d}Y$. This is the mass flow out per unit span of the sides of the volume, which we assume occurs with an average X component of velocity of $\frac{1}{2}(U_\infty + U_e)$, where U_e is the flow velocity outside of the wake on the right hand face of the volume. With this, the net X-momentum flux out of the volume per unit span is $\rho \int \left[U^2 - U_\infty^2\right] \mathrm{d}Y + \frac{1}{2}\rho(U_\infty + U_e) \int \left[U_\infty - U\right]\ \mathrm{d}Y$, and the X-component of the pressure force on the volume per unit span is $\int (p_\infty - p)\, \mathrm{d}Y$, where $p(Y)$ is the pressure on the right-hand face. The

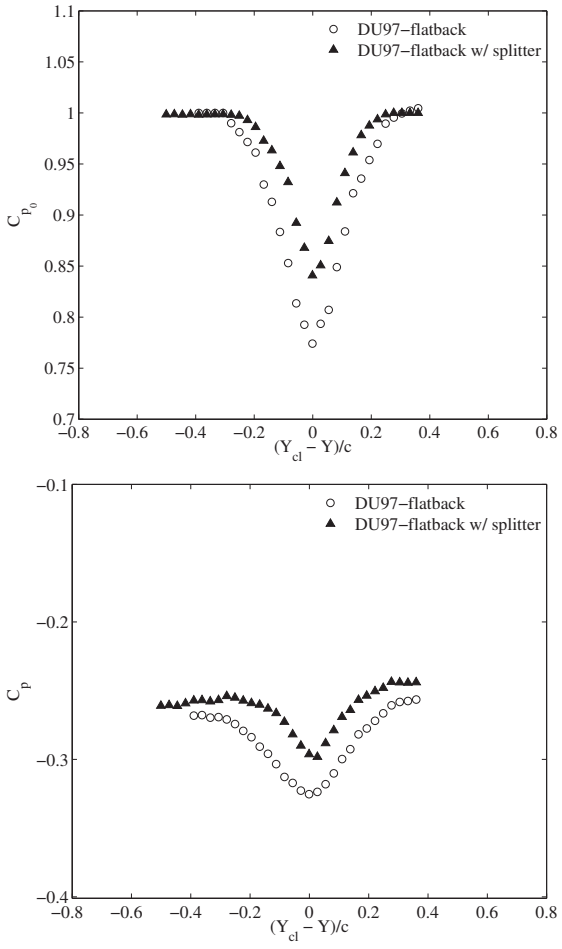

Figure 32. DU97-flatback stagnation and static pressure profiles measured at $X/c = 3.74$. $Re_c = 3.2 \times 10^6$, $\alpha_{geom} = 12.8$ deg, no trip.

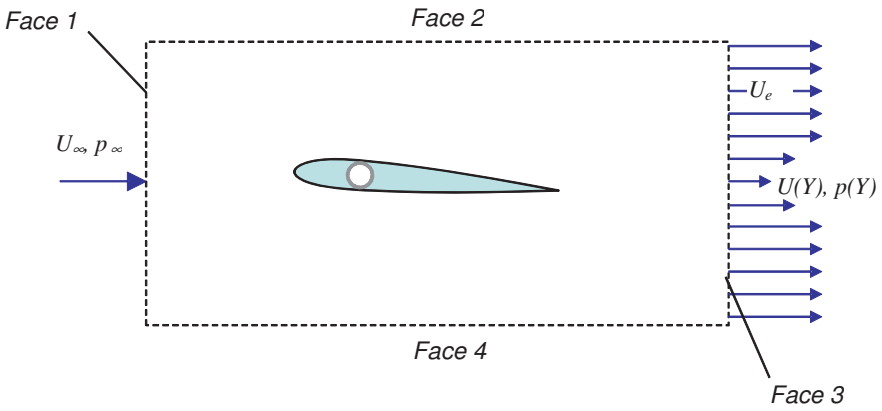

Figure 33. Control volume used for drag analysis based on wake profiles.

total drag force per unit span on the airfoil located in the volume is thus

$$D = \rho \int \left[U_\infty^2 - U^2 - \frac{1}{2}(U_\infty + U_e)(U_\infty - U) - \frac{p - p_\infty}{\rho} \right] \mathrm{d}Y, \tag{4}$$

and the drag coefficient is

$$C_d = \int \left[2 - 2\frac{U^2}{U_\infty^2} - \left(1 + \frac{U_e}{U_\infty}\right)\left(1 - \frac{U}{U_\infty}\right) - C_p \right] \mathrm{d}(Y/c). \tag{5}$$

In terms of the stagnation and static pressure coefficients measured on the downstream face C_{p_0} and C_p, this becomes

$$C_d = \int \left[2 - 2C_{p_0} + C_p - \left(1 + \sqrt{1 - C_p}\right)\left(1 - \sqrt{C_{p_0} - C_p}\right) \right] \mathrm{d}(Y/C). \tag{6}$$

Since the integrand is zero outside the viscous wake, the limits of the integral can be taken as the edges of the wake. Some attempt was also made to infer drag coefficients by integrating the airfoil pressure distributions. However, these estimates were found to be too uncertain to be useful, the uncertainty deriving from the large lift coefficient and the unknown details (including pressure) of the blunt trailing edge and splitter-plate flows.

The calculated drag coefficients are compared in Figure 34. The single corrected drag coefficient value available from the present measurements at $Re_c = 1.6 \times 10^6$ is slightly higher than the $Re_c = 3$ million data from TU-Delft, as would be expected. The flatback drag is significantly higher than that of the DU97-W-300, which is also expected due to the additional base drag induced by the relatively low pressure on the base of the flatback. Rather unexpectedly, the flatback drag values decrease somewhat with increase in angle of attack, presumably as a result of viscous flow details in the base region. Adding the splitter plate does significantly attenuate the wake of the blunt trailing edge and the associated drag. The drag coefficient comparison of Figure 35 shows that the splitter plate eliminates roughly half of the additional drag associated with the flatback trailing edge.

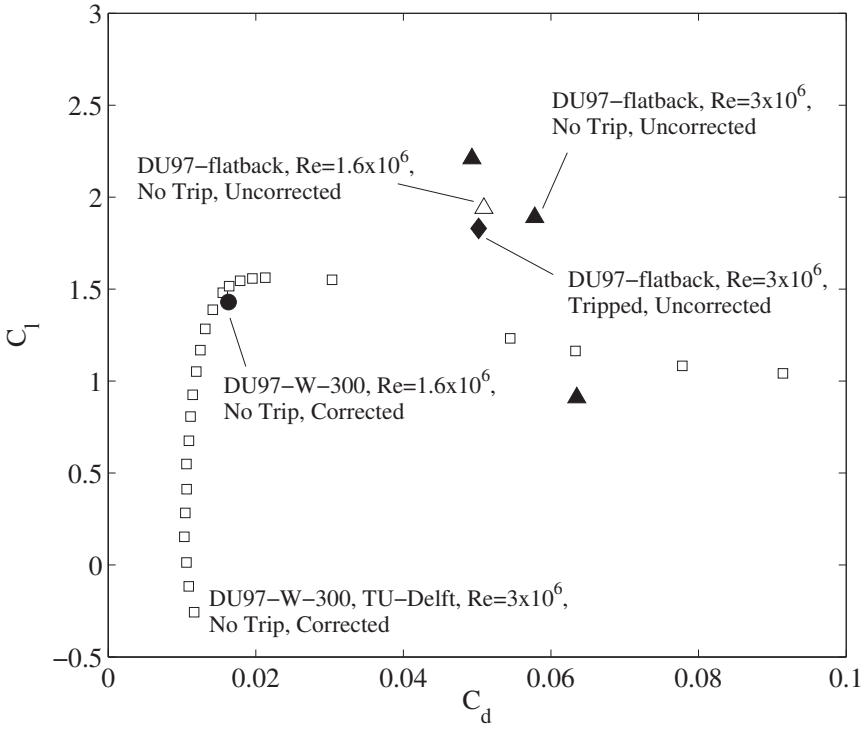

Figure 34. Drag coefficients for the DU97-W-300 and DU97-flatback, compared with data taken in the TU-Delft wind tunnel.

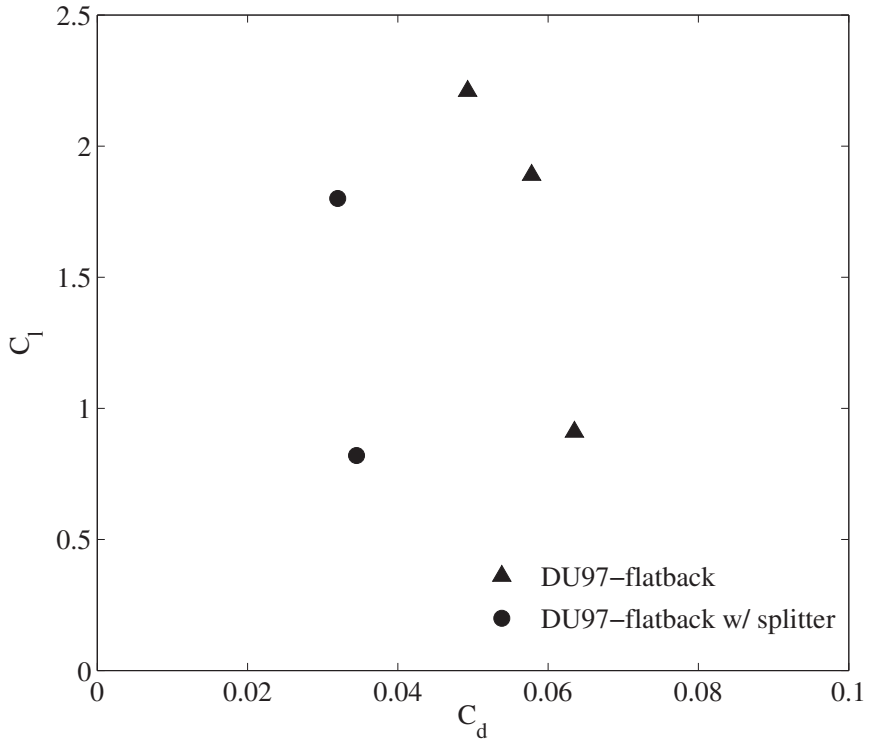

Figure 35. Uncorrected drag coefficients for the DU97-flatback with and without splitter plate, $Re_c = 3.2 \times 10^6$, no trip.

Trip	α_{geom}, deg.	Re_c	$x - x_{te}$	Side	δ (mm)	δ^* (mm)	θ (mm)
No Trip	5.1	3.01×10^6	0.9	Pressure	16.9	1.6	1.3
No Trip	5.1	3.14×10^6	1.3	Suction	22.8	8.1	3.6
No Trip	10.3	1.51×10^6	1.3	Suction	41.9	21.9	5.5
No Trip	10.3	3.08×10^6	1.0	Pressure	18.7	1.4	1.2
No Trip	10.3	3.10×10^6	1.3	Suction	36.3	17.0	4.9
Serrated Tape	10.3	1.53×10^6	0.9	Pressure	16.3	17.0	4.9
Serrated Tape	10.3	3.15×10^6	1.0	Pressure	18.3	1.2	1.0
Serrated Tape	10.3	3.05×10^6	1.3	Suction	99.9	42.7	8.7
No Trip	15.4	3.07×10^6	1.3	Suction		Flow separated	

Table 4. Test matrix and results for the hotwire measurements on the DU97-W-300 airfoil.

4.4 Trailing Edge Boundary Layer Properties

As discussed in Section 2.4, a single hot-wire probe was used to measure trailing edge boundary layers for both sides of the DU97-W-300 airfoil. Conditions and locations for the measurements, along with boundary layer parameters, are listed in Table 4. The measurements were made between 0.9 and 1.3mm aft of the trailing edge of the airfoil to reduce the risk of probe damage. We assume that there was no significant evolution of the boundary layer flow over this short distance. While we were not successful in making measurements on the DU97-W-300 to confirm this assumption, measurements upstream and downstream of the trailing edge were made as part of a different, but parallel, test of a similar 0.91-m chord DU96 airfoil model. These measurements show little effect on the boundary layer flow over this short distance as it passes the trailing edge, at least over the region that can be reached with the hot wire probe.

In processing these data, it was found that the boundary layer edge location (needed to define boundary layer thickness δ and edge velocity U_e) could not be reliably inferred from the mean velocity profile alone. The reason is that the flow velocity is not constant outside the boundary layer near the trailing edge because of the local flow curvature. This gradient tends to obscure the boundary layer edge. Instead, the edge was defined as the location where the interpolated turbulence intensity u/U_e passes through 2%. The boundary layer thickness was measured to this point, and the edge velocity determined from the interpolated mean velocity here. (Note that the use of the edge velocity is recursive, and so a few iterations are needed to converge to the true edge location.) In a flat plate boundary layer, the location of the boundary layer edge determined in this way, and using the more conventional definition (point where the velocity is 99% of the uniform free stream), produce very similar answers. The displacement thickness, δ^*, and momentum thickness, θ, are given in Table 4 and were integrated using the usual definitions:

$$\delta^* = \int_0^{\delta} \left(1 - \frac{U}{U_e}\right) \, \mathrm{d}|y - y_0| \tag{7}$$

and

$$\theta = \int_0^{\delta} \frac{U}{U_e}\left(1 - \frac{U}{U_e}\right)\, \mathrm{d}|y - y_0|. \tag{8}$$

5 Acoustic Results

The test matrix for the microphone phased array measurements is shown in Table 5. This matrix describes the entire set of test configurations measured, the tunnel flow speed (*not* corrected for blockage), the geometric angle of attack (AoA), and the tunnel condition, *i.e.* fan speed (rpm) and tunnel temperature. Note that the last three configurations in this table correspond to the empty tunnel case, where no airfoil is installed.

The data from the 63 microphones in the array was processed to compute the following results:

- Average noise spectrum: the average of all 63 microphones in the array was computed. It provides an estimate of the noise inside the anechoic chamber. This estimate is useful to obtain noise results at low frequency, in particular below 500 Hz where the array resolution is very poor. The average spectrum was computed in narrow band (3.125 Hz resolution) and in 1/12th octave bands. The definition of the 1/12th octave bands used here is described in Appendix B.

- Acoustic maps: the acoustic maps were computed over a plane along the center of the test section as illustrated in Figure 36(a). The acoustic maps were computed for the 1/12th octave bands in the 500 to 5000 Hz range. The beamforming grid has 201 points along the test section direction (grid resolution of 2.54 cm) and 73 points from floor to ceiling (grid resolution of 2.54 cm) for a total of 14,600 grid points. The color contours in the acoustic maps range from the maximum level in the map to the maximum level minus 10 dB as illustrated in Figure 36(b). The level (color) in the acoustic maps represents the noise observed at the array plane due to sources at the grid points.

- Integrated Spectrum: Using the point spread function, the levels in the scanning grid encompassing the trailing edge were summed to a single value for each frequency to compute the integrated spectrum. In this work, the levels were integrated 5 dB down from the peak value to avoid adding the effects of the sidelobes from other sources. The integrated spectrum was computed for all the configurations listed in Table 5 in 1/12th octave bands in the 500 to 5000 Hz range. To compute the integrated spectrum, a volume enclosing the trailing edge of the airfoil was defined for the beamforming/integration process. The volume for the integration is shown in Figure 37. The volume has a square cross section and it is aligned with the airfoil trailing edge (green box in Figure 37). The parts of the trailing edge next to the junction with the tunnel were excluded to avoid noise due to end effects as well as other spurious noise sources seen on the test section floor and ceiling.

Airfoil	α_{geom}, deg.	Trip	U_∞ (m/s)[1]	Fan Speed (rpm)	Tunnel Temp. (deg. F)	St	Run Number
DU97-W-300	5.1	No trip	28.25	267	58.9	–	008
DU97-W-300	5.1	No trip	42.06	402	59.9	–	009
DU97-W-300	5.1	No trip	55.99	534	62.9	–	010
DU97-W-300	10.3	No trip	28.43	288	60.7	–	005
DU97-W-300	10.3	No trip	42.04	436	61.8	–	006
DU97-W-300	10.3	No trip	56.25	586	65.4	–	007
DU97-W-300	15.4	No trip	28.76	304	71.5	–	012
DU97-W-300	15.4	No trip	55.61	599	67	–	011
DU97-W-300	10.3	Tripped	28.31	272	64.9	–	002
DU97-W-300	10.3	Tripped	42.35	425	65.7	–	003
DU97-W-300	10.3	Tripped	56.37	573	68.2	–	004
DU97-flatback	5.1	No trip	28.82	278	73.4	0.25	018
DU97-flatback	5.1	No trip	43.17	422	73.8	0.24	019
DU97-flatback	5.1	No trip	57.50	561	75.4	0.24	020
DU97-flatback	12.8	No trip	43.35	476	75.6	0.24	022
DU97-flatback	12.8	No trip	56.83	622	77.9	0.23	023
DU97-flatback	15.4	No trip	28.41	306	70.2	0.25	037
DU97-flatback	15.4	No trip	56.55	625	72.7	0.24	038
DU97-flatback	12.8	Tripped	28.47	301	72.4	0.25	034
DU97-flatback	12.8	Tripped	43.10	453	72.7	0.24	035
DU97-flatback	12.8	Tripped	56.65	605	75.1	0.24	036
DU97-flatback Splitter Plate	5.1	No trip	28.55	276	75.4	0.29	027
DU97-flatback Splitter Plate	5.1	No trip	43.21	415	75.6	0.30	028
DU97-flatback Splitter Plate	5.1	No trip	57.16	553	77.0	0.30	029
DU97-flatback Splitter Plate	12.8	No trip	28.57	305	76.2	0.28	024
DU97-flatback Splitter Plate	12.8	No trip	43.26	468	76.3	0.29	025
DU97-flatback Splitter Plate	12.8	No trip	57.28	625	78.8	0.29	026
DU97-flatback Splitter Plate	5.1	Tripped	57.43	544	74.6	0.26	030
DU97-flatback Splitter Plate	12.8	Tripped	28.48	298	72.9	0.27	031
DU97-flatback Splitter Plate	12.8	Tripped	43.11	455	72.7	0.27	032
DU97-flatback Splitter Plate	12.8	Tripped	56.71	604	75.8	0.27	033
Empty tunnel			28.18	233	64.7	–	112
Empty tunnel			42.25	343	65.3	–	113
Empty tunnel			54.00	432	67.7	–	114

Table 5. Test matrix for the phased array measurements.

[1]Flow speeds of 56, 44, and 28 m/s correspond to nominal chord Reynolds numbers of 1.6, 2.4, and 3.2 million, respectively.

5.1 Empty Tunnel Results

The average noise spectra of the empty tunnel at 28.18, 42.25, and 54.00 m/s are shown in Figure 38 (runs 112, 113, and 114). The empty tunnel spectrum is essentially broadband but a number of tones are clearly observed, in particular below 900 Hz. The fan blade passage frequency (BPF) and the first harmonic are identified in the spectra. The other tones are not related to the fan. Another feature of the spectrum is the valley around 80 Hz which is the result of the destructive interference effect of the direct sound and the reflection from the back wall of the anechoic chamber. Note that the anechoic chamber acoustic treatment is very ineffective at these low frequencies; the cut-off frequency of the chamber is approximately 200 Hz.

The empty tunnel spectra were then scaled by the 6th and 5th power of the flow speed and shown in Figures 39(a) and 39(b), respectively. The noise spectra scaled very well with the 6th power in the 100 to 2500 Hz range while the 5th power fits the data above 2500 Hz. Scaling with respect to the fan speed leads to the same results, *i.e.* fan and flow speed for the empty tunnel are linear. It is important to note that the empty tunnel noise spectra are not a true indication of the background noise with the model installed. Since the models produce blockage, the tunnel fan needs to operate at a faster speed and consequently the background noise will be louder than that measured with the empty tunnel. For example, the fan speed operates at 432 rpm to achieve a 54.0 m/s flow speed in the empty test section (run 114) while it must run at 625 rpm when the DU97-flatback is installed at a geometric AoA of 15.4 degrees for a flow speed of 56.55 m/s (run 038). Thus, care must be exercised when analyzing the results for the average spectra. The empty tunnel scaling information here is useful to estimate the actual background noise spectrum when a model is installed in the test section. To illustrate this point, Figure 40 shows the average narrowband spectrum for the empty tunnel at 54.0 m/s (run 114) and for the DU97-flatback model (15.4 degrees geometric AoA) at 56.5 m/s. The actual background noise for this case is most likely the red curve shifted up by $\sim$ 10.8 dB (at least below 2000 Hz). This ”corrected” background noise implies that the part of the spectrum around 150 Hz, containing the hay-stack due to the vortex shedding at the blunt end of the airfoil, is the only part of the spectrum that shows an acceptable signal-to-noise ratio.

5.2 Airfoil Results

In this section, the acoustic results for the DU97-W-300 and DU97-flatback airfoils are presented. The data in this section includes narrowband and 1/12th octave band spectra for all the airfoil configurations shown in Table 5. Acoustic maps are also shown for selected configurations.

Narrowband Spectrum

Figures 41 through 43 show the average narrowband spectrum for the DU97-W-300 airfoil for 5.1 degrees, 10.3 degrees (no trip and tripped), and 15.4 degrees geometric AoAs at the flow speeds of 57, 44, and 28 m/s, respectively. As reference, the empty tunnel case corresponding to the same

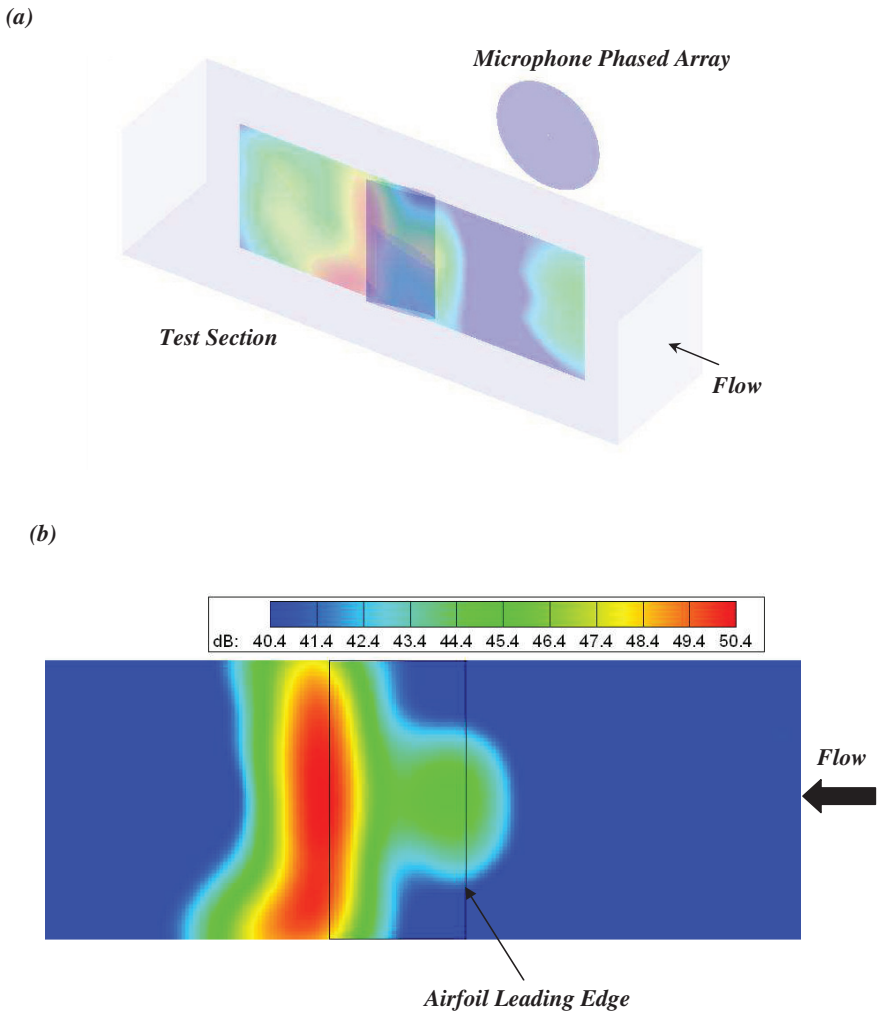

Figure 36. (a) Beamforming measurement plane for the computation of the acoustic maps. (b) Typical acoustic map and color scale for an airfoil measurement. (Example shown: DU97-flatback, 5.1 degrees α_{geom}, 28m/s flow speed, and 1933 Hz 1/12th band).

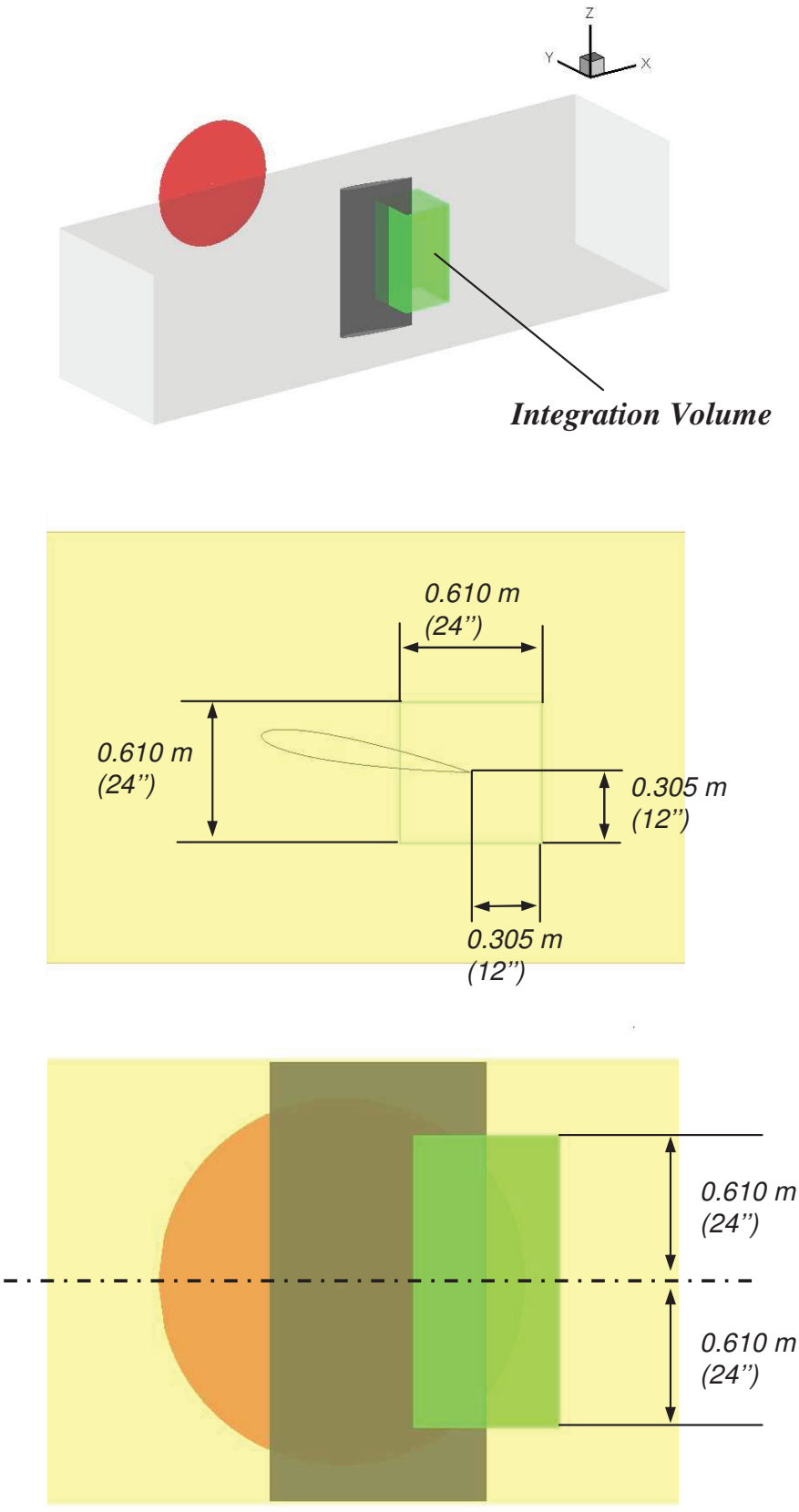

Figure 37. Beamforming measurement volume for the computation of the integrated spectrum.

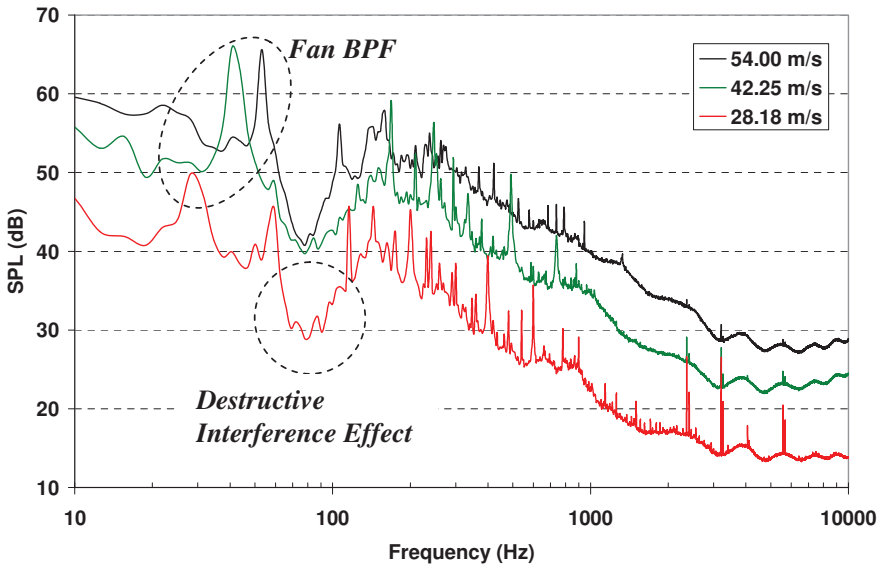

Figure 38. Average noise spectrum for the empty tunnel operating at several flow speeds. (Frequency resolution: 3.125 Hz)

test section flow speed is also plotted in these figures. Based on the discussion of the empty tunnel noise in section 5.1, the average noise spectrum can not provide any useful information for the DU97-W-300 airfoil. In other words, the signal-to-noise ratio is poor.

Figures 44 through 46 show the same results for the DU97-flatback airfoil without the splitter plate. For this airfoil, the geometric AoAs are 5.1 degrees, 12.8 degrees (no trip and tripped), and 15.4 degrees at the same flow speeds. The results now show a dominant hay-stack peak due to vortex shedding, e.g. at 150 Hz for the case of 5.1 degrees AoA at 57 m/s. In some configurations, the harmonics of the fundamental shedding frequency are also observed such as for the 5.1 degrees AoA at 57 m/s (Figure 44(a)) and all cases for 28 m/s (Figures 46(a), (c), and (d)). Therefore, it is reasonable to assume that the spectrum below approximately 200 Hz is a good estimate of the noise generated by the DU97-flatback airfoil. However, the actual noise levels must be corrected due to the chamber's reflection and microphone frequency response function below 200 Hz as explained in Section 2.

Comparing the cases with and without trip for 57 and 44 m/s (Figures 44(b), 44(d), ,45(b) and 45(d)) the effects of the boundary layer trip on vortex shedding noise are to narrow the width of the spectral peak and slightly increase its amplitude.

The results for the same airfoil with the splitter plate installed are shown in Figures 47 through 49 at the flow speeds of 57, 44, and 28 m/s, respectively. To help in the interpretation of the splitter plate noise impact, the noise spectrum of the DU97-flatback airfoil is also plotted in these figures. For the higher flow speeds of 44 and 57 m/s, the splitter plate yields a dramatic reduction in the vortex shedding amplitude ranging from 10 to 15 dB. Evidence of the reduction of the harmonics is also seen in Figures 47(a) and 48(a). The results also suggest that with the splitter plate installed there are two distinct vortex shedding frequencies as observed in some configurations such as the

(a)

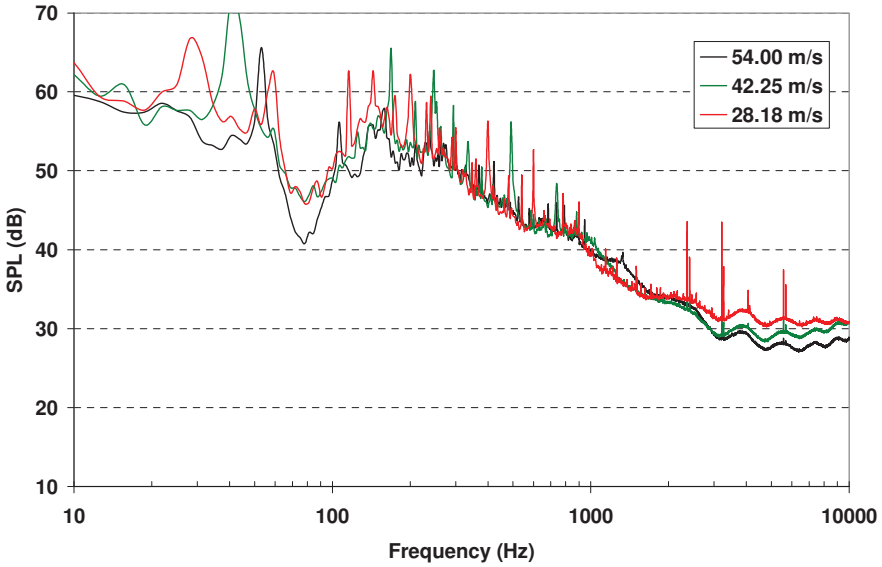

(b)

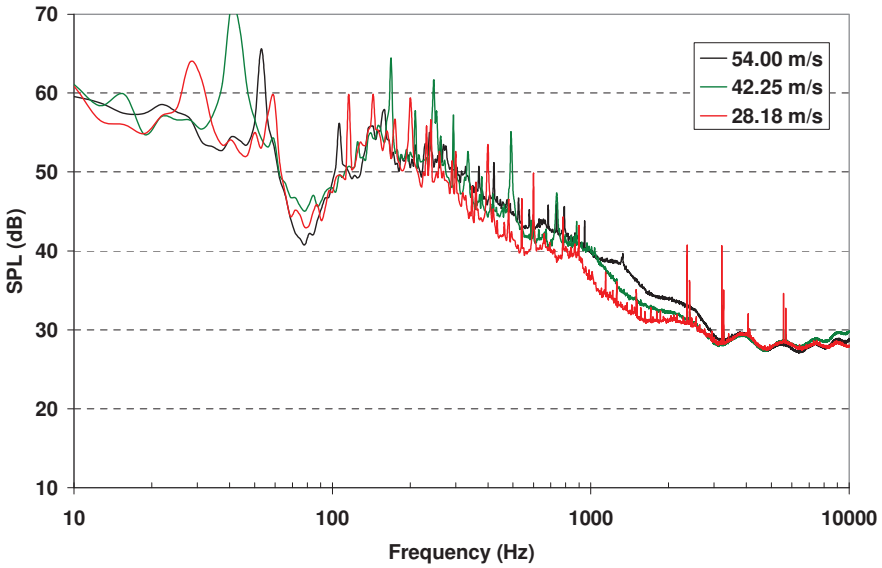

Figure 39. Average noise spectrum the empty tunnel operating at several flow speeds scaled to the (a) 6th and (b) 5th power of the flow velocity. (Frequency resolution: 3.125 Hz)

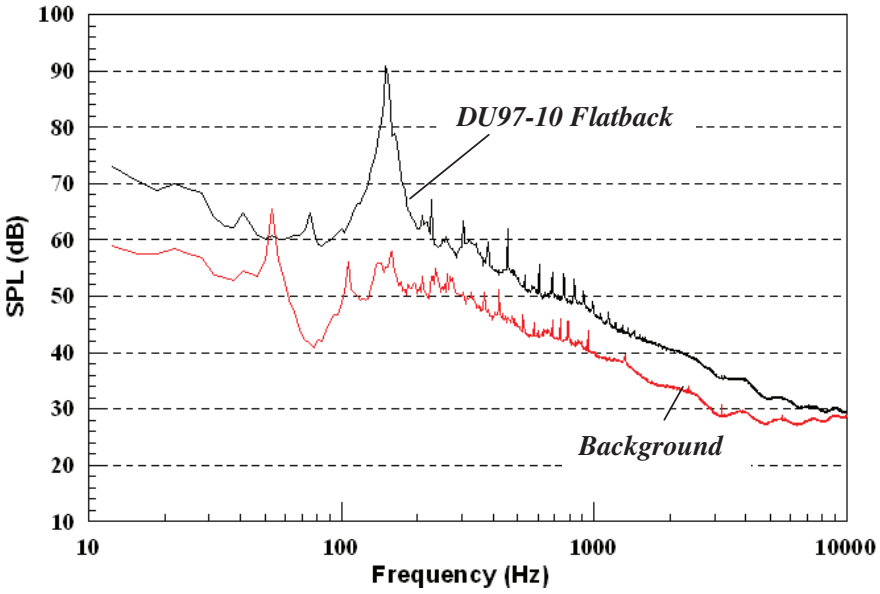

Figure 40. Average noise spectrum for the empty tunnel and the DU97-flatback airfoil ($\alpha_{geom} = 15.4$ degrees) at 56.5m/s.

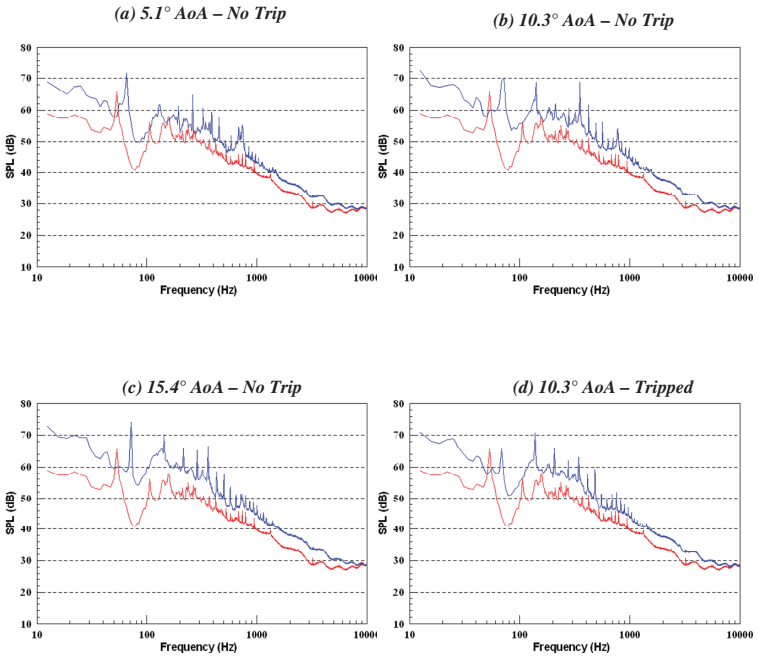

Figure 41. Average narrowband noise spectrum for the DU97-W-300 airfoil at $\sim$ 57 m/s (runs 10, 7, 11, 4, and 114).

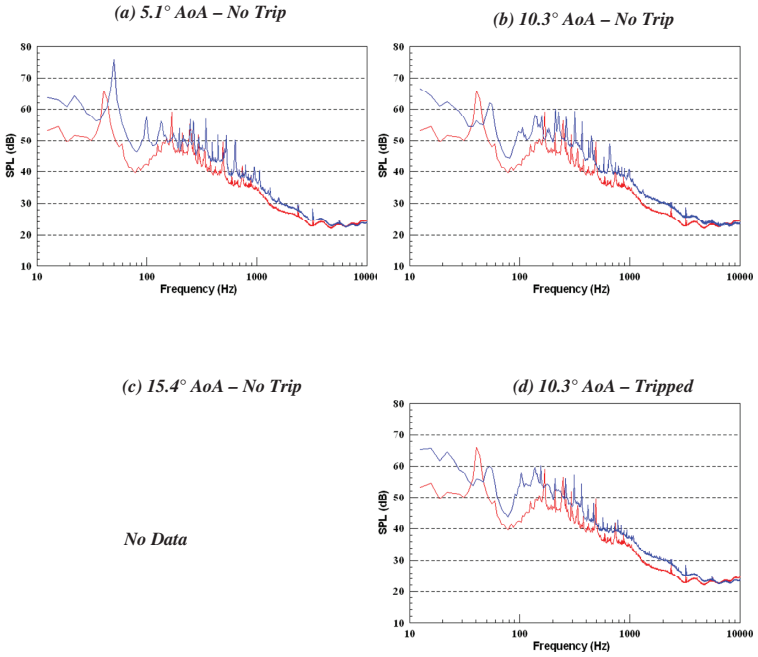

Figure 42. Average narrowband noise spectrum for the DU97-W-300 airfoil at $\sim$ 44 m/s (runs 9, 6, 3, and 113).

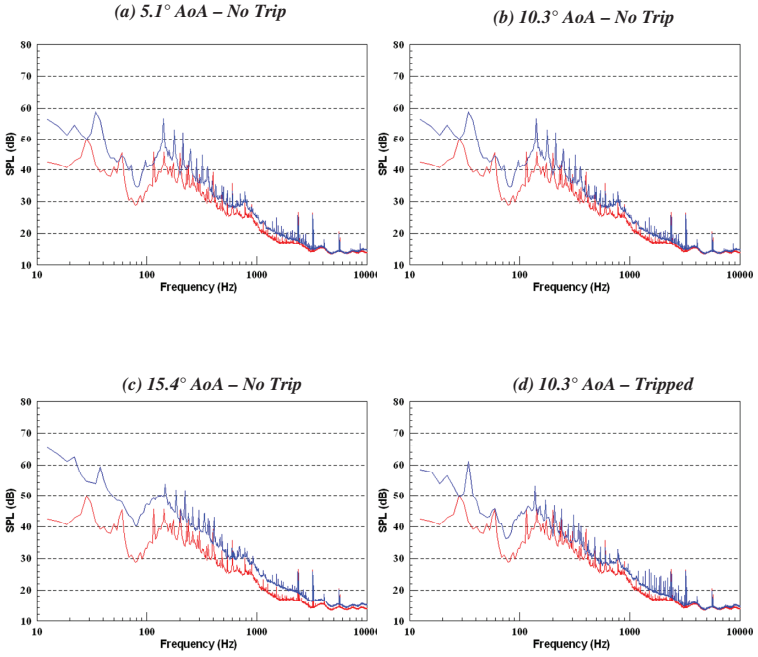

Figure 43. Average narrowband noise spectrum for the DU97-W-300 airfoil at $\sim$ 28 m/s (runs 8, 5, 12, 2, and 112).

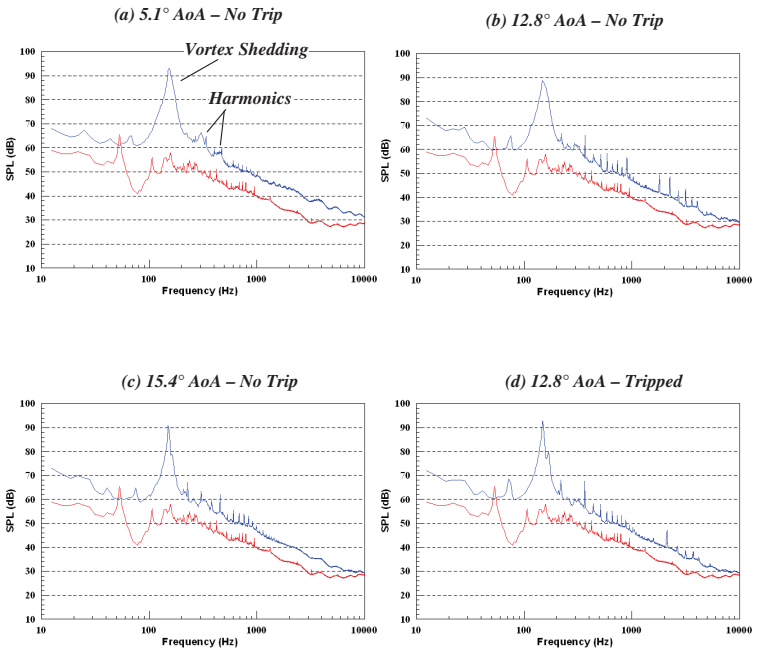

Figure 44. Average narrowband noise spectrum for the DU97-flatback airfoil at $\sim$ 57 m/s (runs 20, 23, 38, 36, and 114).

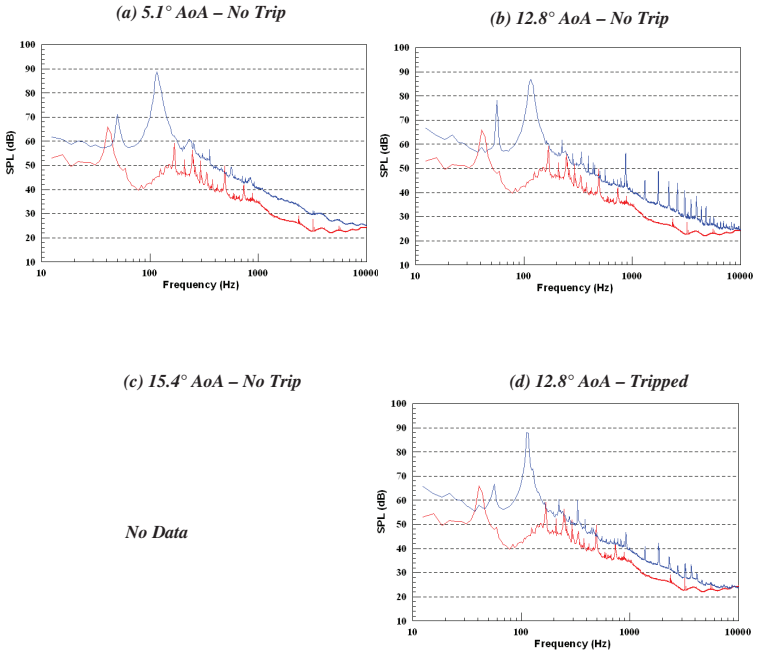

Figure 45. Average narrowband noise spectrum for the DU97-flatback airfoil at $\sim$ 44 m/s (runs 19, 22, 35, and 113).

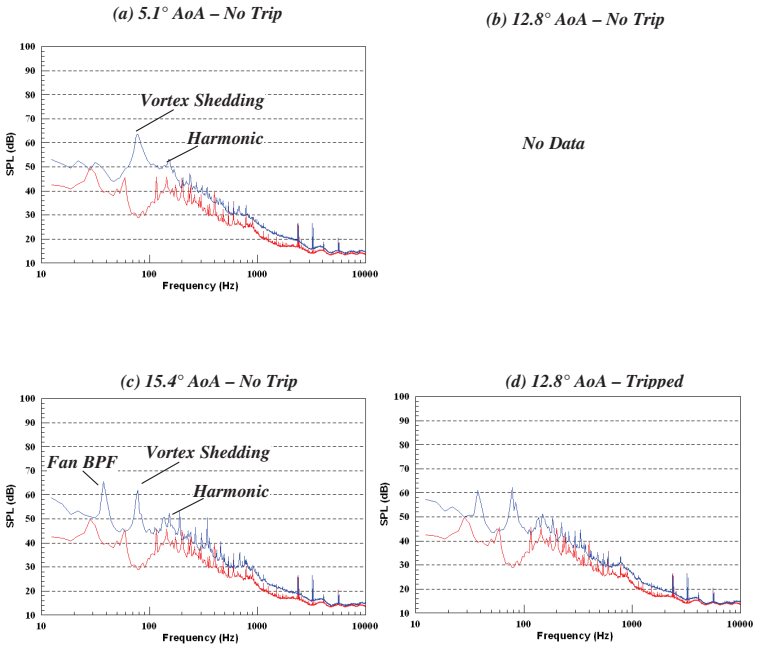

Figure 46. Average narrowband noise spectrum for the DU97-flatback airfoil at $\sim$ 28 m/s (runs 18, 34, 37, and 112).

5.1 degrees AoA at 44 m/s (Figure 48(a)).

There are two configurations for the lowest flow speed of 28 m/s to assess the splitter plate effect: 5.1 degrees AoA no trip and 12.8 degrees AoA tripped. From these two cases, the splitter plate appears to have a lesser noise impact as compared to the other flow speeds. The 5.1 degrees AoA no trip case in Figure 49(a) suggests a shift in the fundamental frequency of the vortex shedding from 78.1 to 90.6 Hz with no reduction in the amplitude. However, this is the frequency range where there is destructive interference effect due to the chamber wall reflections. Since the destructive interference is stronger at the lower frequency (78.1 Hz), it is very likely that there is some reduction of the peak amplitude. It is also interesting to note that there is a noticeable reduction (1-4 dB) in the rest of the spectrum with the splitter plate. Finally, the 12.8 degrees AoA tripped configuration shows about a 5 dB reduction in peak amplitude with the splitter plate but no significant difference over the rest of the spectrum.

Table 5 gives the Strouhal number of the peak vortex-shedding frequency identified from the averaged acoustic spectra. The Strouhal number is defined as

$$St = \frac{f_{peak} h}{U_\infty} \tag{9}$$

where h is the flatback base height. Note that the Strouhal number is calculated using the uncorrected free stream velocity, which does not account for test section blockage. The Strouhal number of the flatback vortex-shedding noise is 0.24-0.25, and is insensitive to Reynolds number, angle of attack, and boundary layer tripping for the conditions investigated. The Strouhal number for the flatback with splitter plate is increased to 0.26-0.30, and remains insensitive to angle of at-

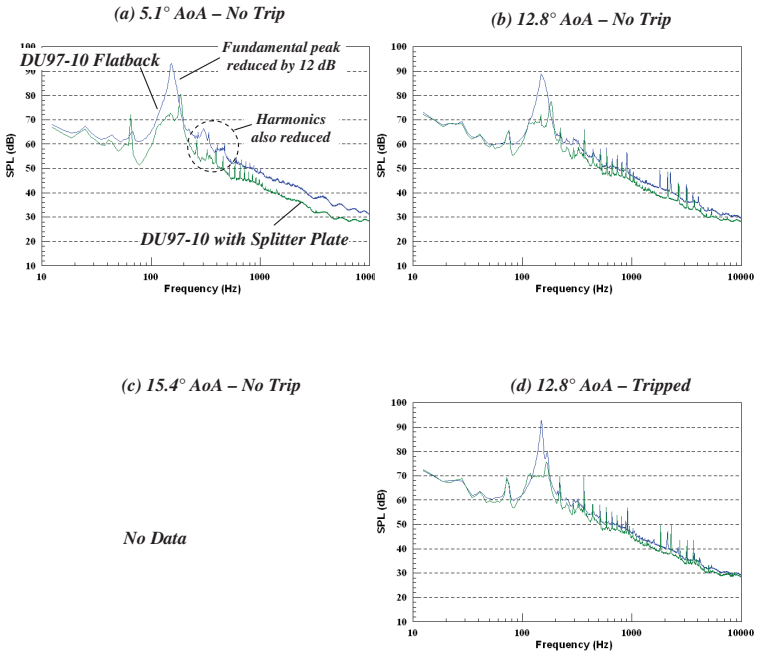

Figure 47. Average narrowband noise spectrum for the DU97-flatback and DU97-flatback with splitter plate at $\sim$ 58 m/s (runs 29 vs 20, 26 vs 23, and 33 vs 36).

tack although some mild dependence on Reynolds number and boundary layer tripping is evident. The Reynolds number dependence must be interpreted with caution since the dependence of the blockage effect on Reynolds number is unknown.

Acoustic Maps

The noise maps for all configurations were computed in 1/12th octave band in the 500 to 5000 Hz range. For the sake of illustration, the 38 maps for the DU97-flatback airfoil at 5.1 degrees AoA at 58 m/s are shown in Figures 50 through 53. In these plots, the flow is from right to left and each plot has its own scale. The airfoil is indicated by the rectangle. The 1/12th octave center frequency is shown on the top left corner of the map. This case was selected because it clearly shows trailing edge noise in all frequency bands. The complete set of maps was visually inspected to identify configurations showing the presence of trailing edge noise. The result of this visual inspection will be presented in the next section together with the integrated spectra.

Average and Integrated Spectra in 1/12th Octave Bands

The objective in this section is to present the trailing edge noise spectrum. To this end, Figures 54(a) and 54(b) are used to illustrate the approach to compute this spectrum. The trailing edge

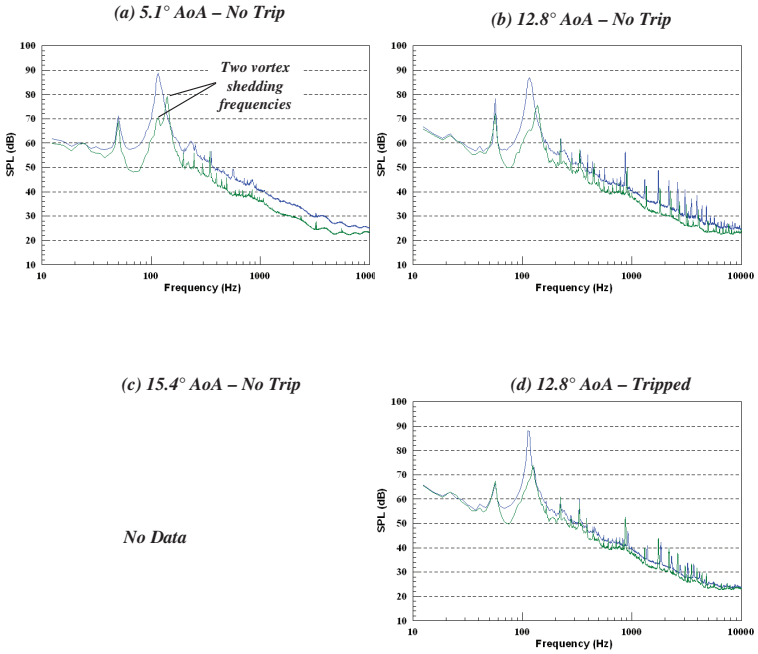

Figure 48. Average narrowband noise spectrum for the DU97-flatback and DU97-flatback with splitter plate at $\sim$ 44 m/s (runs 28 vs 19, 25 vs 22, and 32 vs 35).

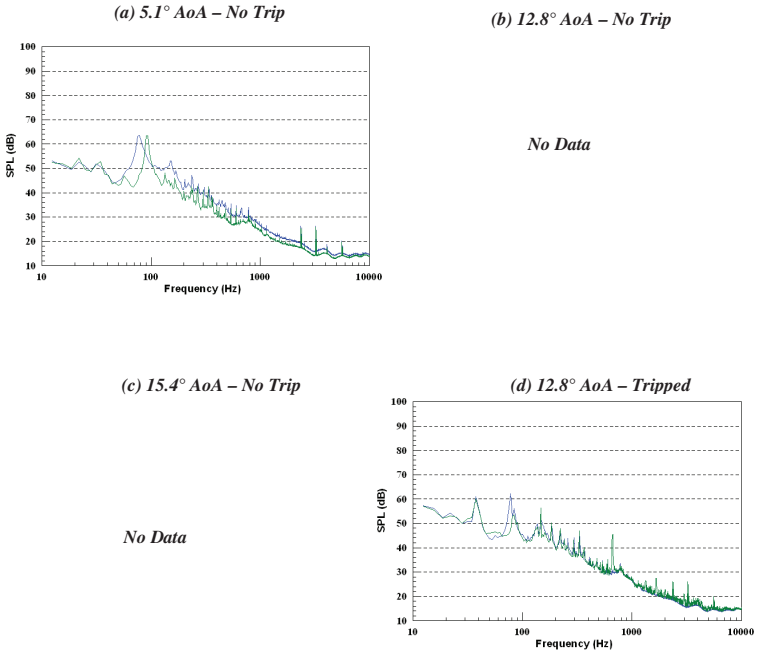

Figure 49. Average narrowband noise spectrum for the DU97-flatback and DU97-flatback with splitter plate at $\sim$ 28 m/s (runs 27 vs 18 and 31 vs 34).

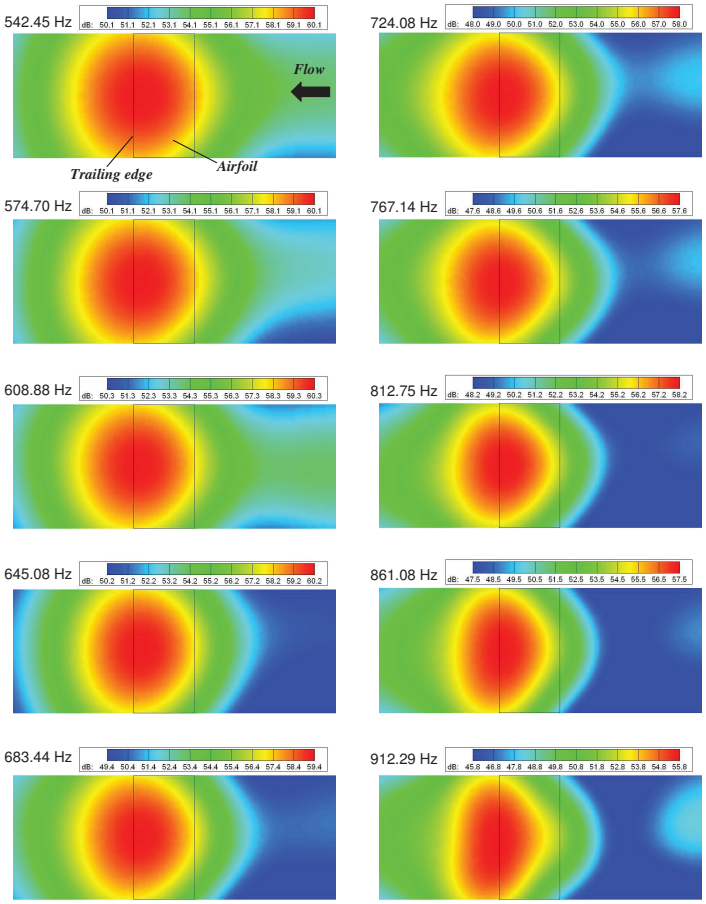

Figure 50. Acoustic maps (1/12th octave bands) for the DU97-flatback airfoil at 5.1 degrees geometric AoA at 57.5 m/s flow speed (run 20).

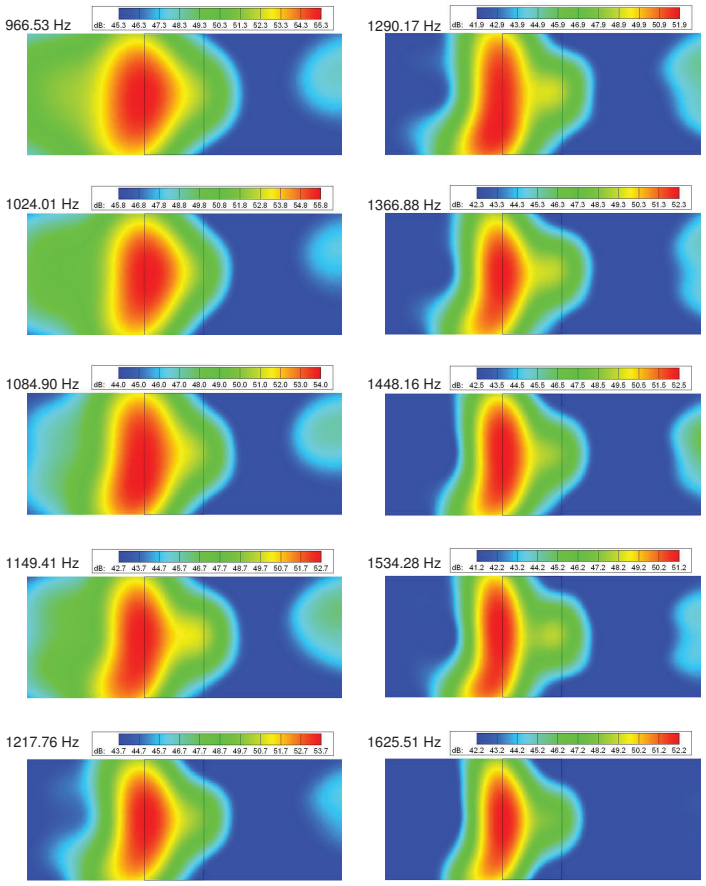

Figure 51. Acoustic maps (1/12th octave bands) for the DU97-flatback airfoil at 5.1 degrees geometric AoA at 57.5 m/s flow speed (run 20)

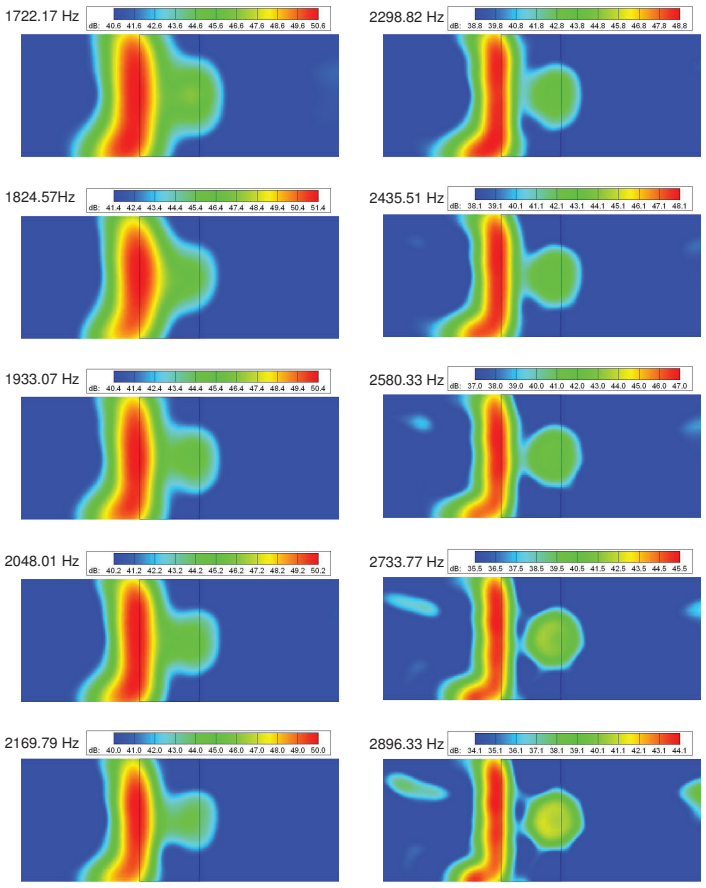

Figure 52. Acoustic maps (1/12th octave bands) for the DU97-flatback airfoil at 5.1 degrees geometric AoA at 57.5 m/s flow speed (run 20)

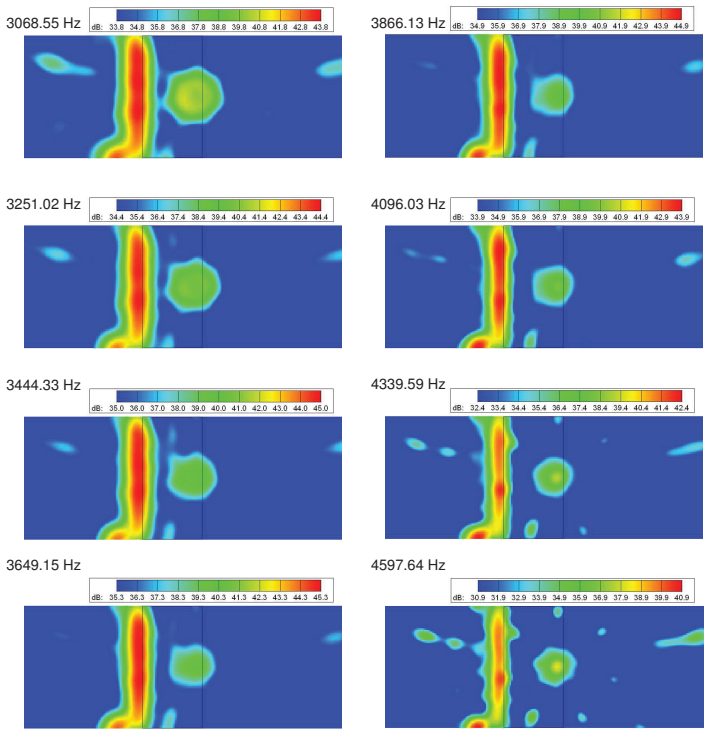

Figure 53. Acoustic maps (1/12th octave bands) for the DU97-flatback airfoil at 5.1 degrees geometric AoA at 57.5 m/s flow speed (run 20)

noise radiated from the airfoil is found by integrating the noise maps over a volume enclosing the trailing edge accounting for the array point spread function. The integration volume was defined earlier and shown in Figure 37. It included only the inner 1.22 m (4 feet) of the airfoil trailing edge. The integrated spectrum represents the average noise over the array produced by all sources inside the integration volume, *i.e.* all the other noise sources outside this volume are theoretically excluded. The integrated spectrum in Figure 54(a) is shown as a black line with diamond symbols at the center frequency of the bands in the 500 to 5000 Hz range. This integration is not performed below 500 Hz because of the reduced resolution of the array (see Figure 19(a)).

The integrated spectrum is contaminated from the ”sidelobes” of sources outside the volume of integration. Thus, the results from the integration must be carefully evaluated to enable correct interpretation. The approach taken here was to visually inspect the acoustic maps at each 1/12th band. If trailing edge noise was evident, the value of the spectrum is considered reliable and it is treated as genuine trailing edge noise. To illustrate this approach, selected acoustic maps are shown in the figure, *e.g.* see maps at the 2048 and 3650 Hz bands in Figure 54(a). On the other hand, if the presence of trailing edge noise in the maps was unclear, the integrated spectrum at that band was not considered trustworthy. Since the complete integrated spectrum is plotted in the figure, a red line at the bottom of the graph is used to indicate the frequency range where trailing edge noise is observed on the maps. If a red line is not shown in the graph, it implies that trailing edge noise could not be ”seen” on the maps and the actual trailing noise level is below the values plotted, *i.e.* the tunnel is too loud for the array to measure trailing edge noise.

In addition to showing the integrated spectrum, the average spectrum was also plotted on the same graphs, using the same information as in Figures 40 through 49 but in 1/12th bands rather than narrowband. The average spectrum is shown as a blue line with diamond symbols at the center frequencies. The lowest frequency plotted is 100 Hz because below this frequency reflections in the chamber are very significant. The main reason for plotting the integrated and average spectra together is that both are due to trailing edge noise. This fact is, in particular, true for the DU97-flatback airfoil both without and with the splitter plate. At frequencies below 500 Hz, the airfoils produce noise well above the tunnel background. This noise is due to vortex shedding at the trailing edge and clearly observed in the average spectrum. On the other hand, the integrated spectrum is also due to trailing edge noise (at least for the bands identified in the maps). Thus, these two spectra (average below 500 Hz and integrated above 500 Hz) are due to the same source, namely the airfoil trailing edge. Note that the average spectrum above 500 Hz is completely dominated by tunnel noise and thus not useful. For the sake of completeness, this part of the average spectrum is still shown in the graphs but should be ignored.

Figures 55 through 63 show the results for the configurations listed in Table 5 in the same form as described in Figure 54(a). In addition, selected configurations were further plotted as illustrated in Figure 54(b). To this end, note that the integrated spectrum represents the trailing edge noise from the center 2/3 of the airfoil while the average spectrum is due to the entire airfoil span. Thus, for consistency the integrated spectrum level should be increased by 1.7 dB to estimate the noise produced by the entire trailing edge. Combining the average spectrum (below 500 Hz) and the adjusted integrated spectrum (above 500 Hz) results in the single ”trailing edge noise” spectrum shown in Figure 54(b).

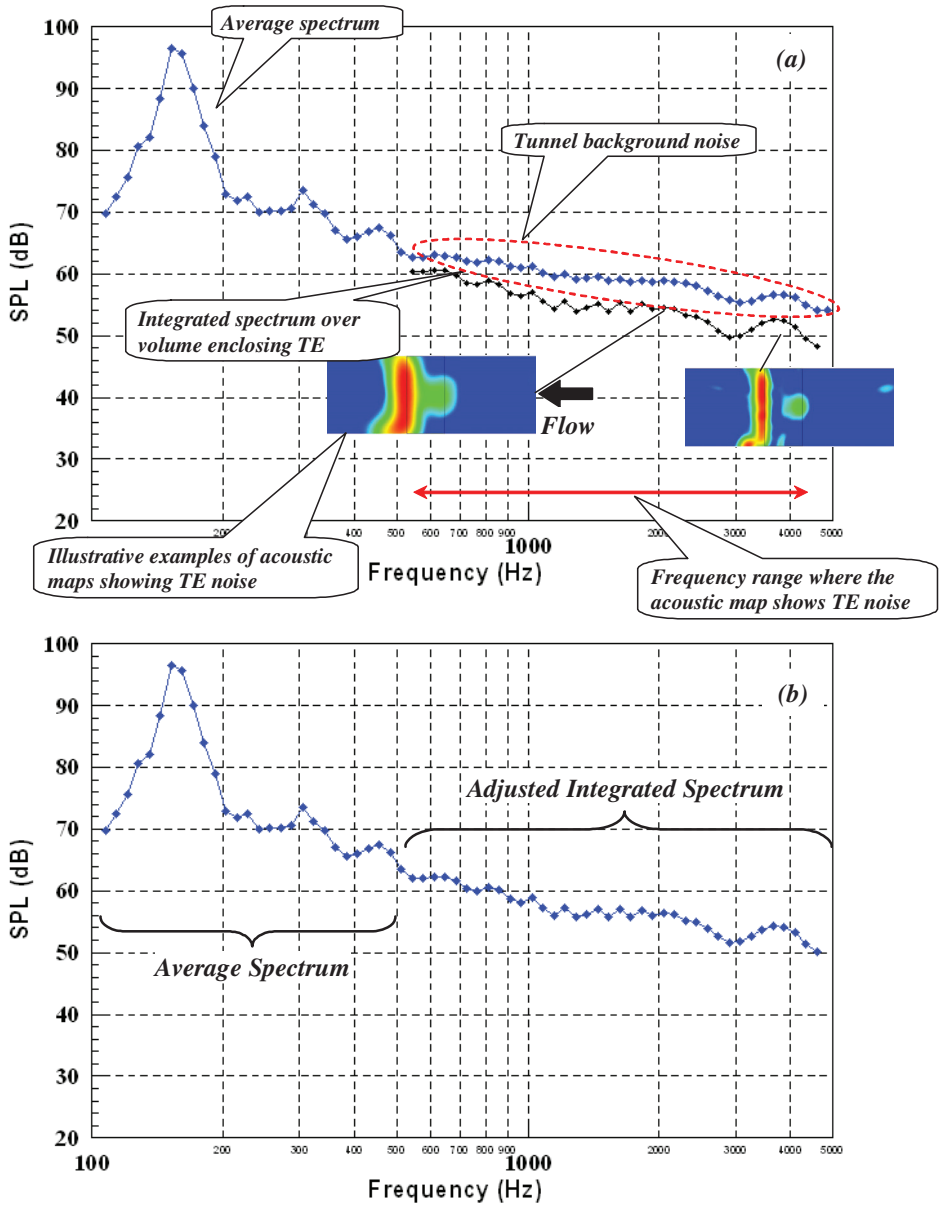

Figure 54. Description of typical noise spectrum of an airfoil model in 1/12th octave bands: (a) Average and integrated spectrum separately and (b) Average and adjusted integrated spectrum as a single trailing edge noise spectrum. Example: DU97-flatback without splitter plate at 5.1 degrees AoA at 56 m/s.

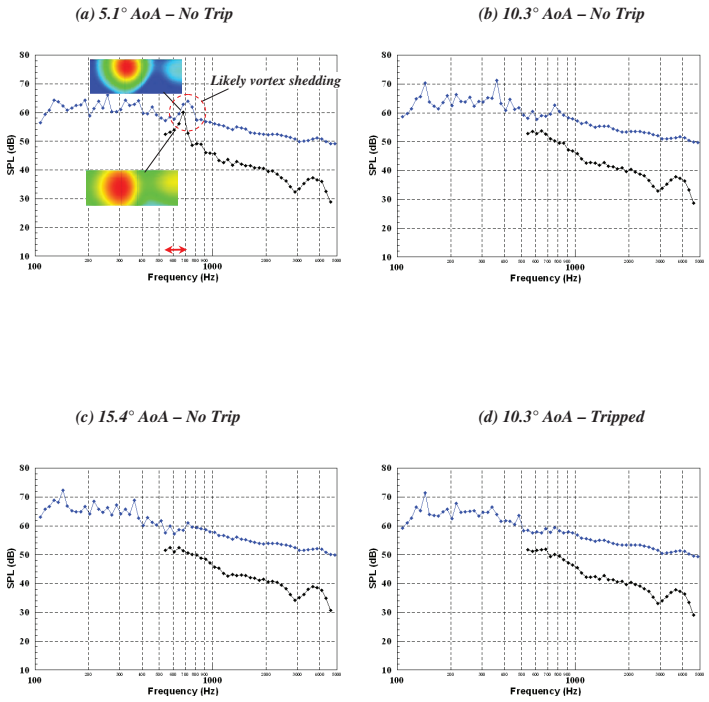

Figure 55. 1/12th octave band noise spectrum for the DU97-W-300 airfoil at $\sim$ 56 m/s flow speed.

Figures 55 through 57 show the average and integrated spectrum for the DU97-W-300 airfoil at 56, 44, and 28 m/s flow speeds, respectively. Unfortunately, the results for this airfoil do not show clear evidence of trailing edge noise in the acoustic maps except for a few frequency bands around 700 Hz for the 5.1 degrees AoA no trip at 56 m/s case (Figure 55(a)). The maps shown in this figure suggest a noise source from the upper half of the airfoil about 10 inches below the airfoil junction with ceiling. The only other conclusion that can be drawn from these plots for the DU97-W-300 airfoil is that the trailing edge noise must be below the spectra shown.

Figures 58 through 63 present the results for the DU97-flatback without and with splitter plate. The figures are organized such that the airfoil without and with the splitter plate are back to back for the same flow speed. This approach makes evaluating the effect of the splitter plate easier. Unlike the DU97-W-300 airfoil, there are cases where trailing edge noise was successfully identified and measured. Figure 58 shows the DU97-flatback without the splitter plate at a flow speed of 56 m/s for 5.1, 12.8, and 15.4 degrees geometric AoA. The plots show that for 5.1 degrees and 12.8 degrees (no trip and tripped), trailing edge noise was measured over the complete 500 to 5000 Hz frequency range. On the other hand, the higher blockage and consequent increase in tunnel background noise for the 15.4 degrees AoA case hindered the identification of trailing edge noise by the array. Figure 59 shows results for the same airfoil with the splitter plate. Comparing Figures 58 and 59 demonstrates that the splitter plate leads to significant noise reduction. Results for the other two flow speeds are shown in Figures 60 through 63. These results also show reduction in the noise levels with the splitter plate installed, but reliable integrated spectra were obtained for only a few cases.

(a) 5.1° AoA – No Trip

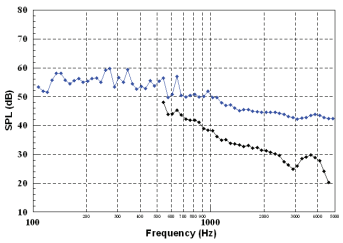

(b) 10.3° AoA – No Trip

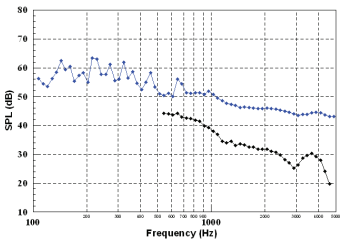

(c) 15.4° AoA – No Trip

No Data

(d) 10.3° AoA – Tripped

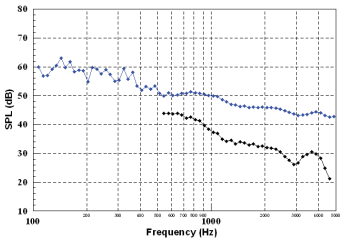

Figure 56. 1/12th octave band noise spectrum for the DU97-W-300 airfoil at $\sim$ 42 m/s flow speed.

(a) 5.1° AoA – No Trip

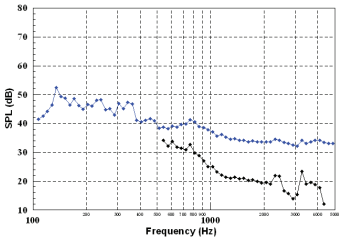

(b) 10.3° AoA – No Trip

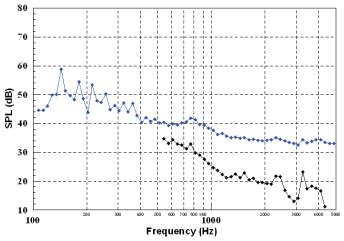

(c) 15.4° AoA – No Trip

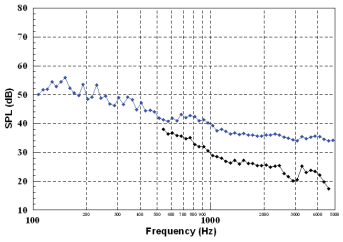

(d) 10.3° AoA – Tripped

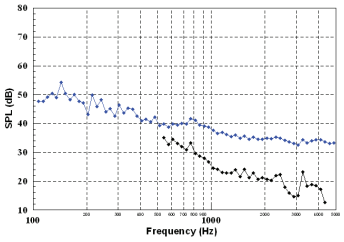

Figure 57. 1/12th octave band noise spectrum for the DU97-W-300 airfoil at $\sim$ 28 m/s flow speed.

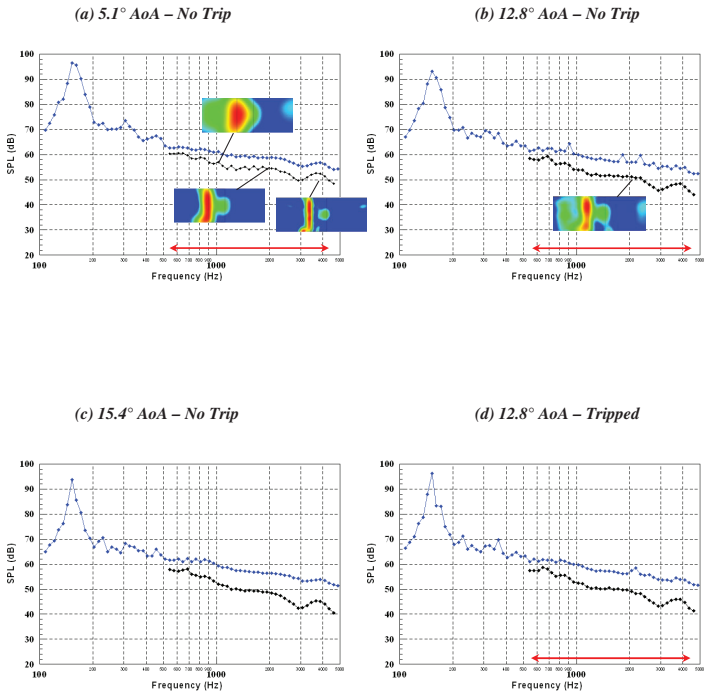

Figure 58. 1/12th octave band noise spectrum for the DU97-flatback airfoil without splitter plate at $\sim$ 56 m/s flow speed.

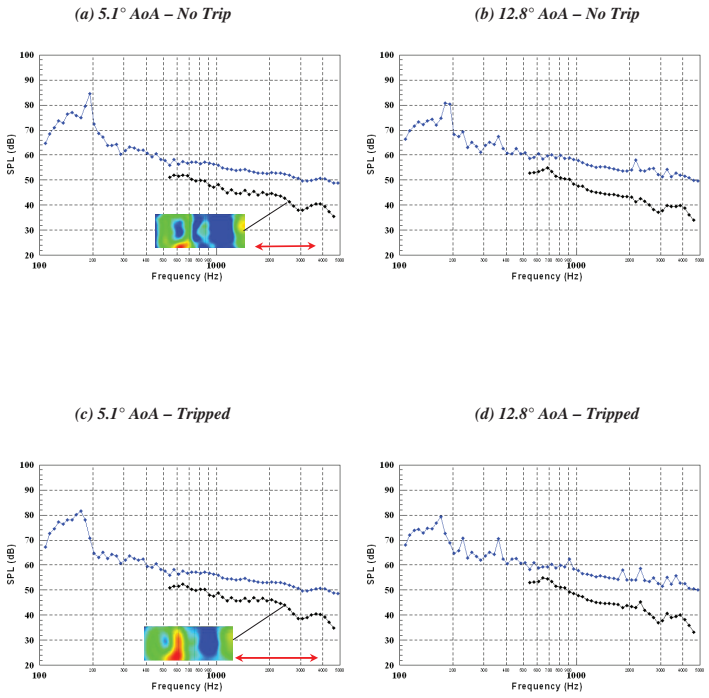

Figure 59. 1/12th octave band noise spectrum for the DU97-flatback airfoil with splitter plate at $\sim$ 56 m/s flow speed.

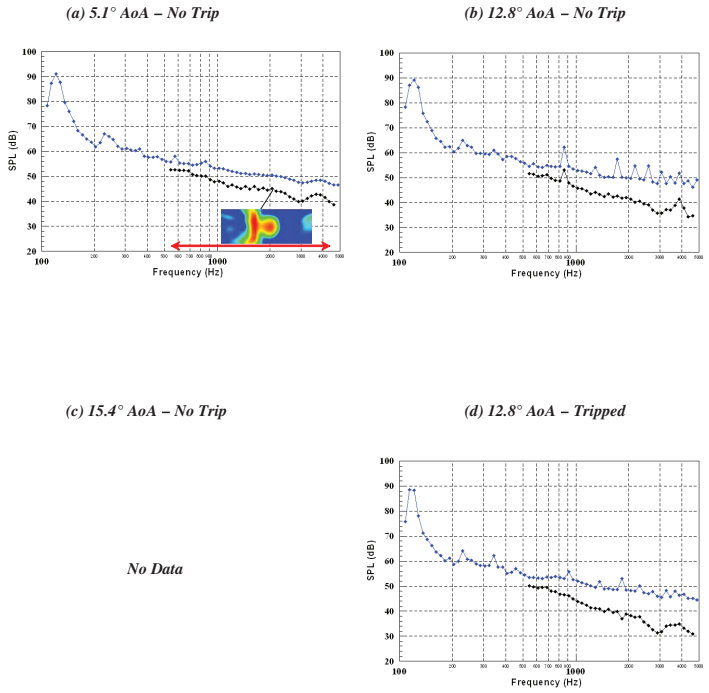

Figure 60. 1/12th octave band noise spectrum for the DU97-flatback airfoil without splitter plate at $\sim$ 43 m/s flow speed.

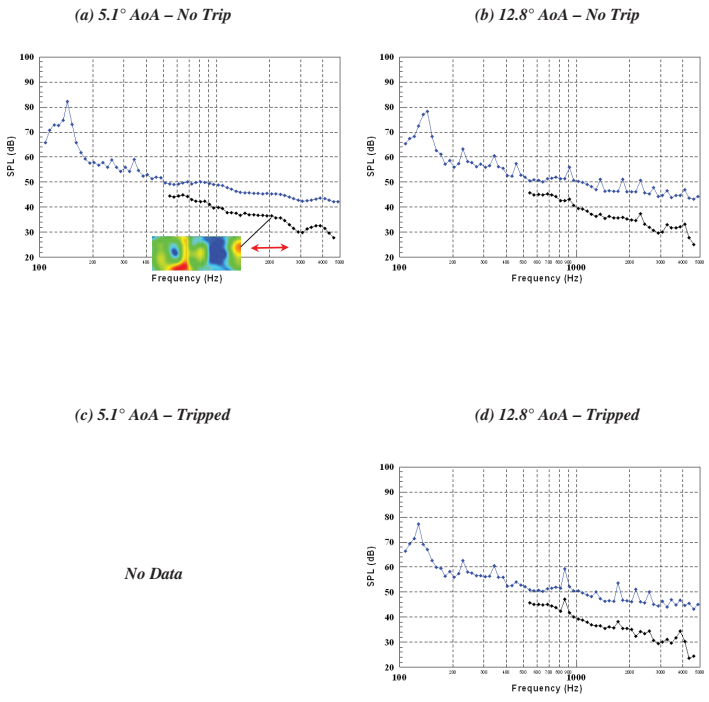

Figure 61. 1/12th octave band noise spectrum for the DU97-flatback airfoil with splitter plate at $\sim$ 43 m/s flow speed.

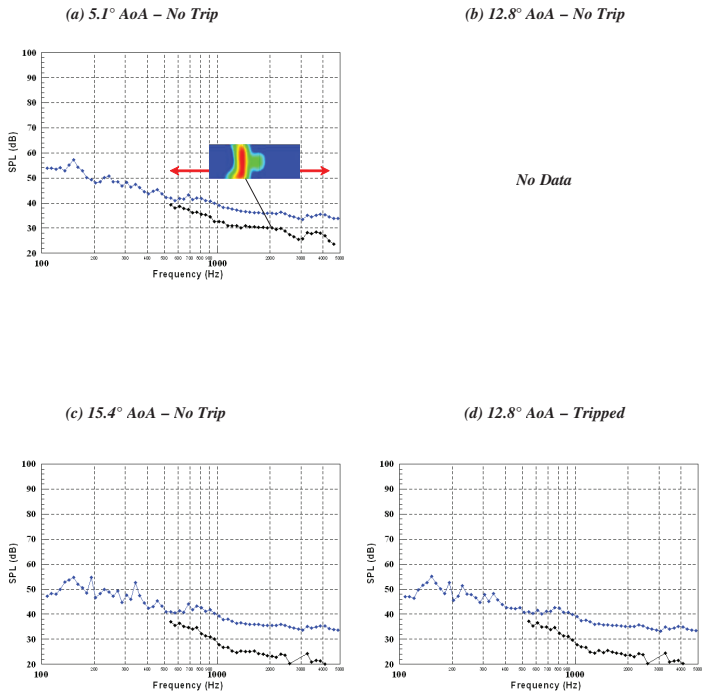

Figure 62. 1/12th octave band noise spectrum for the DU97-flatback airfoil without splitter plate at $\sim$ 28 m/s flow speed.

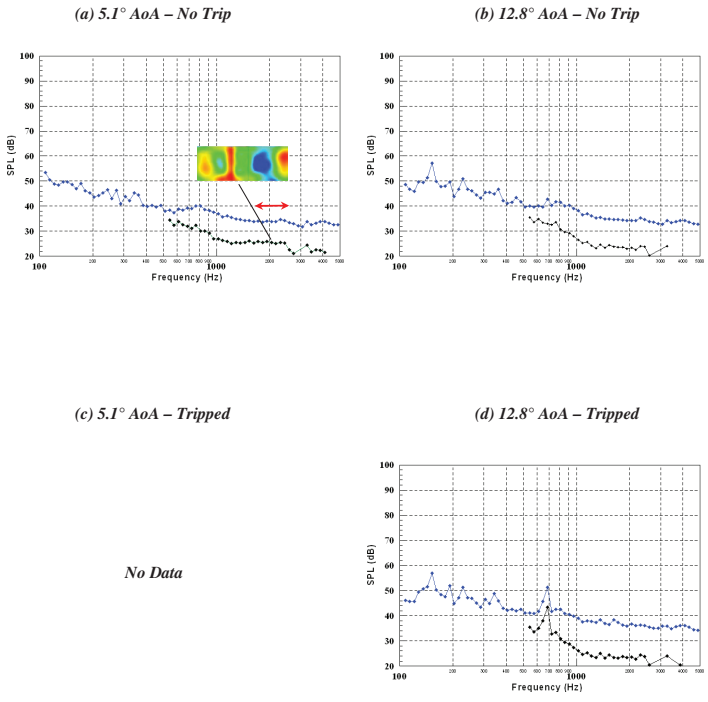

Figure 63. 1/12th octave band noise spectrum for the DU97-flatback airfoil with splitter plate at $\sim$ 28 m/s flow speed.

The full frequency range trailing edge noise spectrum for selected cases is shown in Figures 64 through 67. The trailing edge noise spectrum for the DU97-flatback airfoil at 5.1 degrees AoA for the three nominal chord Reynolds numbers of 1.6, 2.4 and 3.2 million is shown in Figure 64(a). The spectra normalized by the 6th power of the flow speed collapses reasonable well as shown in Figure 64(b). The scaling is particularly good for the 56 and 44 m/s cases. The effect of the splitter plate on the trailing edge noise is assessed in Figure 64 for the DU97-flatback airfoil at 5.1 degrees AoA at 56 m/s flow speed. In addition to the reduction of the vortex shedding noise, the rest of the spectrum was attenuated significantly, from 3-4 dB at 400 Hz to 10 dB at the higher frequencies. Figure 65 suggests a minor effect on the trailing edge noise due to the angle of attack at the highest flow speed case (remember that the noise maps for the 15.4 degrees AoA don't show trailing edge noise clearly). Figure 66 shows that tripping the DU97-flatback airfoil has a small effect on the trailing edge noise at the Reynolds number of 3.2 million, but only for frequencies above 1000 Hz.

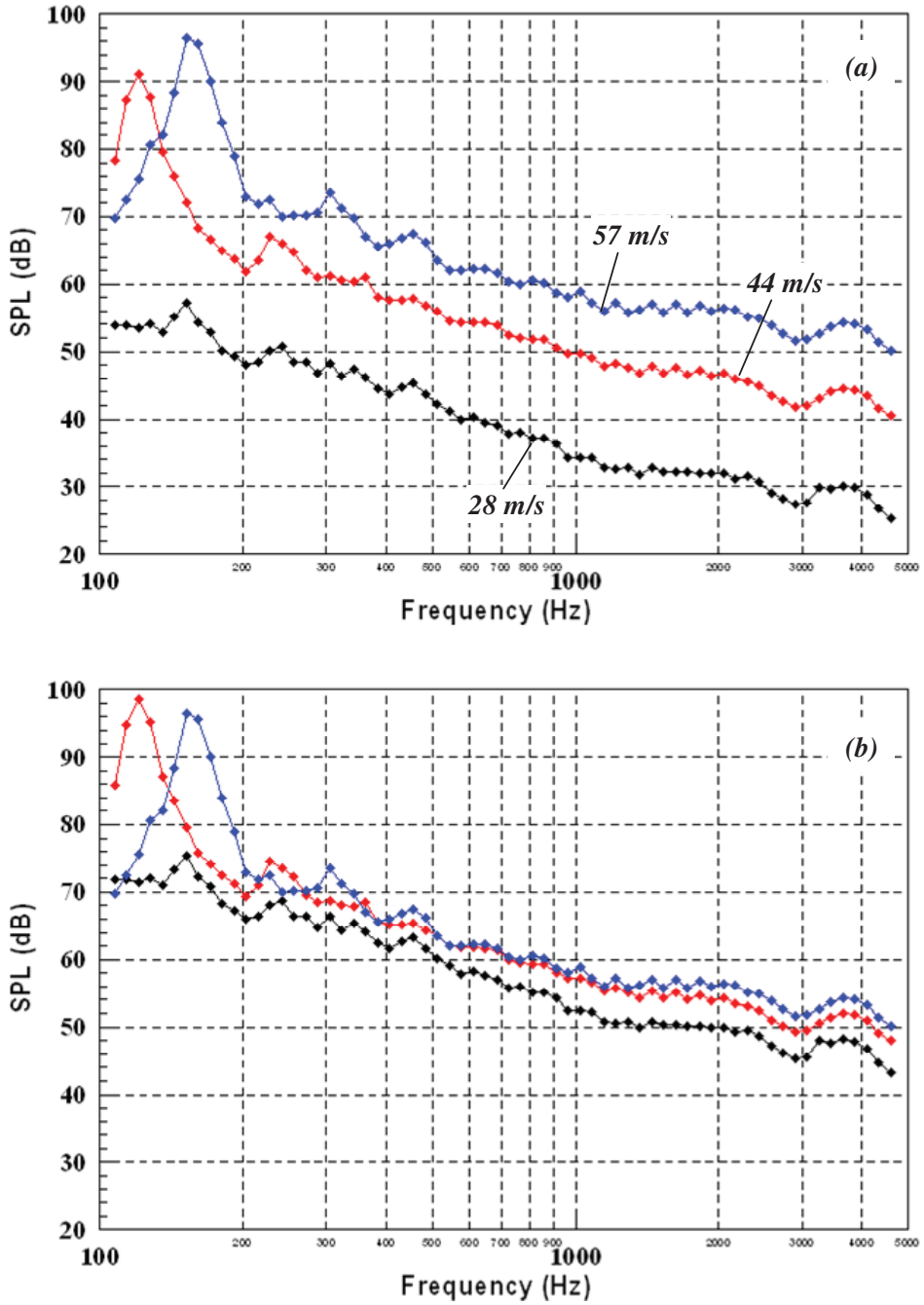

Figure 64. (a) Trailing edge noise spectrum for the DU97-flatback at 5.1 degrees geometric AoA for 57, 44, and 28 m/s and (b) scaled to the 6th power of the flow velocity. No trip.

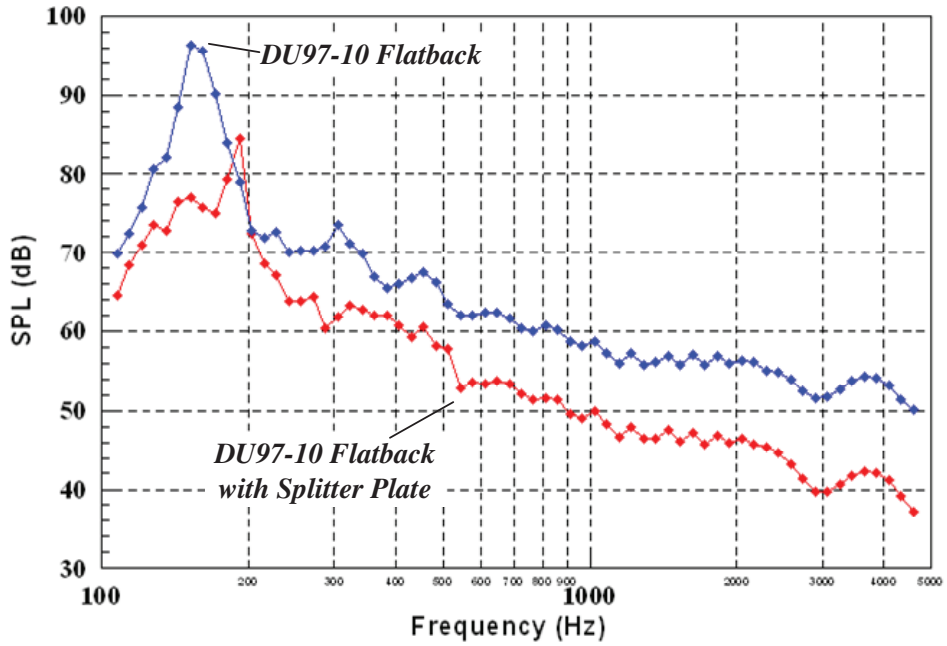

Figure 65. Trailing edge noise spectrum for the DU97-flatback with and without splitter plate at 5.1 degrees geometric AoA and $\sim$ 56 m/s flow speed. No trip.

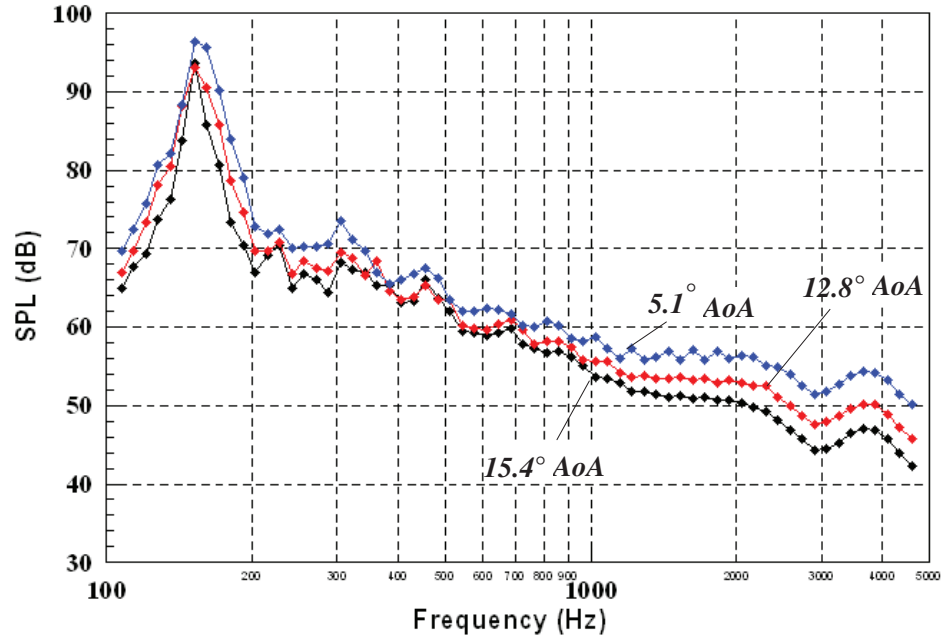

Figure 66. Trailing edge noise spectrum for the DU97-flatback at 5.1, 12.8, and 15.4 degrees geometric AoA and $\sim$ 56 m/s flow speed. No trip.

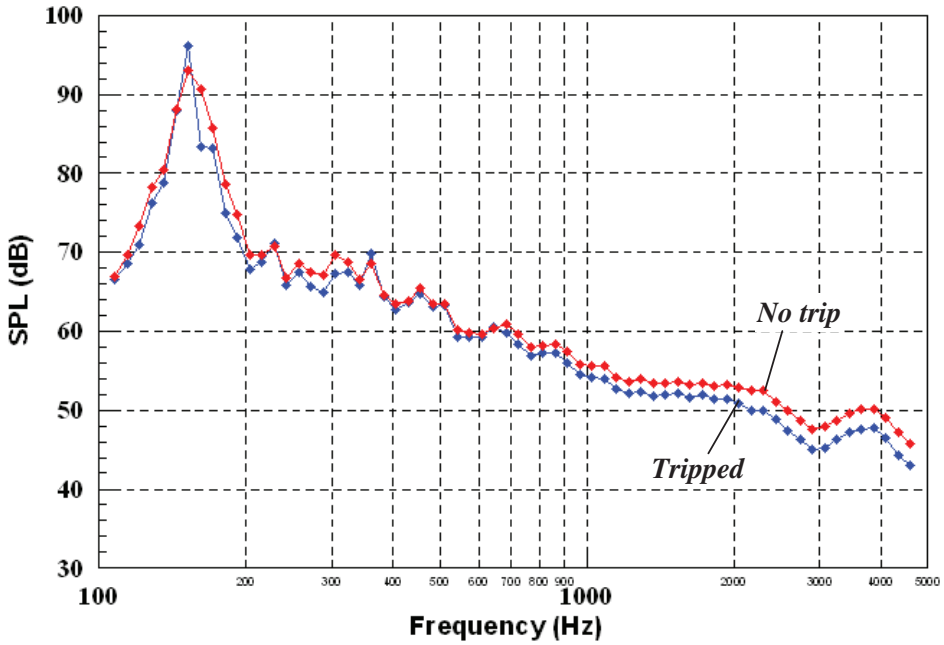

Figure 67. Trailing edge noise spectrum for the DU97-flatback at 12.8 degrees geometric AoA and $\sim$ 56 m/s flow speed, tripped and no trip.

6 Conclusions

Experimental wind tunnel results have been presented for the DU97-W-300 airfoil and a flatback version of that airfoil, operating at a chord Reynolds number ranging from 1.6 to 3 million. The aerodynamic portion of the experiment resulted in the following observations:

- The increase in lift curve slope and maximium lift coefficient for flatback airfoils that has been reported at lower chord Reynolds numbers ($<$ 1 million) is also observed at higher Reynolds numbers. The Reynolds numbers studied in the present experiment correspond more closely to the flow conditions that would be experienced by the inboad region of a utility-scale wind turbine blade.
- The increase in drag due to the blunt base of the flatback is large, as expected. However,the drag can be reduced by up to 50% using a simple splitter plate attachment, in accord with results at lower Reynolds number.
- The flatback airfoil has a larger nose-down pitching moment than the original airfoil. This effect is more pronounced at higher angle of attack than at low angle of attack.
- The flatback lift coefficient is relatively insensitive to boundary layer tripping applied near the leading edge, even at angles of attack approaching stall.

The acoustic measurements of the flatback airfoil and subsequent analysis lead to the following observations:

- A distinct vortex-shedding tone is present at a Strouhal number of approximately 0.24-0.25 (uncorrected for tunnel blockage) for the flatback airfoil. The Strouhal number of the shedding is relatively insensitive to boundary layer tripping, angle of attack, and Reynolds number.
- The intensity of the low-frequency trailing edge noise scales approximately with the sixth power of the flow velocity for the two higher velocity cases examined (44 and 56 m/s). The measured vortex-shedding tone at the lowest tunnel speed (28 m/s) is believed to be artificially attenuated by spurious reflection from the anechoic chamber walls.
- At Reynolds number of 3.2 million, the splitter plate attachment reduces the amplitude of the vortex-shedding tone by 12 dB and shifts the peak Strouhal number to 0.26-0.30.
- At Reynolds number of 3.2 million, increasing the geometric angle of attack from 5.1 to 15.4 degrees reduced the peak SPL by about 4 dB for the flatback with and without the splitter plate.
- At Reynolds number of 3.2 million, tripping the boundary layer near the leading edge of the flatback resulted in an increase of the peak noise intensity by about 3-4 dB over the free-transition case at a geometric angle of attack of 12.8 degrees.

Appendix A Development of Porous Wall Wind Tunnel Corrections

Over the course of the present experiment, it became apparent that simple downwash corrections that had been previously applied to measurements for relatively thin, symmetric airfoils were not adequate for the present configuration. In order to support development of corrections to aerodynamic data taken in the acoustic test section, a sequence of measurements was made on the DU97-W-300. Measurements included surface pressure distributions on the airfoil, pressure distributions over the Kevlar side walls and measurements of the deflection of the Kevlar side walls. Additionally, flow quality studies were performed, including examination of the effect of airfoil fences as well as tuft flow visualization of the airfoil and Kevlar side-wall surface flows. This Appendix describes the measurements and how they were used to develop porous wall interference and blockage corrections for the acoustic test section.

A.1 Apparatus and Instrumentation

Measurements were performed using the same setup described in Section 2. The reader is referred to that section for the details of the wind tunnel, acoustic test section, DU97-W-300 airfoil model and mount, and other hardware which are not repeated here.

Additions to the above setup unique to the follow-on measurements are described below. These include new pressure instrumentation, instrumentation for measuring the deflection of the Kevlar acoustic windows and the pressure distributions across those windows, fences mounted to the ends of the airfoil model with the intention of promoting two-dimensional flow, material used for tuft flow visualizations, and measurements of the porosity of the Kevlar material.

A.1.1 Instrumentation and flow visualization

All pressures were recorded using an Esterline 9816/98RK pressure scanner with 48 channels with a range of $\pm$10 inches of water column and 48 channels with a range of $\pm$2.5psi. The system has a rated accuracy of $\pm$0.05% full scale. Almost all pressure measurements were at free stream velocities of 30m/s or less permitting use of a $\pm$10 inch H_2O range.

The pressure distribution over the interior surfaces of the Kevlar acoustic windows was measured using a set of Dwyer straight Pitot static probes with a 1.6 mm diameter and measuring 0.43 m in length. The probes were mounted on a horizontal 7.6-m long aluminum rail mounted along the inside of the acoustic window (Figure A.1). A series of aluminum standoffs were used to position the probes some 0.28m from the rail. With multiple probes attached to the rail, and by mounting the rail at different heights, static pressure measurements over the interior surface of each window were made (measured Pitot pressures were not used). Pressures in each of the anechoic chambers were also recorded so that pressure differences across the Kevlar could be calculated.

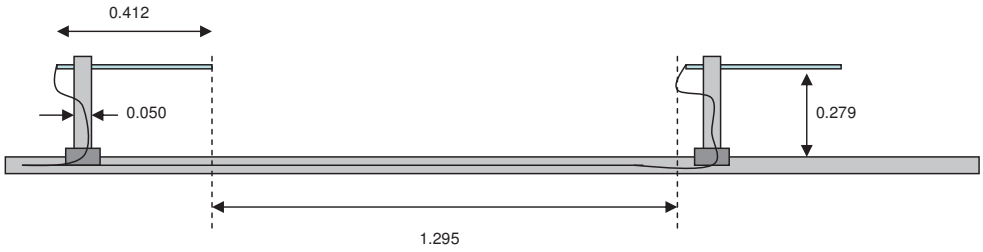

Figure A.1. Photograph and diagram showing the system of Pitot static tubes used to measure the pressure distributions over the inside of the Kevlar acoustic windows, adapted from Crede [8].

At some conditions, flow visualizations were performed on the inside surfaces of the acoustic windows using tufts made from Nylon yarn. The tufts were placed in a square grid pattern with a separation of about 30cm over the whole surface of the window. Tuft flow visualizations were also performed at some conditions on the surfaces of the airfoil models to examine the two-dimensionality of the flow and to check for separation. The same tuft material was used but tufts were attached in a much denser pattern. Note that tufts were removed before making surface pressure measurements.

The shape of the Kevlar window was measured using 12 Sharp GP2D12 infra-red sensors mounted on an aluminum frame. Each sensor was calibrated using Kevlar fabric stretched on a model frame. The sensors were spaced every 28cm on a beam that was aligned in the streamwise direction inside of the acoustic chamber. The streamwise beam was consequently mounted on a vertical beam that allowed the deflection measurements at 5 vertical positions.

Absolute airfoil position and angles in the test section was measured either with a FARO Arm coordinate measuring machine (nominal accuracy 0.074mm), or by measuring distances between the points on the airfoil, or a long straight edge placed parallel to the airfoil chordline and the wind tunnel walls, using a conventional tape measure. Absolute accuracy of the angle between the chordline and centerline of the tunnel test section was 0.2 degrees.

A.2 Airfoil Model Fences

For some measurements, boundary layer fences were attached near the ends of the DU97-W-300 airfoil model. Boundary layer fences are usually employed as a way to prevent 3-dimensional end effects from contaminating the flow over the central portion of the airfoil. Measurements made with and without fences were compared in the present study to reveal the importance of end effects on the airfoil flows. The fences consisted of 6-mm thick aluminum plates cut with an inner boundary matching the shape of the airfoil profile, and an elliptical outer boundary, with its major axis forming an extension of the airfoil chord line. The major and minor axes of the ellipse were 1100mm and 394mm with the ellipse protruding 100mm forward of the leading edge, and with an angle of 0.8 degrees between the ellipse axis and the airfoil chordline in the direction of positive angle of attack. The fences were placed 235mm inboard of the ends of the models.

A.3 Porosity of the Kevlar windows

The Kevlar 120 scrim material is not impermeable, but has about a 6% open area ratio. Thus the local pressure differences across the Kevlar windows can induce local flow through them. We are therefore interested in the relationship between pressure difference across the Kevlar scrim and the velocity of the flow through it, since this forms one of the test section boundary conditions. To determine this relationship, a sequence of two tests were performed, as illustrated in Figure A.2.

In the first test a Kevlar sample was stretched across the mouth of a PVC pipe over which was

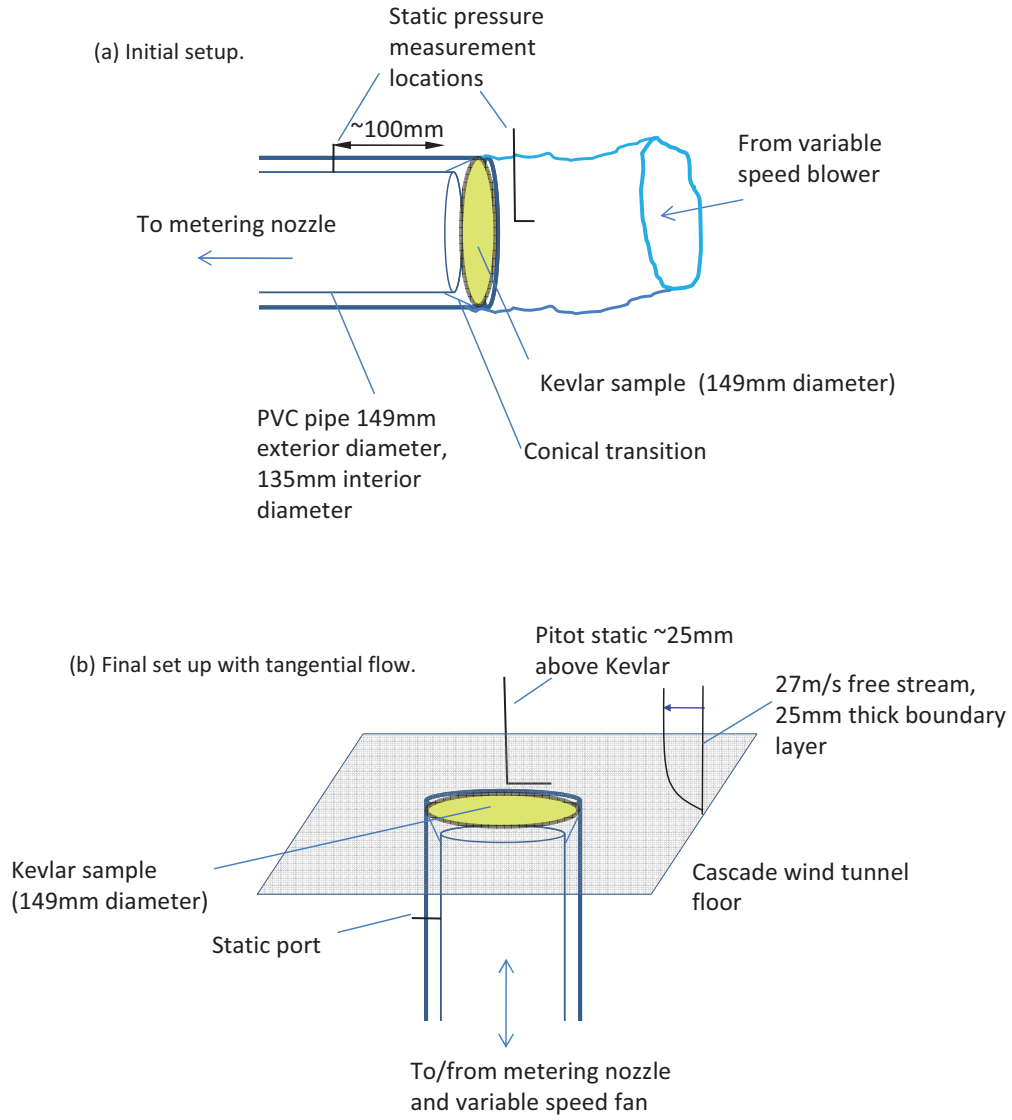

Figure A.2. Test setups used to measure the relationship between the pressure difference across the Kevlar and the transpiration flow. (a) Initial setup. (b) Final setup with tangential flow.

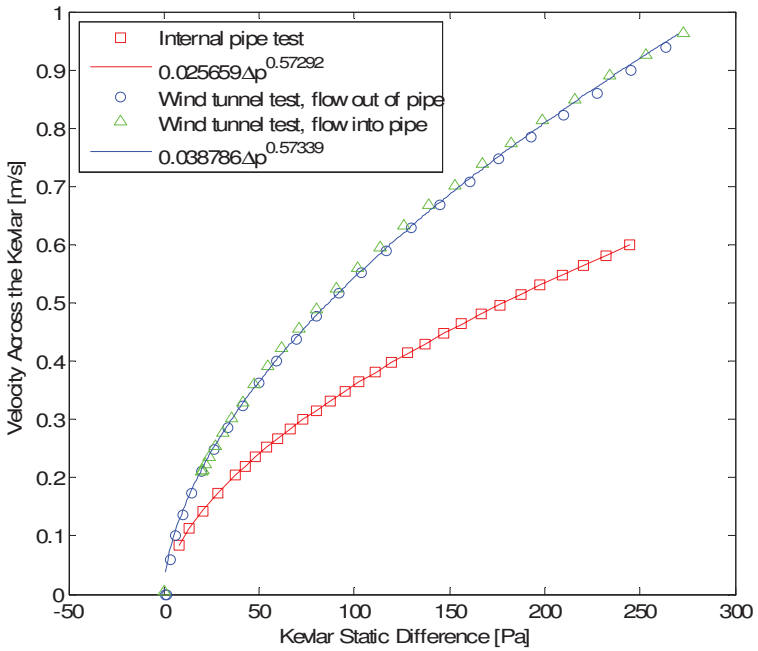

Figure A.3. Pressure-velocity relationship for the Kevlar 120 scrim measured using the setup shown in Figure A.2.

fitted a flexible duct delivering air from a variable speed fan, Figure A.2(a). Static pressure in front of the Kevlar sample was measured using a miniature static probe. The pressure downstream was recorded using a static tap mounted in the wall of the pipe. Air from the pipe was exhausted through a metering nozzle. Pressure difference across the sample was measured as a function of flow speed, for conditions similar to those experienced by the acoustic windows of the Stability Tunnel test section. Measurements made at the static port were corrected for the short conical contraction between the sample and the interior of the PVC pipe. Results, illustrated in Figure A.3, fall on a smooth curve accurately described by the function

$$V = 0.0257\Delta p^{0.5729} \tag{10}$$

Where p is the pressure difference across the Kevlar in Pascals, and V is the average flow velocity through it in meters per second.

The second test was designed to more realistically model conditions experienced at the acoustic windows. Here the Kevlar sample and the PVC pipe were mounted vertically, with the Kevlar flush with the test wall of a cascade wind tunnel, Figure A.2(b). At the location of the Kevlar the wind tunnel boundary layer was close to 25mm thick, with a free stream velocity of some 25m/s. Air was then drawn either in or out through the Kevlar by means of the variable speed fan, the flow rate again being measured using the metering nozzle. In this test, static pressure above the Kevlar sample was recorded using a Pitot-static probe aligned with the tunnel free stream. Measurements were made with and without the wind tunnel flow, and with both directions of flow through the Kevlar. Results, in Figure A.3, show almost the same relationship between velocity and pressure with the wind tunnel flow on and with flow through the Kevlar in either direction. Results measured

without wind tunnel flow follow almost the same curve. All the data, however, indicate higher velocities through the Kevlar than the initial test, with the relationship being closely described by the function

$$V = 0.038786\Delta p^{0.57339} \tag{11}$$

We believe that this second relationship is more reliable since the setup more accurately replicates Stability Tunnel conditions. Furthermore, the measurement accuracy of the static pressure above the Kevlar in the cascade tunnel configuration was significantly better than that in the flexible duct of the original configuration.

A.4 Experimental Results

Mean surface pressure distributions were measured at a nominal freestream velocity of 30 m/s. Three angles of attack were tested, all without boundary layer trips. Boundary layer fences were also used for a few runs and are discussed briefly here. Additionally, window surface pressure and deflection distributions were measured at two angles of attack. The different test conditions investigated are the 30.0 m/s cases reported previously in Table 2.

A.4.1 Surface Pressure Distributions

Pressure distributions on the DU97-W-300 were measured at geometric angles of attack of 0, 6.7, and 13.2 degrees, and are plotted in Figures A.4 to A.6. At 0 and 6.7 degrees geometric angle of attack, the fences have virtually no effect on the measured pressure distribution. Tuft flow visualization on the Kevlar windows at 6.7 degrees showed the flow to be well behaved at all positions, with no sign of flow separation. At a geometric angle of attack of 13.2 degrees, tuft flow visualization on the Kevlar windows again did not show any sign of flow separation. However, the addition of fences produced a sizeable increase in pressure over the first 40% chord on the suction side as shown in Figure A.6. Beyond this location, the distribution seems to exhibit signs of stall (initiated at the junction between the airfoil and the fences, as revealed by tuft flow visualization seen in Figure A.7).

Pressure distributions were also measured on the Kevlar windows for the DU97-W-300 at 6.7 and 13.2 degrees. The results are presented in Figures A.8 and A.9 for 6.7 and 13.2 degrees respectively. The data is presented in terms of a pressure coefficient difference ΔC_p defined as

$$\Delta C_p \equiv \frac{p_w - p_s}{\frac{1}{2}\rho_\infty U_\infty^2} \tag{12}$$

where p_w is the local window surface pressure and p_s is the acoustic chamber pressure.

The window pressure measurements in Figures A.8 and A.9 are plotted against the streamwise distance (referenced at the quarter chord of the model) on the horizontal axis. The plots present the window pressure for the port chamber (suction side) in solid lines and for the starboard chamber

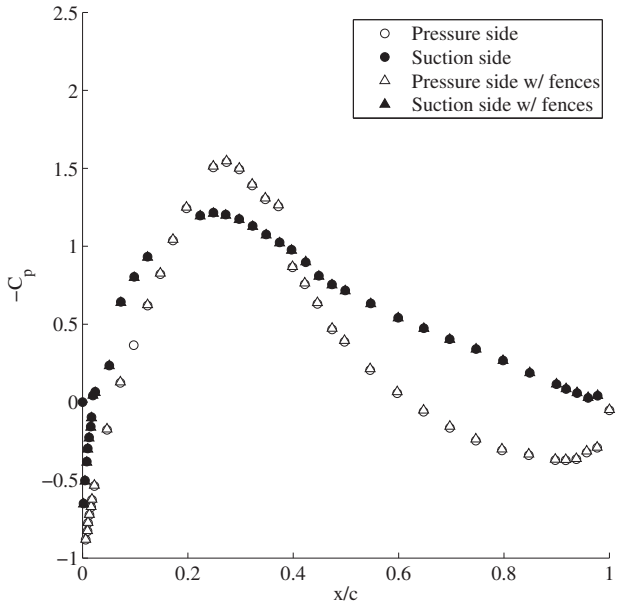

Figure A.4. Measured pressure distribution for the DU97-W-300 airfoil at 0 degrees geometric angle of attack without boundary layer fences and with boundary layer fences installed 235mm from the end walls.

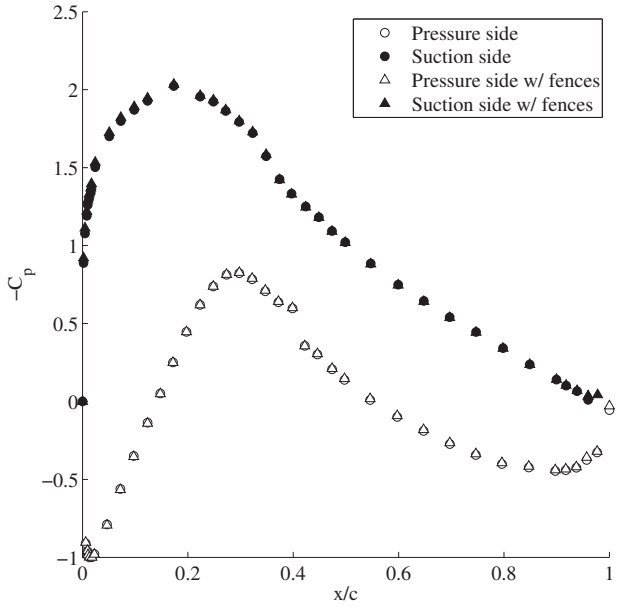

Figure A.5. Measured pressure distribution for the DU97-W-300 airfoil at 6.67 degrees geometric angle of attack without boundary layer fences and with boundary layer fences installed 235mm from the end walls.

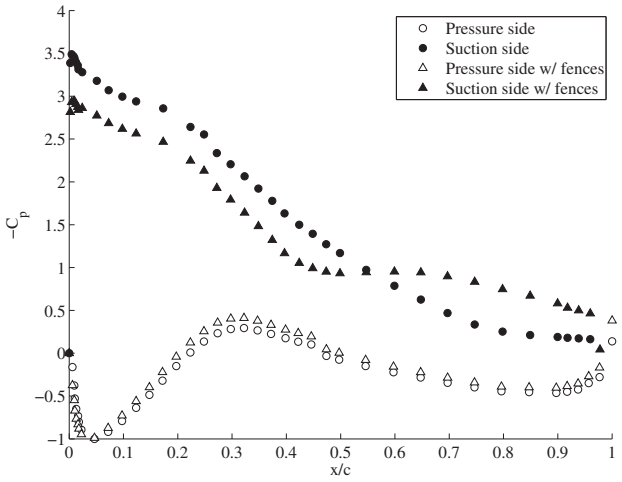

Figure A.6. Measured pressure distribution for the DU97-W-300 airfoil at 13.2 degrees geometric angle of attack without boundary layer fences and with boundary layer fences installed 235mm from the end walls.

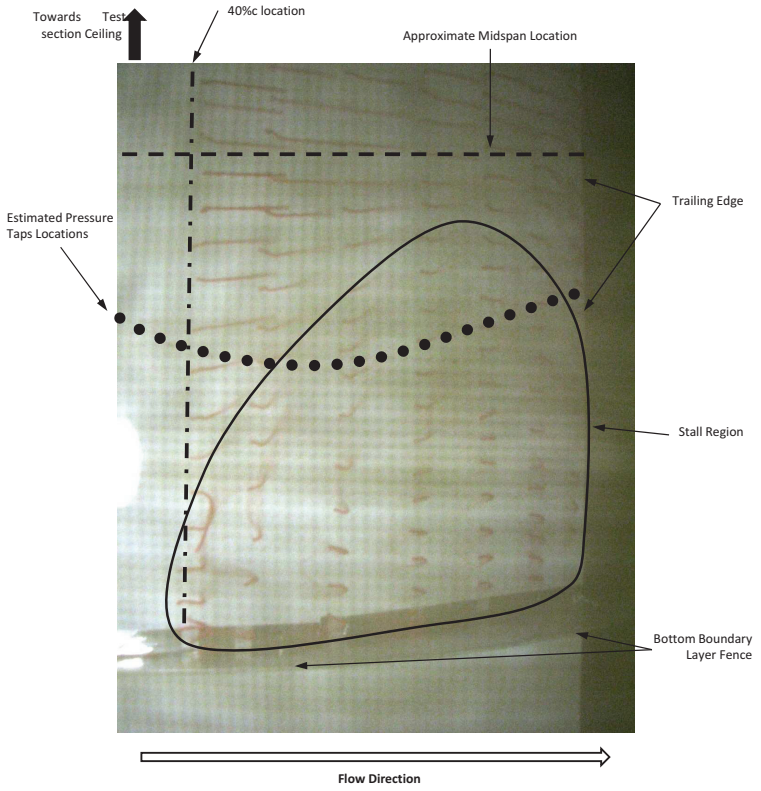

Figure A.7. Tuft flow visualization on the suction side of the DU97-W-300 airfoil with boundary layer fences at a geometric angle of attack of 13.2 degrees as seen from the port acoustic chamber.

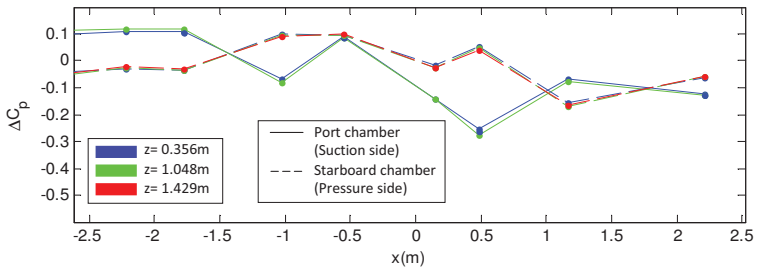

Figure A.8. Surface pressure distributions measured on the Kevlar windows during testing of the DU97-W-300 airfoil at a geometric angle of attack of 6.67 degrees.

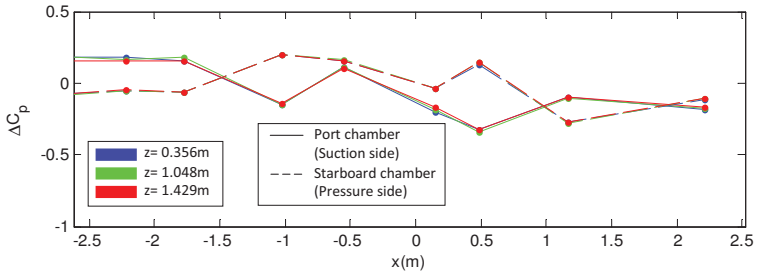

Figure A.9. Surface pressure distributions measured on the Kevlar windows during testing of the DU97-W-300 airfoil at a geometric angle of attack of 13.2 degrees.

(pressure side) in dashed lines. The pressures are plotted for the three vertical locations of z=0.356 m, 1.048 m, and 1.429 m in blue, green, and red, respectively.

In addition, deflection measurements were also made using the infra-red sensors described in Section A.1.1. The results are presented in Figures A.10 and A.11 as contour maps of the Kevlar deflection (in meters) plotted against the streamwise distance x (referenced at the model quarter chord) on the horizontal axis and the distance along the height of the test-section z on the vertical axis (both expressed in meters). A positive deflection indicates that the Kevlar window is deforming into the flow. The scales of the horizontal axes of Figures A.8 to A.11 are identical to allow for direct comparisons.

At 6.7 degrees, Figure A.8 shows that the pressure on the starboard window is mainly positive, meaning that the pressure inside that chamber is lower than in the test-section. Such positive pressure difference is consistent with the negative deflection (i.e. towards the chamber) with a maximum magnitude of 0.03 m that can be seen as the dominating feature in Figure A.10. On the suction side window (i.e. port), the pressure difference is mainly negative (indicating that flow is being sucked out of the port chamber into the test-section), with a region of positive pressure difference between x=-2.62 and -1.5 m. Such pressure distribution translates into negative deflections (out of the flow) from x=-2.62 to -1.5 m, and positive deflections further downstream as seen in Figure A.10. The region of negative deflection on the starboard side in Figure A.10 has a peak of

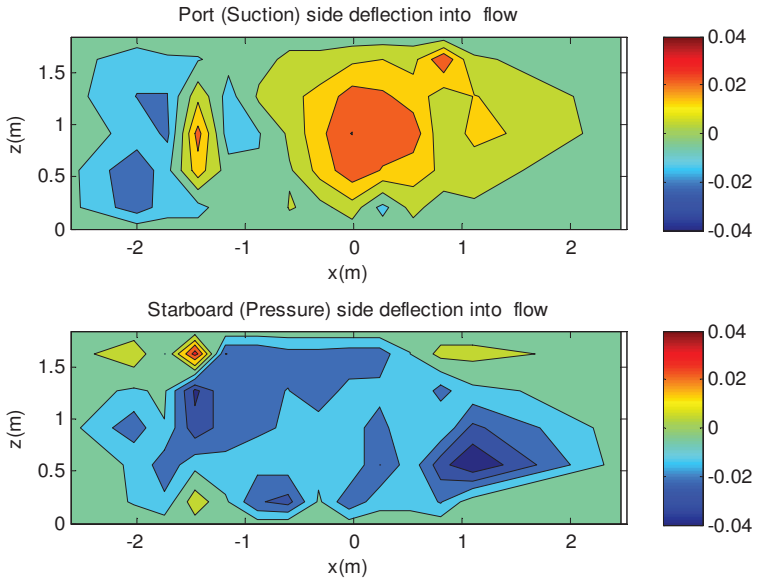

Figure A.10. Kevlar window deflection measured during the testing of the DU97-W-300 airfoil at a geometric angle of attack of 6.67 degrees. Deflections in meters.

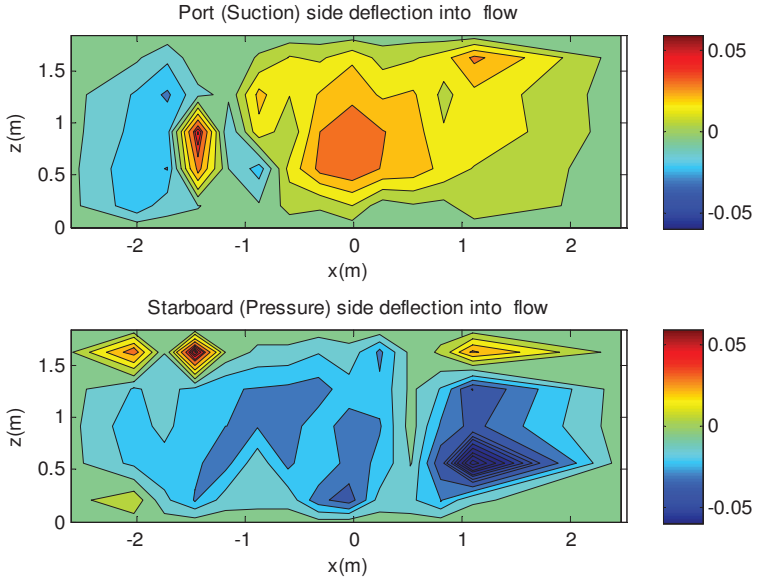

Figure A.11. Kevlar window deflection measured during the testing of the DU97-W-300 airfoil at a geometric angle of attack of 13.2 degrees. Deflections in meters.

0.021 m. The maximum positive deflection (into the flow) on the port side is 50% greater (0.031 m) and occurs at the streamwise location of the quarter chord (x=0 m). While one would expect the pressure along the port side window to vary monotonically, Figure A.8 shows two negative peaks occurring at x=-1 and 0.5 m. The local increase in the pressure difference seen around x=-0.5 m does not seem natural and could be the result of clogged static ports on one of the probes used in this set-up. Note that on both windows, the collapse of the different colored lines indicates that there is great spanwise uniformity along the Kevlar windows.

Figure A.9 shows that variations in the pressure distributions on the windows at a geometric angle of attack of 13.2 are very similar to those measured at 6.7 . However, the magnitudes involved are almost twice as large (notice that the scale of the vertical axis on Figure A.9 is twice that of Figure A.8). A quick comparison of Figures A.9 and A.11 reveals that the same remark can be made for the deflections. On the starboard window (associated with the pressure side of the airfoil), the deflections are primarily negative with a peak of 0.07m occurring near the trailing edge of the DU97-W-300. On the suction side (port window), the maximum deflection into the flow (0.04 m) still occurs at the quarter chord, with a lobe of negative deflections (with a peak of -0.02 m) upstream of the leading edge.

A.5 Interference Calculations and Corrections

Calculations were made to model the effects of the wind tunnel walls on the airfoil aerodynamics using a hybrid panel method extended to account for presence of the wind tunnel walls and acoustic windows, and the transpiration of air into or out of the test section through the windows. The method consists of several components that are solved together; a conventional panel method model of the airfoil, a panel model of the wind tunnel walls, and a model for the flow through the acoustic windows. In addition to the panel method, theoretical models have been developed to provide correction formulae for the effects of porosity.

A.5.1 Airfoil model

A standard linear vortex panel scheme was used to model flow around the airfoils. The scheme was used by itself to compute the free-flight aerodynamics of the airfoils (for comparison), and as part of the hybrid interference method.

The design shapes of the airfoils were each discretized into 200 straight vortex panels of linearly varying strength. A control point was placed at the center of each panel. The panel strengths were inferred by requiring that the non-penetration condition be satisfied at each of the control points and that the Kutta condition be satisfied at the trailing edge. The handling of the Kutta condition required particular care because the DU97-W-300 has a non-negligible trailing edge thickness of about 1.7% of chord, which would be expected to shed a significant wake. The generation of the wake was modeled by placing a source panel of constant strength across the blunt base of the trailing edge, between points A and B as illustrated in Figure A.12. Points A and B are also

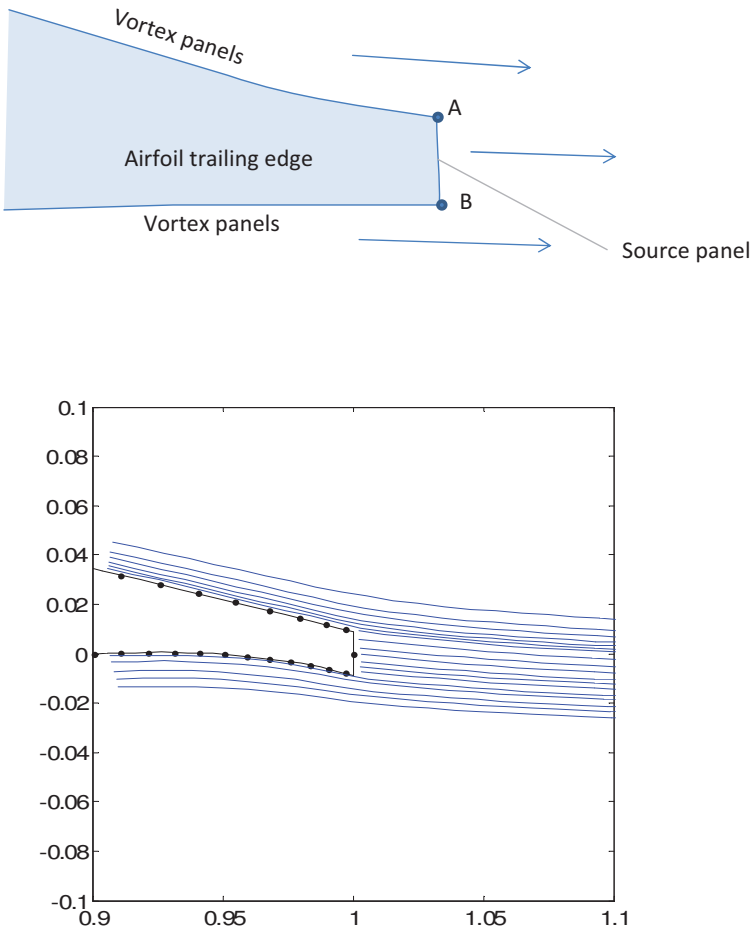

Figure A.12. Finite trailing edge modeling. Top: Schematic showing the position of the source panel. Bottom: Streamlines in the immediate vicinity of the DU97-W-300 in free flight at 8 degrees angle of attack.

at the edges of the first and last vortex panels that model the remainder of the airfoil. The Kutta condition is set by requiring that the vortex panel strengths at A and B be equal and opposite. This implies that the velocities tangent to the upper and lower surfaces of the airfoil are equal at these points, and thus the pressures the same. The wake is modeled by requiring that the strength of the source panel match the strength of the vortex panels at A and B, so that the flow velocity out of this panel matches that on either side of the trailing edge. This method produces streamlines that vary smoothly and realistically in the immediate vicinity of the trailing edge, as shown in Figure A.12.

The panel method was validated against the well-known Xfoil code (Drela [13]), for a NACA 0012 airfoil. Xfoil includes a panel method solver, used to generate inviscid solutions to free-flight airfoil problems, and a coupled boundary layer solver used to model viscous effects. Figure A.13 compares pressure distributions computed using the present method and Xfoil running in inviscid mode at 8 degrees angle of attack. The pressure distributions appear indistinguishable. The

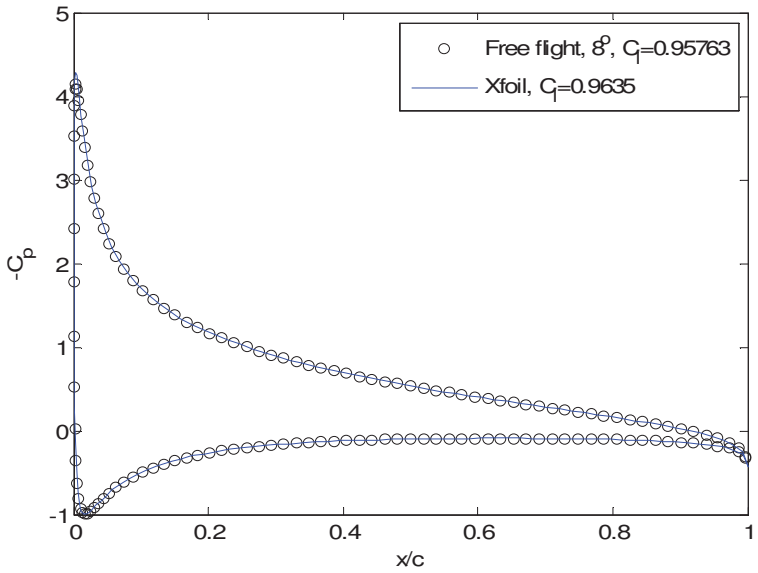

Figure A.13. Comparison of computed pressure distributions for a NACA0012 airfoil at 8 degrees angle of attack using the present panel method and using Xfoil in inviscid mode.

predicted lift coefficients are within 0.6% of each other.

While the ideal-flow method appears accurate, it is important to keep in mind that it is not a complete flow model and viscous effects on the pressure distribution and lift coefficient are not necessarily negligible. For example, running Xfoil in viscous mode for the NACA 0012, at a chord Reynolds number of 400,000, shows that viscous effects noticeably reduce the pressure difference between the pressure and suction sides of the airfoil, lowering the predicted lift coefficient by almost 10% to 0.876. Such effects are not negligible compared to typical wind tunnel interference corrections.

It is important to stress that the inviscid modeling of the blunt trailing edge is, to some extent, subjective and this subjective choice plays a substantial role in determining the aerodynamic characteristics when the trailing edge is thick, specifically in the case of the DU97-W-300. Figures A.14 and A.15 show the results of a series of calculations to illustrate this point. Figure A.14 compares pressure distributions computed for the DU97-W-300 at 8 degrees angle of attack using the present panel method, and using Xfoil in inviscid and viscous mode (for a Reynolds number of 1,600,000). Figure A.15 shows the same set of calculations but performed with the airfoil profile modified to sharpen the trailing edge, as shown in Figure A.16.

For the blunt trailing edge (Figure A.14), there is substantial disagreement between the present method and Xfoil inviscid. The present method predicts significantly smaller negative pressures on the airfoil suction side and a lift coefficient that is almost 10% smaller than Xfoil. Interestingly, the agreement between the present method and the viscous Xfoil calculation is much better. With the sharp trailing edge (Figure A.15), however, it is the inviscid Xfoil solution and the present method that are in agreement. The viscous Xfoil solution shows much lower pressure differences between

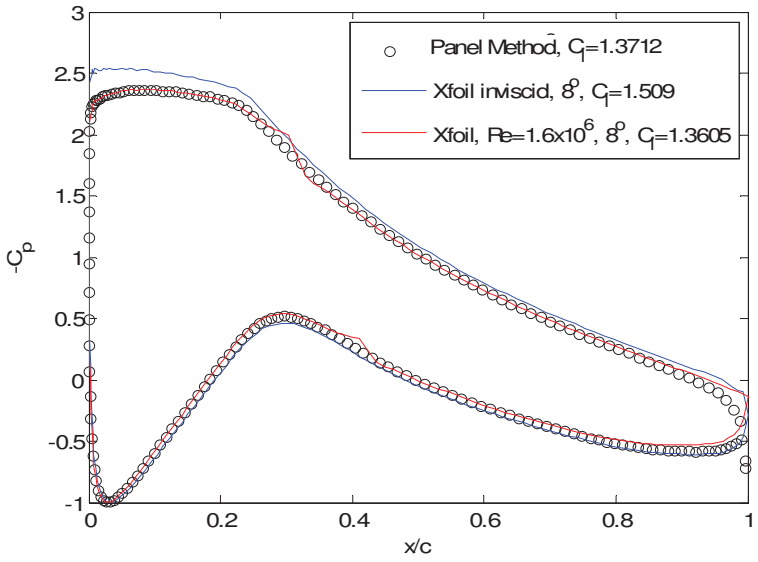

Figure A.14. Comparison of computed pressure distributions for the DU97-W-300 airfoil at 8 degrees angle of attack using the present panel method and using Xfoil.

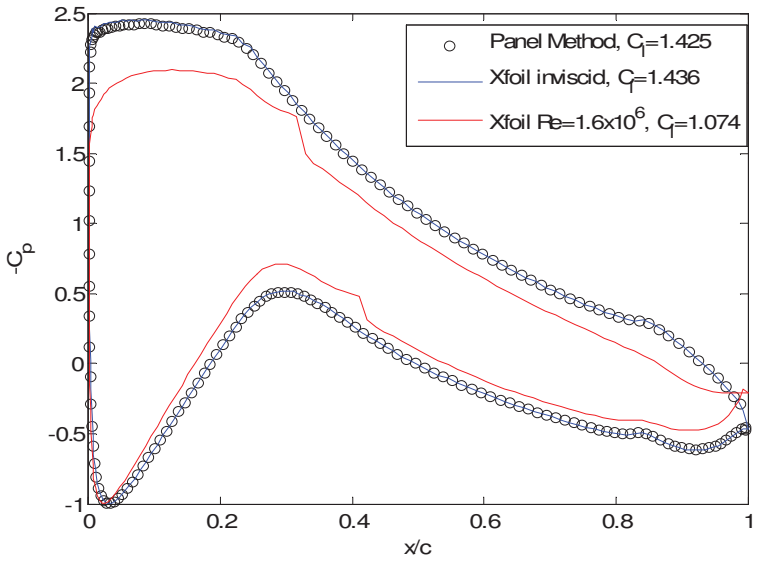

Figure A.15. Comparison of computed pressure distributions for the modified sharp trailing edge DU97-W-300 airfoil at 8 degrees angle of attack using the present panel method and using Xfoil.

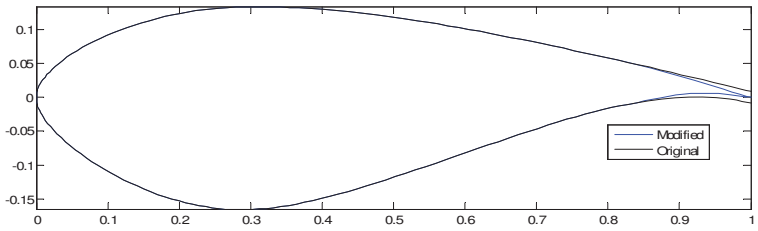

Figure A.16. Modified DU97-W-300 profile with a sharp trailing edge.

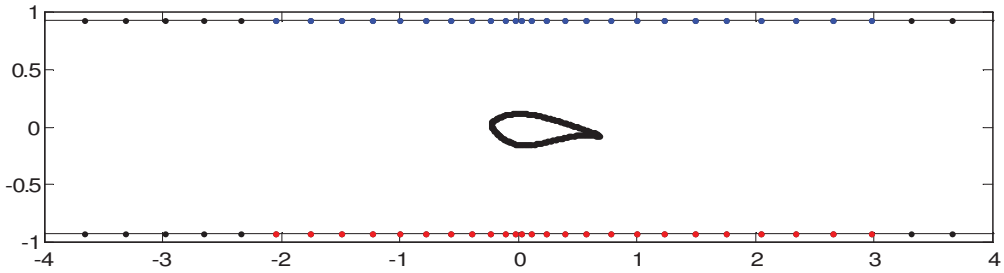

Figure A.17. Panel configuration including wind tunnel walls.

suction and pressure side and an overall lift coefficient that is some 25% smaller. The inconsistency between these models seems to be a consequence of the extreme sensitivity of the flow past the DU97 to the details of the trailing edge flow. It is also an indication that accurate solution of the flow past this airfoil may require methods that are significantly more sophisticated than those under consideration here. This motivates the use of Navier-Stokes CFD modeling later in this section. Nevertheless, the panel code was deemed suitable for deriving downwash corrections due to the transpiration flow through the Kevlar walls.

A.5.2 Basic model of the test section walls

The basic airfoil calculation method described above was extended to model the wind tunnel interference by including a series of constant-strength source panels arranged along the side-walls of the test section, as illustrated in Figure A.17. A total of 98 panels was used to represent each wall extending 20.4m upstream and downstream of the airfoil $1/4$-chord location (compared to the test section width of 1.85m). Minimum panel length (near the airfoil) was 0.06m, maximum was 0.62m furthest from the airfoil. Control points were placed at the center of each panel.

By enforcing the non-penetration boundary condition at the control points and solving for the panel strengths simultaneously with the airfoil solution described above, the code simulates the blockage effects of a solid wall test section. An example calculation, for the DU97-W-300 at 8 degrees angle of attack, is shown in Figure A.18. We are ignoring the possible viscous effects on this airfoil, discussed above, since we are concerned here only with characterizing the inviscid

interference effects of the tunnel walls. As one might expect, the confinement of the airfoil between the walls produces significant lowering of the pressures on its suction side, and an increase in lift coefficient, from 1.39 to 1.60.

A.5.3 Modeling the transpiration through the Kevlar acoustic windows

The actual test section walls do not, of course, behave as perfect solid walls over the 5.14m length of the acoustic windows. Here pressures on the windows, set up by the airfoil flow, cause air to be drawn into the test section from, or driven out of the test section into, the anechoic chambers. Modeling the presence of this transpiration in the panel method is a straightforward modification of the boundary condition applied at the control points of the panels representing the acoustic windows. Instead of requiring that the velocity component perpendicular to the wall is zero at these points, it is set to be equal to the transpiration velocity into or out of the anechoic chamber.

The problem, of course, is determining what the transpiration velocity is and this can be done using the velocity pressure difference relations for the Kevlar scrim given in Equation (11). The pressure difference across the Kevlar is given by the pressure calculated by the panel method at the inside of the acoustic window and an estimate of the pressure in the anechoic chamber. This pressure can be estimated by requiring that (a) there be no net mass flow out of the acoustic window, or (b) that any mass flow out of one window be exactly absorbed by the other. Condition (a) would correspond to the chambers being perfectly sealed to the test section. Condition (b) would correspond to no seal at all. We will discuss which of these is most realistic later, when comparing with experimental data.

The above scheme implies a nested iterative process that proceeds as follows. First, flow in the test section is computed as for a solid wall. This provides estimates of the pressure distributions over the acoustic windows. The transpiration velocities through the windows are then calculated using Equation 11, by iteratively choosing the chamber pressure to satisfy mass flow conditions (a) or (b). For condition (a) separate pressures are estimated for the port and starboard chambers. For condition (b) only a single pressure, taken to be the same in both chambers, is needed. The panel method is then repeated with the boundary condition on the Kevlar windows set to match the just-computed transpiration velocities. This process is repeated until convergence is achieved - typically in fewer than 10 iterations.

Sample calculations are shown in Figures A.19 through A.22 for the DU97-W-300. Calculations of pressure distributions on the airfoil, pressure distributions on the Kevlar windows, transpiration velocities through the windows, and streamlines are shown for the DU97-W-300 at 8 degrees angle of attack in Figures A.19 through A.21. These calculations were performed using the porosity relation (Equation (11)) for both mass flow conditions. The effect of the porosity is, primarily, to reduce the magnitude of the pressure coefficient on the suction side of the airfoil (Figure A.19). This reduction is greater when mass flow into or out of the acoustic windows is permitted, since this allows a slightly greater turning of the overall flow by the airfoil (Figure A.21). Transpiration is greatest near the quarter chord location of the airfoil (x=0, Figure A.20). Velocities are greatest into the test section on the starboard (suction) side of the airfoil, and peak at 2 to 3% of the

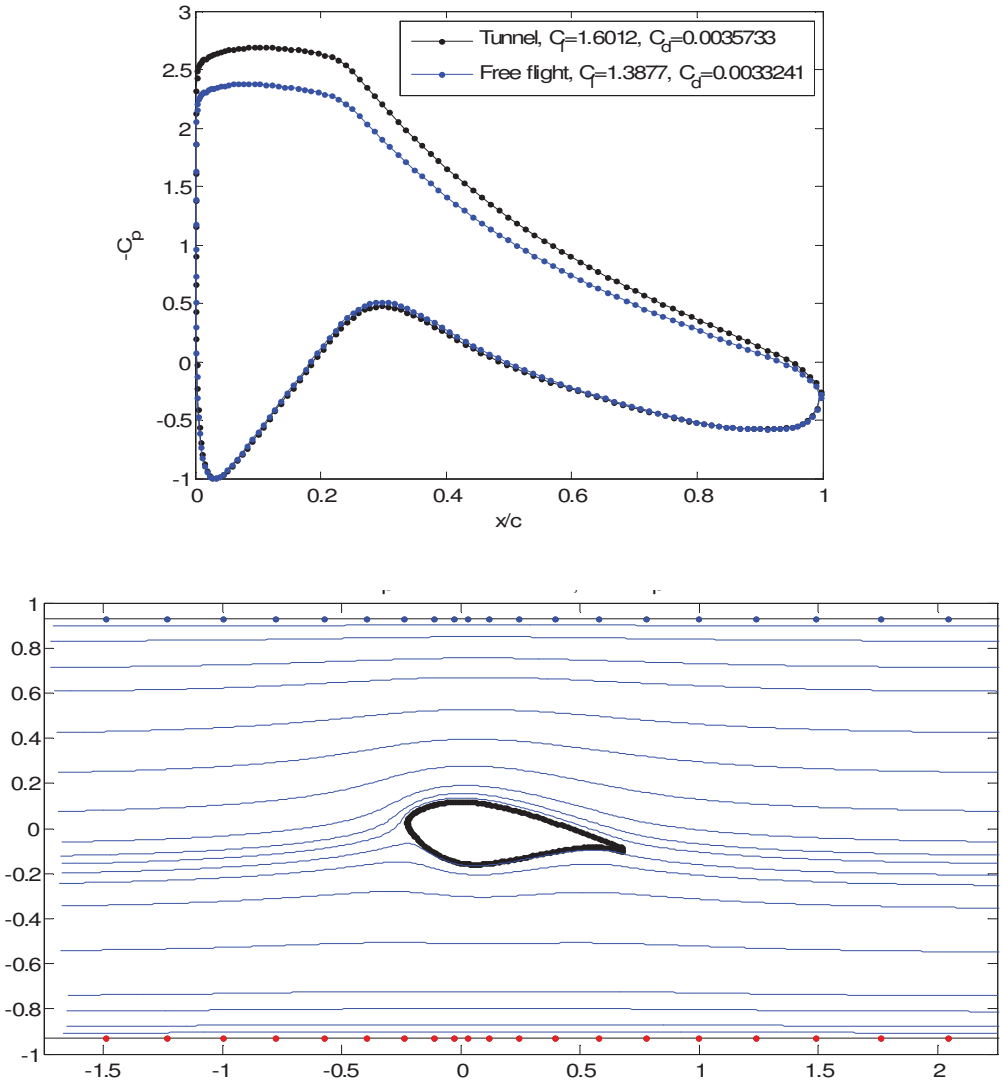

Figure A.18. DU97-W-300 at 8 degrees angle of attack, showing effects of solid test section walls. Top : pressure distribution compared with free flight. Bottom : streamlines.

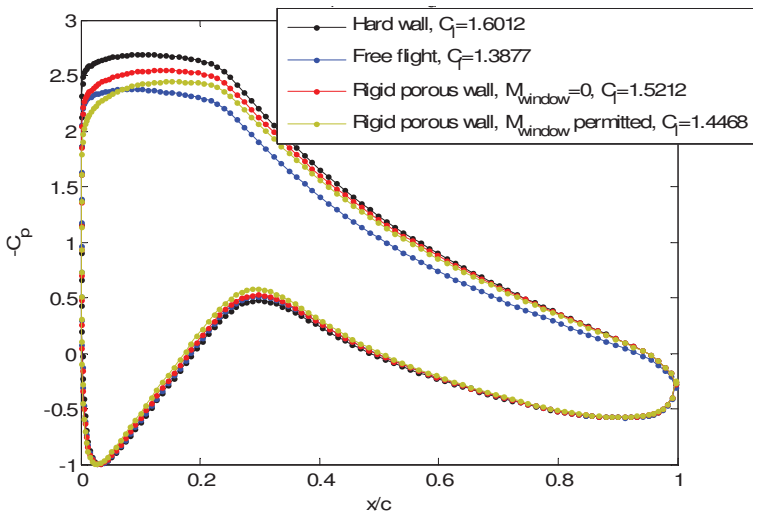

Figure A.19. DU97-W-300 at 8 degrees angle of attack. Computed pressure distributions for free flight, solid-wall test section, and porous rigid wall test section. Porous wall shown for no mass flux through window (condition 'a'), and mass flux allowed (condition 'b').

free stream speed. Transpiration velocities reduce towards the ends of the windows and, for mass flow condition 'a' (no net mass flux), reverse direction. The pressure difference distributions are qualitatively similar to the transpiration velocity distributions.

The changes in the airfoil pressure distributions due to the porosity of the Kevlar and the different mass flow conditions are almost identical to those that would be produced by a change in angle of attack, as shown in Figure A.22. With no net mass flow through the windows (condition 'a'), the airfoil flow is almost identical to that which would be produced in the solid wall test section at an angle of 7.4 degrees (a reduction of 0.6 degrees). With mass flow allowed, the effective angle of attack is 6.9 degrees (a reduction of 1.1 degrees). This observation is important. It implies that the Kevlar walls are in the 'aerodynamic farfield' and that the effects of their porosity can be corrected for simply by adjusting the angle of attack.

A.6 Simplified Porous Wall Downwash Correction

A.6.1 Panel Method Parameter Studies

As discussed in Section A.5.3, the aerodynamic effects of the Kevlar acoustic windows are limited to changes in the far-field boundary conditions similar to those that would be imposed by a conventional solid wall test section. In this section we use this observation to investigate and develop simplified correction methods.

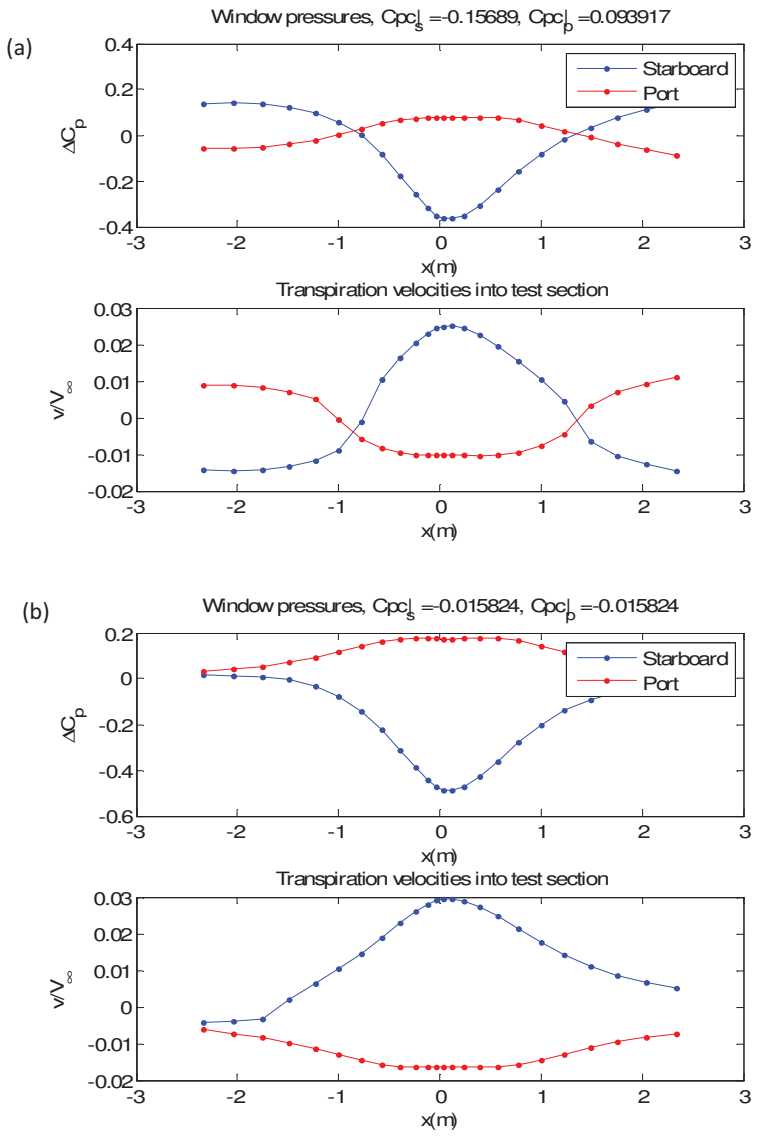

Figure A.20. DU97-W-300 at 8 degrees angle of attack. Computed pressure distributions and transpiration velocity distributions along the two acoustic windows modeled as porous rigid walls with mass flow condition 'a' (top) and 'b' (bottom).

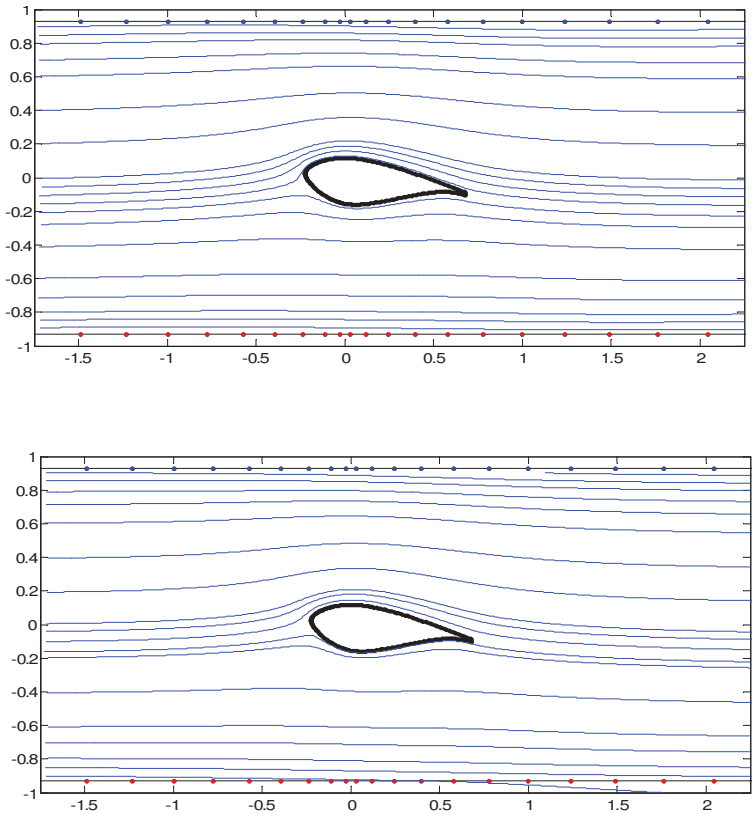

Figure A.21. DU97-W-300 at 8 degrees angle of attack. Computed streamline patterns for porous, rigid test section walls with mass flow condition 'a' (top) and 'b' (bottom).

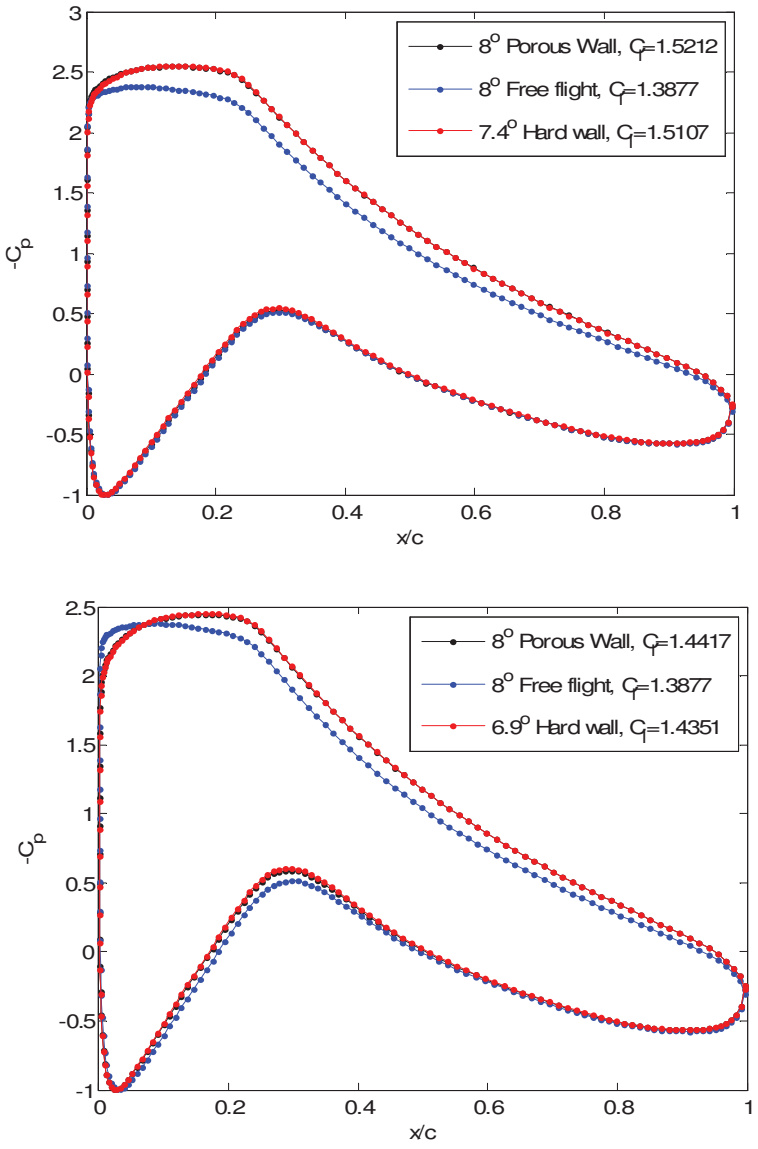

Figure A.22. Comparison of pressure distributions computed for the DU97-W-300 at 8 degrees angle of attack for porous, rigid test section walls and pressure distributions predicted for solid wall boundary conditions at lower angles of attack. Mass flow condition 'a' (top) and 'b' (bottom).

A series of calculations were performed for the case of rigid but porous test section walls for different angles of attack, airfoil shapes and chordlengths to reveal the effects of porosity alone on the aerodynamics. As discussed in Section A.5.3, the panel code predicts that the effects of the porosity are almost the same as the effects of an angle of attack change. Thus airfoil pressure distributions at a given geometric angle of attack very closely match those computed for a hard-wall test section but for a slightly reduced angle α_h, the difference depending on the chord length, angle of attack and details of the porosity. We therefore define the proportionate angle of attack correction δ (to hard-wall conditions),

$$\delta \equiv \frac{\alpha - \alpha_h}{\alpha - \alpha_{0l}} \tag{13}$$

where α_{0l} is the zero lift angle of attack of the airfoil section. That is, the effective hard-wall test section angle of attack is given by

$$\alpha_h = \alpha - (\alpha - \alpha_{0l})\delta \tag{14}$$

The first sets of calculations were all performed using the porosity relation given by Equation (11) and with mass flow boundary condition (b), i.e. with a net mass flow permitted through the acoustic windows. Results are shown in Figures A.23 through A.25. These figures include panel code predictions, displayed as symbols, as well as results from simple a correction model presented later in this section, displayed as solid lines. Note that the effective angles of attack were determined by subjective comparison and so are not completely free from uncertainty.

Figure A.23 shows the dependence of δ on angle of attack for the 0.91-m DU97-W-300 airfoil and for a hypothetical 0.91-m chord NACA 0012. These chordlengths imply a chord-to-test section width ratio c/h =0.493. The proportionate angle of attack correction is not constant, but reduces by almost 40% as the angle of attack increases from 4 to 16 degrees. It is, however, almost identical for the two airfoils, making it unlikely that it is a function of airfoil shape. Figure A.24 shows the effect of chord length (in terms of c/h) for the NACA 0012 at 8 degrees angle of attack. Increasing the chord length increases the correction but following a non-linear variation. Figure A.25 shows the effect of flow speed on the correction for a 0.91-m chord NACA 0012 at 8 degrees angle of attack. There is an effect of flow speed (a gradual increase in the correction) because the exponent in the porosity relation, Equation (11), is not exactly 0.5, implying some Reynolds number dependence.

Similar calculations (not shown) were performed with changes to the porosity boundary condition, using mass flow boundary condition (a) (no net mass flow out of either chamber). The corrections are significantly less (roughly half) with this mass flow constraint. Figure A.26 shows the effects of chord length on the NACA 0012 with mass flow boundary condition (b) but with the porosity relation replaced by the hypothetical linear expression,

$$V = 0.00533\Delta p \tag{15}$$

which gives about the same velocity as Equation 11 for Δp=100Pa. Interestingly, this linear relation results in a linear dependence of the correction on chord length, as opposed to the non-linear dependence seen in Figure A.24. This is an important clue for the development of a simplified relation for the effects of the porosity, since it implies an intimate relationship between the correction and the porosity relation.

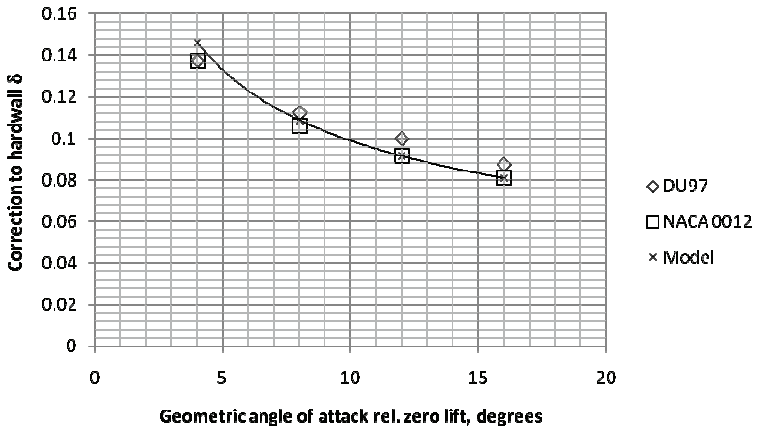

Figure A.23. Effect of angle of attack on the proportionate angle of attack correction to hardwall δ for 0.91-m chord airfoils at 30m/s as computed using the hybrid panel method and given by the simplified model. Net mass flow permitted through acoustic windows. Porosity given by Equation (11).

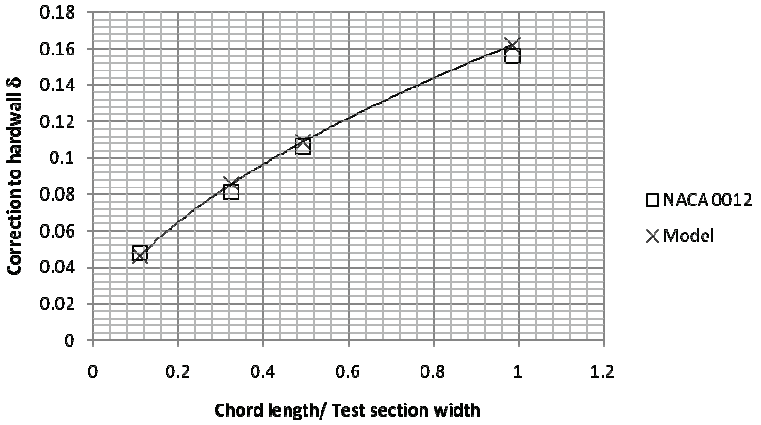

Figure A.24. Effect of airfoil chord on the proportionate angle of attack correction to hardwall δ for 8 degrees angle of attack at 30m/s as computed using the hybrid panel method and given by the simplified model. Net mass flow permitted through acoustic windows. Porosity given by Equation (11).

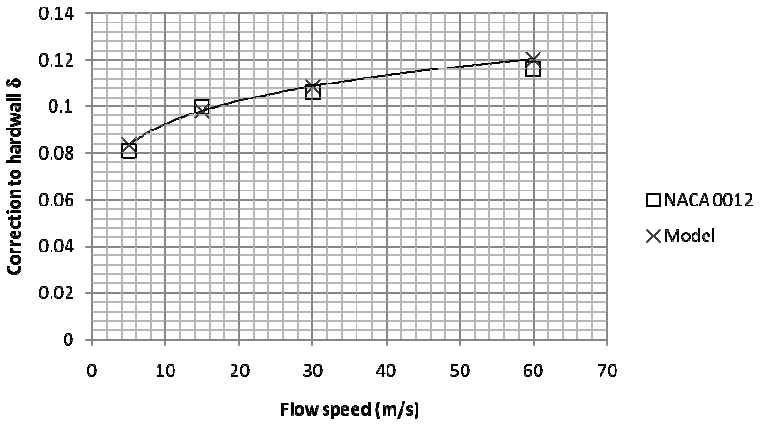

Figure A.25. Effect of flow speed on the proportionate angle of attack correction to hardwall δ for 0.91-m chord airfoils at 8 degrees angle of attack as computed using the hybrid panel method and given by the simplified model. Net mass flow permitted through acoustic windows. Porosity given by Equation (11).

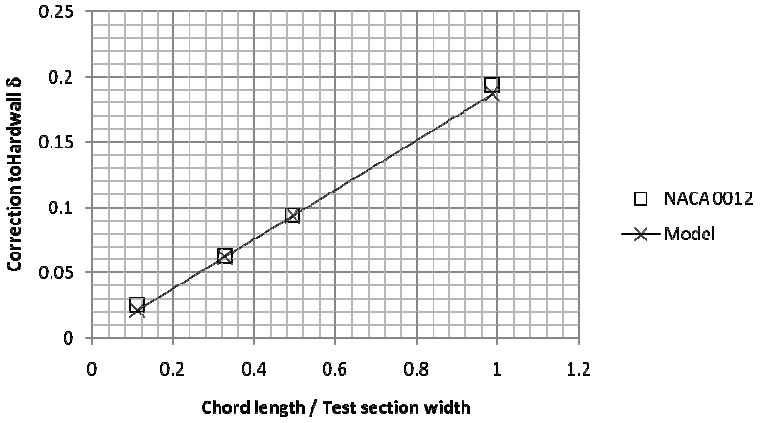

Figure A.26. Effect of airfoil chord on the proportionate angle of attack correction to hardwall δ for 8 degrees angle of attack at 30m/s as computed using the hybrid panel method and given by the simplified model. Net mass flow permitted through acoustic windows. Porosity given by the linear expression in Equation (15).

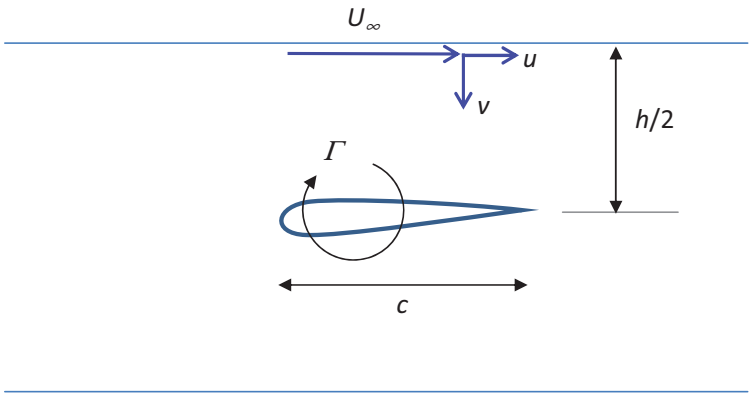

Figure A.27. Schematic showing variables used in the derivation of the porosity correction formula.

A.6.2 Derivation of the Simplified Downwash Correction

Consider the airfoil between porous walls, as illustrated in Figure A.27. The airfoil generates a circulation Γ and this circulation acts to increase or decrease the velocity along the porous walls near the airfoil. The maximum change will be $\Gamma/\pi h$, felt immediately above or below the quarter chord. The actual deviation from the free stream velocity on the walls will have a typical value that is reduced from this number, since it will represent the average over some streamwise distance, but then increased by the effects of the images of the airfoil in the tunnel walls. We therefore write this typical value as

$$u \approx A\frac{\Gamma}{\pi h} \tag{16}$$

where A is a constant, expected to be of order 1. In terms of the lift coefficient on the airfoil C_l this expression is

$$u \approx A\frac{C_l U_\infty c}{2\pi h}. \tag{17}$$

This velocity deviation results in a non-zero pressure coefficient on the acoustic window with a magnitude of

$$|C_p| \approx \frac{2u}{U_\infty} \approx A\frac{C_l}{\pi}\frac{c}{h}, \tag{18}$$

where we have used the linearized form of the pressure coefficient.

The pressure acting on the porous walls is what draws the flow through them, resulting in a transpiration velocity with a magnitude given by a relation of the form,

$$v = C|\Delta p|^n \tag{19}$$

(such as Equation 11) where Δp is the difference between the pressure on the acoustic window and the pressure in the chamber behind it. If we assume the chamber pressure is only slightly different than the free stream pressure (an assumption met most accurately when mass flow out of

the acoustic windows is permitted), then this expression can be re-written as,

$$\frac{v}{U_\infty} = \frac{C}{U_\infty}\left(\frac{1}{2}\rho U_\infty^2\right)^n |C_p|^n \tag{20}$$

Now, v/U is the typical flow angle at the wall that results from the porosity. We would therefore expect this to also be the reduction in the effective angle of attack that results from the porosity. Substituting Equation (18) for the pressure coefficient, we therefore have

$$\alpha - \alpha_h \approx \frac{v}{U_\infty} \approx \frac{C}{U_\infty}\left(\frac{1}{2}\rho U_\infty^2\right)^n A^n \left(\frac{C_l}{\pi}\right)^n \left(\frac{c}{h}\right)^n \tag{21}$$

or

$$\delta = \frac{\alpha - \alpha_h}{\alpha - \alpha_{0l}} = A^n \frac{C}{(2\pi)^n}\rho^n U_\infty^{2n-1} \frac{C_l^n}{\alpha - \alpha_{0l}}\left(\frac{c}{h}\right)^n \tag{22}$$

We can reduce this relationship by assuming the thin airfoil theory result for the lift coefficient $C_l = 2\pi(\alpha - \alpha_{0l})$ to give

$$\delta = A^n C \rho^n U_\infty^{2n-1} (\alpha - \alpha_{0l})^{n-1} \left(\frac{c}{h}\right)^n \tag{23}$$

where the angle of attack is measured in radians. Alternatively, measuring the angle of attack in degrees, we have

$$\delta = A^n C \rho^n U_\infty^{2n-1} (\alpha - \alpha_{0l})^{n-1} \left(\frac{c}{h}\right)^n \left(\frac{\pi}{180}\right)^{n-1} \tag{24}$$

Qualitatively, this expression matches the behavior observed in Figures A.23 through A.26. For the porosity relation given by Equation 11 (n=0.5734), the normalized correction should decrease with angle of attack (Figure A.23), increase with chord length (Figure A.24) and velocity (Figure A.25). For the linear porosity relation (n=1) the increase with chord length should be linear (Figure A.26). We also note that in the limit of high Reynolds number flow through the porous walls (for which we would expect n=0.5), the correction becomes independent of velocity, as would be expected.

Quantitative results calculated using this expression are included in Figures A.23 through A.26. Note that for the DU97-W-300, a zero lift angle of attack of -2.35 degrees was used and that the density (1.19 kg/m^3) was set to the same value used in the hybrid panel method. For those cases where mass flow was permitted through the acoustic windows (represented by Figures A.23 through A.26), the constant A was simply set to 1 and thus represent absolute predictions. The agreement is very encouraging, the agreement for the variations in chord length, angle of attack and velocity all being quite good. Surprisingly, the method also accurately predicts the level of the linear variation in Figure A.26, suggesting that the influence of the porosity relation is correctly captured in this expression.

With net mass flow not permitted through the porous walls (results not shown), the assumption that the chamber pressures are equal to the free stream pressure is not as good. Indeed one would expect the pressure in each chamber to settle roughly to the average pressure impressed on the porous wall inside the test section. The net effect should be to reduce the constant A by a factor of about 2. In reality a value of 0.35 was used to provide good agreement with the panel method results.

A.7 Streamline Curvature and Blockage Corrections

The remaining wall interference effects requiring correction are streamline curvature and blockage. The experimental measurements for surface pressure and lift, when corrected for porous wall downwash and classical solid wall blockage effects [14], did not agree well with the benchmark TU-Delft data set [5] or with Reynolds-averaged Navier-Stokes CFD predictions (good agreement was observed between CFD and the Delft data set). The pressure distribution comparisons indicated that the angle of attack correction was accurate, but that the blockage effect for the porous wall tunnel was weaker than the solid wall blockage theory predicts.

In order to quantify the blockage effect, a series of CFD computations was performed at the 30 m/s flow conditions (with "free flight" boundary conditions) and the computed pressure distributions compared to the present data. The CFD code is the SACCARA code [15], a finite volume solver developed at Sandia National Labs that has been extensively validated on external aerodynamic problems. The Spalart-Allmaras turbulence model was used, and the Xfoil code was used to estimate boundary layer transition locations. A very fine computational mesh was used in order to ensure numerically accurate results. The following describes the method for making this comparison and using it to derive an approximate porous wall blockage correction.

A.7.1 Validation of CFD Model

Free-flight, free-transition CFD results are first compared to data taken in the TU-Delft low-speed, low-turbulence wind tunnel at a chord Reynolds number of $Re_c = 3 \times 10^6$. The ratio c/h for the TU-Delft experiment was 0.33, resulting in relatively mild solid wall interference. Figure A.28 shows the comparison of (corrected) measured and computed pressure distributions for three effective angles of attack. At $\alpha = -0.03$ and $\alpha = 6.18$ deg., the agreement is very good, with some over-prediction of the minimum pressure on the pressure surface. This over-prediction may be the due to the inability of the CFD model to accurately capture separation-induced boundary layer transition, which appears to be indicated by the measured data. For $\alpha = 11.85$ deg., the CFD model does not predict the measured separation zone on the suction surface near the trailing edge, which results in an underprediction of the minimum suction surface pressure. From these results, we can conclude that the CFD model gives good agreement with the TU-Delft data for attached-flow conditions, but that conditions with suction surface boundary layer separation may result in reduced accuracy.

A.7.2 Solid Wall Interference Corrections

Allen and Vincente [14] derived solid wall interference corrections using thin airfoil theory. The corrections result from the requirement that the magnitude of the suction peak of the corrected pressure distribution match that of the free-flight pressure distribution. Included in the method are formulas for corrected force coefficients as well as a procedure for correcting the airfoil surface pressure distribution. The velocity increment resulting from the solid wall blockage for incom-

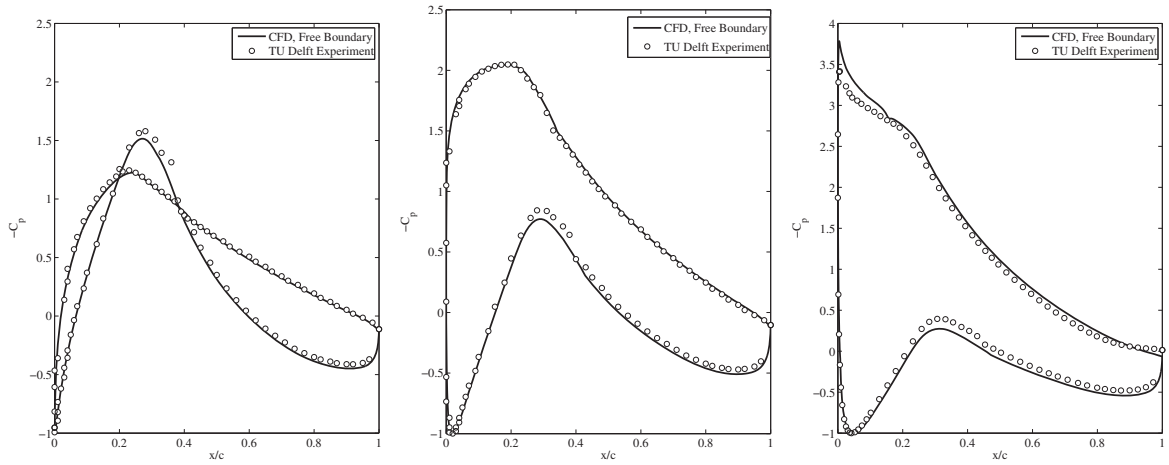

(a) $\alpha = -0.03$ deg. **(b)** $\alpha = 6.18$ deg. **(c)** $\alpha = 11.85$ deg.

Figure A.28. Comparison of CFD results with TU-Delft wind tunnel data at $Re_c = 3 \times 10^6$.

pressible flow is given by

$$\frac{u'_{sw}}{U_\infty} = \Lambda\sigma, \tag{25}$$

with Λ depending on the symmetric component of the airfoil shape and with

$$\sigma = \frac{\pi^2}{48}\left(\frac{c}{h}\right)^2, \tag{26}$$

where c is the airfoil chord and h is the test section width. There are also corrections to the lift distribution and to the angle of attack associated with the streamline curvature induced by the tunnel walls. The angle of attack correction is given by

$$\Delta\alpha_{sw} = \frac{57.3\sigma}{2\pi}\left[C'_l + 4C'_{m_{c/4}}\right] \text{deg.} \tag{27}$$

where C'_l and $C'_{m_{c/4}}$ are the uncorrected lift and moment coefficients.

Approximate blockage corrections for porous wind tunnel walls can be derived in the form

$$\frac{u'_{pw}}{U_\infty} = \Omega\frac{u'_{sw}}{U_\infty}, \tag{28}$$

where u'_{pw} is the porous wall free-stream velocity correction, and Ω is a factor multiplying the solid wall free-stream velocity correction u'_{sw}. Ω can be positive or negative and depends on the porosity of the walls [16].

In order to assess the applicability of the solid wall blockage correction to the surface pressure distribution over the DU97-W-300, a numerical experiment was performed. First, the pressure

distribution was computed (using CFD) for the airfoil with solid wall side boundaries at an angle of attack of 5.74 degrees and $c/h = 0.5$, corresponding to the tested configuration. The side walls were modeled as inviscid free-slip boundaries, with the assumption that the side wall boundary layers would have only a small effect on the blockage. Next, the pressure distribution was computed for free-flight conditions at an angle of attack of 6.00 degrees, which corresponds to the effective angle of attack including the solid wall streamline curvature effect (Equation 27). The solid wall blockage corrections of [14] were then applied to the in-tunnel computational results. Comparison of the two cases is shown in Figure A.29. The maximum difference between the two C_p distributions is about 0.04. This level of agreement indicates that the blockage correction method is valid for the present airfoil and test conditions.

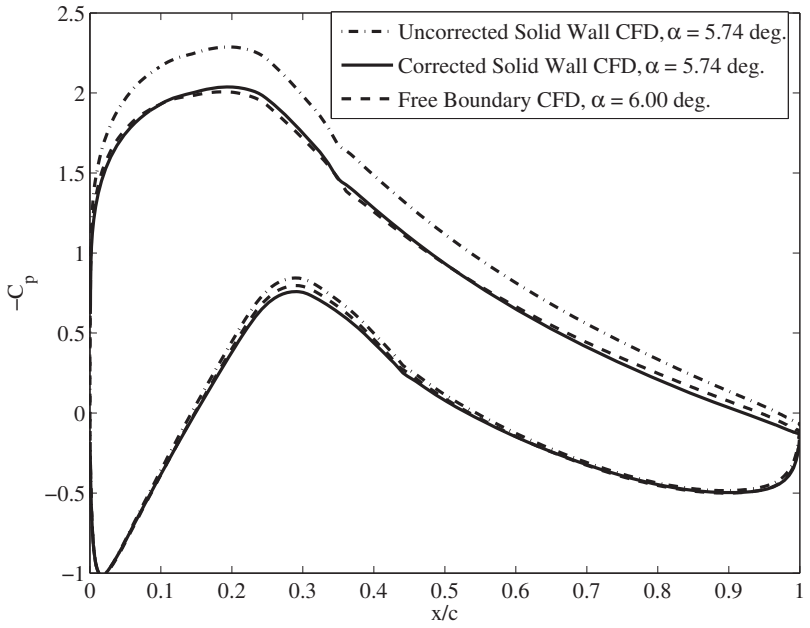

Figure A.29. Comparison of corrected solid wall CFD surface pressure distribution with "equivalent" free boundary CFD pressure distribution.

A.7.3 Comparison of Experimental Data with CFD Results

The applicability of the porous wall blockage correction (28) is now examined by comparison of CFD results with corrected wind tunnel data for the DU97-W-300 at 30 m/s. Free-flight CFD results were obtained for the three effective angles of attack measured in the Virginia Tech Stability Wind Tunnel: $\alpha = -0.43$ deg., $\alpha = 5.74$ deg., and $\alpha = 11.93$ deg. Two computations were performed at each angle of attack: one with free boundary layer transition and one with upper boundary layer leading edge transition. The free-transition cases were run by imposing boundary layer transition at the chord-wise locations predicted by the Xfoil code [13]. The upper leading edge transition cases apply transition at the leading edge for the upper (suction) surface boundary layer, while retaining the free transition condition for the lower surface boundary layer. Early

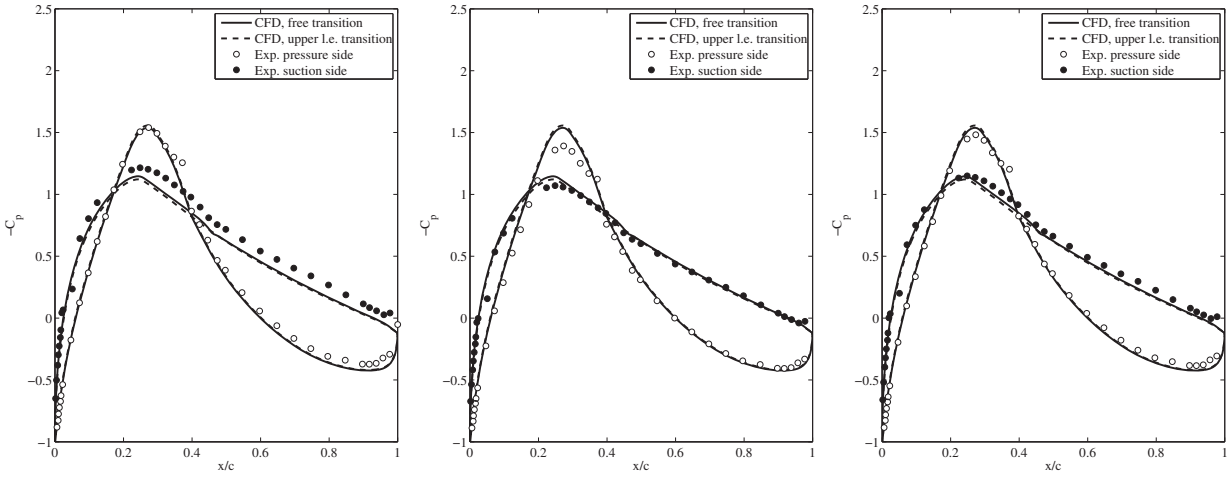

(a) Uncorrected **(b)** Corrected, $\Omega = 1.0$ **(c)** Corrected, $\Omega = 0.42$

Figure A.30. Surface pressure distributions, $Re_c = 1.8 \times 10^6$, $\alpha = -0.43$ deg.

boundary layer transition on the suction surface has the effect of lowering the suction peak. The goal of running these cases was to assess this effect relative to the effect of correcting the pressure distributions for blockage.

Figure A.30 shows the measured uncorrected pressure distribution, the pressure distributions corrected for solid and porous wall ($\Omega = 0.42$) blockage, and comparison with the CFD results, for $\alpha = -0.43$ deg. The CFD results in this case are insensitive to the upper boundary layer transition condition. The shape of the uncorrected pressure distribution agrees reasonably well with the CFD results, with some discrepany over the suction surface. Agreement improves over the suction surface with application of the full solid wall blockage correction $\Omega = 1.0$, while agreement over the pressure surface worsens. At an intermediate value of the blockage correction (Figure A.30(c)), agreement is good over both surfaces. The value $\Omega = 0.42$ is not necessarily an optimal value for best agreement, but was chosen by trial and error for the $\alpha = 5.74$ degree case, and then kept fixed for other angles of attack.

Figure A.31 shows the measured and calculated pressure distributions for $\alpha = 5.74$ deg. The leading edge transition condition results in a slightly lower predicted suction peak relative to the free-transition result. The uncorrected experimental data show lower suction surface pressures than the CFD results. Application of the full solid wall correction appears to over-correct the pressures relative to the CFD results, while the $\Omega = 0.42$ partial correction again results in good agreement with the CFD results.

For $\alpha = 11.93$ degrees, the measured pressure distributions indicate a region of separated flow on the suction surface near the trailing edge (Figure A.32(a)). The free-transition CFD solution does not predict flow separation in this region while the leading edge transition solution does.

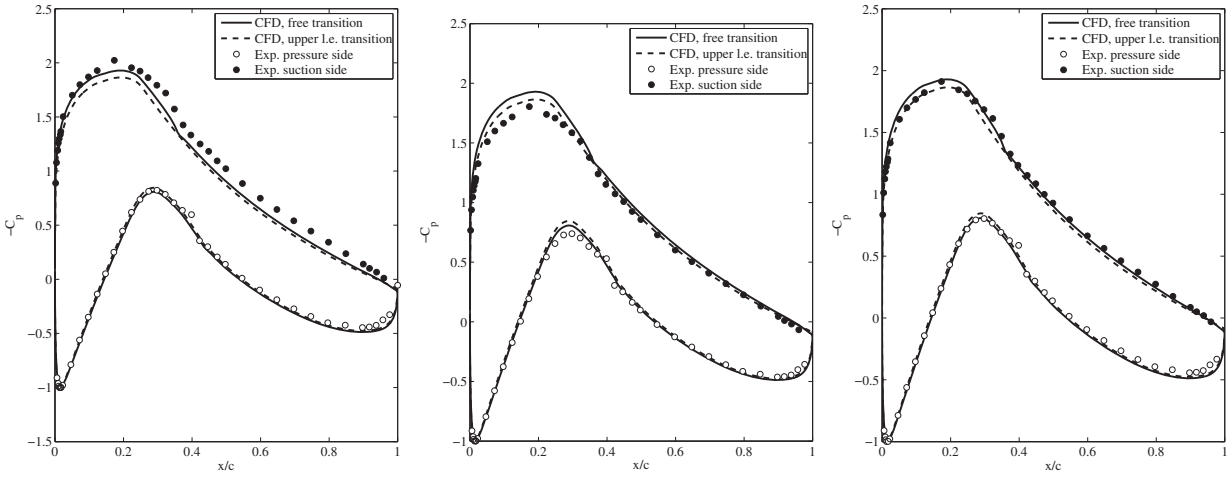

(a) Uncorrected **(b)** Corrected, $\Omega = 1.0$ **(c)** Corrected, $\Omega = 0.42$

Figure A.31. Surface pressure distributions, $Re_c = 1.8 \times 10^6$, $\alpha = 5.74$ deg..

The measured suction peak lies in between that predicted by the free-transition and leading edge transition CFD cases. The full solid wall blockage correction results in good agreement between the corrected values and the leading-edge transition case, while the partial correction ($\Omega = 0.42$) gives comparable agreement for the suction surface and possibly a small improvement over the pressure surface. While it is not certain that the experimental suction surface boundary layer transitioned at the leading edge, it does appear that correct prediction of the region of separated flow near the trailing edge is important in capturing the suction surface pressure distribution.

Overall, the comparisons with CFD verify the porous wall angle of attack correction. The basic shape of the computed pressure distributions is similar to the measured distributions, independent of the blockage correction. In particular, it does not appear that a further shift in angle of attack would improve agreement, since this would cause the upper and lower surface pressures to move apart simultaneously. An examination of Figures A.30 – A.32 shows that this would not uniformly improve the agreement for any of the comparisons.

The comparisons indicate that the full solid wall blockage correction ($\Omega = 1.0$) would be too strong, but that an intermediate correction ($\Omega = 0.42$) gives improved agreement between computation and experiment. However, such a reduced blockage correction is not predicted by the panel code, which predicts blockage very similar to solid wall blockage. It may be that the conservative mass flow condition enforced in the panel code method, where mass inflow through one window must be compensated by mass outflow through the other window, is, in practice, violated. If there is a net mass outflow from the test section, the overall blockage would be reduced.

For the results labeled *corrected* in Section 4, the downwash correction of Equation (24) has been applied, in addition to the blockage correction of Equation (28) with $\Omega = 0.42$ (and applying

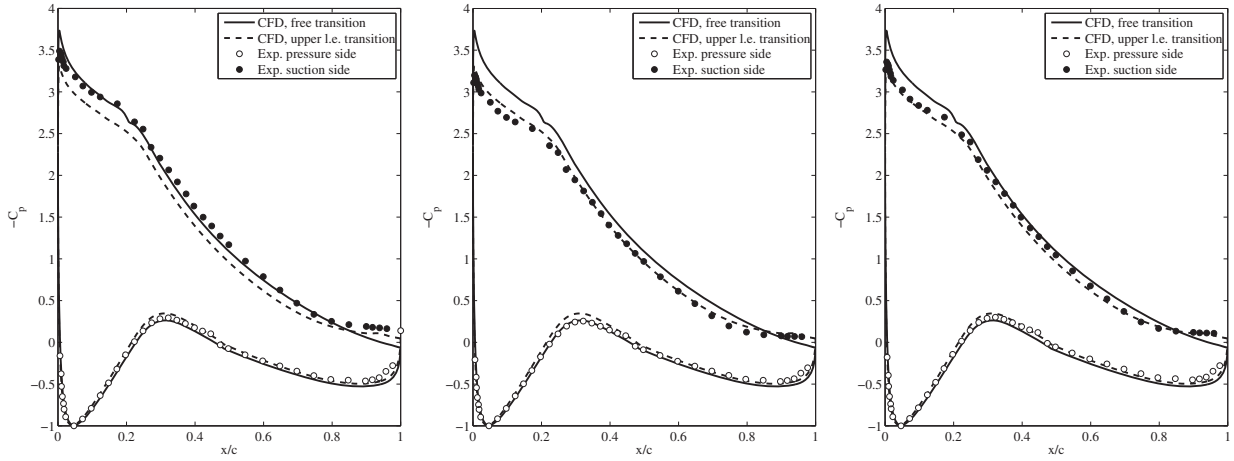

(a) Uncorrected **(b)** Corrected, $\Omega = 1.0$ **(c)** Corrected, $\Omega = 0.42$

Figure A.32. Surface pressure distributions, $Re_c = 1.8 \times 10^6$, $\alpha = 11.93$ deg..

the method of [14]). Both force coefficients and surface pressure corrections have been made.

Application of the present method was not successful in correcting the pressure distributions obtained at higher free stream velocities. By this we mean we were not able to match the TU-Delft and CFD pressure distributions for the DU97-W-300 by applying the downwash correction and an intermediate blockage correction. Given this uncertainty in the corrections at higher free stream velocities, we chose to present data at these velocities as uncorrected, pending further examination and improvement of the corrections.

Appendix B Definition of $1/12^{\text{th}}$ Octave Bands

The $1/12^{\text{th}}$ octave bands are computed as follows: The upper band limit in terms of the n^{th} band center frequency is

$$f_u^n = 2^{1/12} f_c^n.$$

The lower band limit in terms of the n^{th} band center frequency is

$$f_l^n = 2^{-1/12} f_c^n.$$

The band's center frequency sequence is then computed as

$$f_c^n = 2^{1/24} f_c^{n-1},$$

where the reference center frequency is 1 Hz (band number 1). The figure below illustrates the $1/12^{\text{th}}$ octave band boundaries in the 500 to 5000 Hz frequency range.

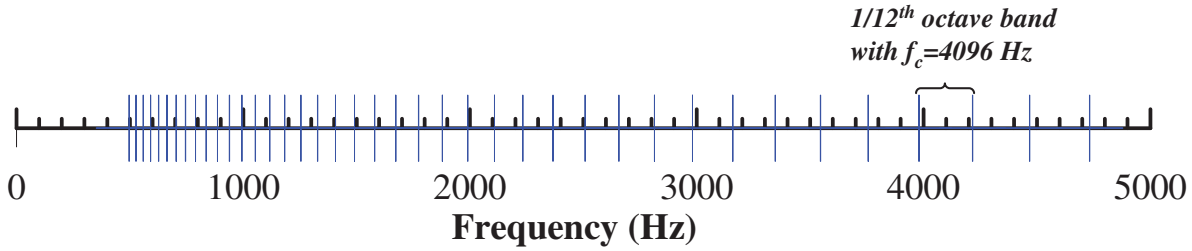

References

[1] J.A. Paquette and P.S. Veers. Increased strength in wind turbine blades through innovative structural design. *Proceedings of the European Wind Energy Conference*, 2007.

[2] J.P. Baker, E.A. Mayda, and C.P. van Dam. Experimental analysis of thick blunt trailing-edge wind turbine airfoils. *J. Solar Energy Engineering*, 128:422–431, 2006.

[3] K.J. Standish and C.P. van Dam. Aerodynamic analysis of blunt trailing edge airfoils. *J. Solar Energy Engineering*, 125:479–487, 2003.

[4] D.D. Chao and C.P. van Dam. Computational aerodynamics analysis of a blunt trailing-edge airfoil modification to the NREL phase VI rotor. *Wind Energy*, 10(6):529–550, 2007.

[5] W.A. Timmer and R.P.J.O.M. van Rooij. Summary of the Delft University wind turbine dedicated airfoils. *J. Solar Energy Engineering*, 125:488–496, 2003.

[6] K. Choi and R. Simpson. Some mean velocity, turbulence, and unsteadiness characteristics of the VPI&SU stability wind tunnel. Department of Aerospace and Ocean Engineering, Virginia Polytechnic Institute and State University, Report VPI-Aero-161, 1987.

[7] S.M. Jaeger, W.C. Horne, and C.S. Allen. Effect of surface treatment on array microphone self noise. AIAA Paper 2000-1937, 2000.

[8] E. Crede. Aerodynamics and aeroacoustics of the Virginia Tech Stability Tunnel anechoic system. MS Thesis, Virginia Tech, 2008.

[9] J. Staubs. Real airfoil effects on leading edge noise. Ph.D. Dissertation, Virginia Tech, 2008.

[10] M.C. Remillieux, H.E. Camargo, and R.A. Burdisso. Calibration of a microphone phased-array for amplitude in the Virginia Tech anechoic wind tunnel. NOISE-CON 2007, Reno, NV, October 2007.

[11] P.W. Bearman. Corrections for the effect of ambient temperature drift on hot-wire measurements in incompressible flow. DISA Information, no. 11, pp. 25–30, 1971.

[12] M.C. Remillieux, H.E. Camargo, R.A. Burdisso, W.J. Devenport, M. Rasnick, P. van Seeters, and A. Chou. Calibration and demonstration of the new Virginia Tech anechoic wind tunnel. 14th AIAA/CEAS Aeroacoustics Conference, Vancouver BC, May 2008.

[13] M. Drela and M.B. Giles. Viscous-inviscid analysis of transonic and low-Reynolds number airfoils. *AIAA J.*, 25(10):1347–11355, 1987.

[14] H.J. Allen and W.G. Vincenti. Wall interference in a two-dimensional-flow wind tunnel, with consideration of the effect of compressibility. NACA Report No. 782, 1947.

[15] C. C. Wong, M. Soetrisno, F. G. Blottner, S. T. Imlay, and J. L. Payne. PINCA: A scalable parallel program for compressible gas dynamics with nonequilibrium chemistry. Sandia National Labs, Report SAND 94-2436, Albuquerque, NM, April 1995.

[16] B.F.R. Ewald. Wind tunnel wall correction. AGARD-AG-336, 1998.

DISTRIBUTION

Mike Bergey
Bergey Wind Power Company
2200 Industrial Blvd.
Norman, OK 73069

David Calley
Southwest Windpower
1801 West Route 66
Flagstaff, AZ 86001

Larry Carr
NASA Ames Research Center
24285 Summerhill Ave.
Los Altos, CA 94024

Jamie Chapman
Texas Tech University
Wind Science & Eng. Research Center
Box 41023
Lubbock, TX 79409-1023

Ian Chatting
Vestas Global Research
Tech Centre, Monks Brook
St. Cross Business Park
Newport
Isle of Wight, PO30 5WZ
UK

R. Nolan Clark
USDA - Agricultural Research Service
PO Drawer 10
Bushland, TX 79012

William Devenport
Department of Aerospace and Ocean Eng.
Virginia Tech
215 Randolph Hall
Blacksburg, VA 24061

Fort Felker
NREL/NWTC
1617 Cole Boulevard
Golden, CO 80401

Carlos Ferreira
Wind Energy Section
Delft University of Technology
Kluyverweg 1
2629 HS Delft
The Netherlands

R. Gopalakrishnan
GE Wind Energy
GTTC, 300 Garlington Road
Greenville, SC 29602

Dayton Griffin
Global Energy Concepts, LLC
1809 7th Ave., Suite 900
Seattle, WA 98101

Sandeep Gupta
Clipper Windpower Inc.
6305 Carpinteria Ave. Suite 300
Carpinteria, CA 93013

D. Hodges
Georgia Institute of Technology
270 Ferst Drive
Atlanta, GA 30332

William E. Holley
GE Wind Energy
GTTC, M/D 100D
300 Garlington Rd.
PO Box 648
Greenville, SC 29602-0648

Adam Holman
USDA - Agricultural Research Service
PO Drawer 10
Bushland, TX 79012-0010

Kevin Jackson
Dynamic Design
123 C Street
Davis, CA 95616

Jason Jonkman
NREL/NWTC
1617 Cole Boulevard
Golden, CO 80401

Gary Kanaby
Knight & Carver Yacht Center
1313 Bay Marina Drive
National City, CA 91950

Kevin Kinzie
GE Energy
P.O. Box 648
GTTL 1236
Greenville, SC 29602

Scott Larwood
1120 N. Stockton St.
Stockton, CA 95203

Dennis Lin
Office of Wind & Hydropower Technologies
EE-2B Forrestal Building
1000 Independence Ave. SW
Washington, DC 20585

David Malcolm
Global Energy Concepts, LLC
1809 7th Ave., Suite 900
Seattle, WA 98101

Amir Mikhail
Clipper Windpower Inc.
6305 Carpinteria Ave. Suite 300
Carpinteria, CA 93013

Patrick Moriarty
NREL/NWTC
1617 Cole Boulevard
Golden, CO 80401

Phil Morris
233P Hammond Building
Department of Aerospace Engineering
The Pennsylvania State University
University Park, PA 16802

Library NWTC (5)
NREL/NWTC
1617 Cole Boulevard
Golden, CO 80401

Byron Neal
USDA - Agricultural Research Service
PO Drawer 10
Bushland, TX 79012

Steve Nolet
TPI Composites, Inc.
373 Market Street
Warren, RI 02885-0328

Tim Olsen
Tim Olsen Consulting
1428 S. Humboldt St.
Denver, CO 80210

Cecelia M. Poshedly (5)
Office of Wind & Hydropower Techologies
EE-2B Forrestal Building
U.S. Department of Energy
1000 Independence Ave. SW
Washington, DC 20585

Michael Robinson
NREL/NWTC
1617 Cole Boulevard
Golden, CO 80401

Dan Sanchez
U.S. Department of Energy
NNSA/SSO
PO Box 5400 MS 0184
Albuquerque, NM 87185-0184

Scott Schreck
NREL/NWTC
1617 Cole Boulevard MS 3811
Golden, CO 80401

Brian Smith
NREL/NWTC
1617 Cole Boulevard MS 3811
Golden, CO 80401

Andrew Swift
Texas Tech University
Civil Engineering
PO Box 41023
Lubbock, TX 79409-1023

Robert W. Thresher
NREL/NWTC
1617 Cole Boulevard MS 3811
Golden, CO 80401

Nando Timmer
Wind Energy Research Group
Delft University of Technology
Kluyverweg 1
2629 HS Delft
The Netherlands

Steve Tsai
Stanford University
Aeronautics & Astronautics
Durand Bldg. Room 381
Stanford, CA 94305-4035

C.P. van Dam
Dept. of Mechanical & Aerospace Eng.
University of California, Davis
One Shields Avenue
Davis, CA 95616-5294

Brian Vick
USDA - Agricultural Research Service
PO Drawer 10
Bushland, TX 79012

Carl Weinberg
Weinberg & Associates
42 Green Oaks Court
Walnut Creek, CA 94596-5808

Carsten Westergaard
Vestas Technology R&D Americas, Inc.
440 Louisiana Street, Suite 400
Houston, TX 77002

Kyle Wetzel
Wetzel Engineering, Inc.
PO Box 4153
Lawrence, KS 66046-1153

Mike Zuteck
MDZ Consulting
601 Clear Lake Road
Clear Lake Shores, TX 77565

INTERNAL DISTRIBUTION:

MS 0557 D.T. Griffith, 1524
MS 0825 J.L. Payne, 1515
MS 0825 C.W. Bruner, 1515
MS 1124 J.R. Zayas, 6333
MS 1124 T.D. Ashwill, 6333
MS 1124 M.F. Barone, 6333
MS 1124 D.E. Berg, 6333
MS 1124 J.C. Berg, 6333
MS 1124 L. Boulton, 6333 (10)
MS 1124 S.M. Gershin, 6333
MS 1124 W. Johnson, 6333
MS 1124 B. Karlson, 6333
MS 1124 D.L. Laird, 6333
MS 1124 J. Paquette, 6333
MS 1124 M.A. Rumsey, 6333
MS 1124 P.S. Veers, 6333

MS 9018 Central Technical Files, 8944 (Electronic)
MS 0899 Technical Library, 9536 (Electronic)

Sandia National Laboratories